Membrane Modeling for Post-Combustion Carbon Capture and Direct Ocean Capture

by

Joanna Rosa Rivero

Submitted to the Graduate Faculty of

the Swanson School of Engineering in partial fulfillment

of the requirements for the degree of

Doctor of Philosophy

University of Pittsburgh

2023

UNIVERSITY OF PITTSBURGH

SWANSON SCHOOL OF ENGINEERING

This dissertation was presented

by

Joanna Rosa Rivero

It was defended on

January 27, 2023

and approved by

Heng Ban, PhD, Professor, Mechanical Engineering and Materials Science

Sangyeop Lee, PhD, Professor, Mechanical Engineering and Materials Science

Glenn Lipscomb, PhD, Professor, Chemical Engineering,University of Toledo

Dissertation Director: Katherine Hornbostel, PhD, Professor, Mechanical Engineering and Materials Science

Membrane Modeling for Post-Combustion Carbon Capture and Direct Ocean Capture

Joanna Rosa Rivero, PhD

University of Pittsburgh, 2023

The aim of this thesis is to use readily available carbon capture technology to further advance the carbon capture research field in order to mitigate global warming effects. Specifically, membranes have been deployed at a pilot scale for carbon capture for pre- and post-combustion carbon capture. This thesis organizes current computational models for post-combustion carbon capture and builds upon and applies these modeling approaches for novel carbon capture applications such as direct ocean carbon capture. First, a thorough literature review organizing hollow fiber membrane contactor models for post-combustion carbon capture was discussed to provide a rigorous comparison of state-of-the-art 1D and 2D models. Approaches to ease computational time and effort for 3D models were suggested as well. Using the information from the review, a study using hollow fiber membrane contactors for direct ocean carbon capture research was conducted consisting of experimental testing, 1D modeling of a hollow fiber membrane contactor, and finally a techno-economic analysis of a pilot scale system. The study discovered that while hollow fiber membrane contactors can be used to separate CO_2 from seawater, the technology needs to be further developed to become economically competitive. Finally, a flat sheet membrane model was developed that represents Membrane Technology Research's (MTR's) latest membrane currently undergoing pilot testing. This model accounts for channel size distributions that result from realistic manufacturing conditions. It was found that non-uniform channel heights affect the overall performance of a flat sheet membrane for gas separation. However, both membrane configurations were equally affected when comparing these non-uniform geometric conditions against a hollow fiber membrane for gas separation. Therefore, one should choose a membrane configuration based on the unique advantages discussed throughout this thesis.

Keywords: membrane modeling, carbon capture, gas separation, ocean capture.

Table of Contents

List of Tables

List of Figures

Preface

In this document is my doctoral thesis titled "Membrane Modeling for Post-Combustion Carbon Capture and Direct Ocean Capture". It was written to fulfill the graduation requirements of the Swanson School of Engineering, Mechanical Engineering and Materials Science program at the University of Pittsburgh.

I would like to thank my advisor, Dr. Katherine Hornbostel, for the excellent guidance and support during my time as a doctoral student. From our first meeting, I knew I would be educationally and emotionally supported throughout this process. Dr. Hornbostel has provided me with challenges that have maximized my learning opportunities, for which I am grateful. I also want to thank Dr. Grigorios Panagakos from Carnegie Melon University for his contribution to my first manuscript. With his support, I gained confidence in myself as I learned the ropes of the membrane and modeling field. Finally, I would also like to thank Dr. Glenn Lipscomb and his lab at the University of Toledo. Dr. Lipscomb and his students helped me fully understand membrane modeling for gas separations and provided me with additional guidance I needed to complete my thesis and contribute to the membrane field.

Additionally, I would like to thank the University of Pittsburgh's Success, Transition, Representation, Innovation, Vision and Education (STRIVE) program, as well as the Department of Energy's Office of Fossil Energy and Carbon Management for their financial support throughout my graduate studies.

Finally, I want to thank my wife, family, friends, and peers for being there for me throughout it all. Without everyone's support and positive outlook, I would not have been able to complete my work at this time given the circumstances the world faced throughout my years in graduate school.

1.0 Introduction

1.1 Executive Summary

The goal of this thesis is to develop membrane models for novel carbon capture applications, ranging from post-combustion pilot testing to ocean carbon capture. This Ph.D. thesis first reviews and organizes membrane contactor models for post-combustion carbon capture (first-author published review paper, discussed in Chapter 2). This review paper provided a rigorous comparison of state-of-the-art 1D, 2D and 3D models for post-combustion carbon capture membrane contactors. Chapter 3 illustrates using hollow fiber membrane contactors for direct ocean carbon capture research (first-author manuscript currently under review). The direct ocean carbon capture project consists of 3 completed tasks to test the feasibility of the system: experimental testing, 1D model of a hollow fiber membrane contactor, and finally a techno-economic analysis of a pilot scale system. Finally, Chapter 4 discusses the developed flat sheet membrane model that represents Membrane Technology Research's (MTR's) latest membrane currently undergoing pilot testing (published, first-author paper). This model accounts for channel size distributions that result from realistic manufacturing conditions. This work is funded by NETL's Carbon Capture Simulation for Industry Impact ($CCSI^2$) program.

1.1.1 Intellectual Merit

Membrane modeling is necessary for the carbon capture field as it enables lab-scale membrane research to transition to pilot scale and then to full-scale adoption. The first portion of the thesis provides a literature review and analysis of state-of-the-art modeling techniques to simulate hollow fiber membrane (HFM) contactors for carbon capture in 1D, 2D and 3D. This review paper provides a detailed comparison of the assumptions needed to successfully model carbon capture membrane contactors, which is a much-needed contribution to the research field of carbon capture membrane modeling. The direct ocean

capture membrane model, presented in Chapter 2, is the first of its kind to use liquid solvent membrane contactors to remove CO_2 from seawater. While the impact of CO_2 on marine ecosystems is well-understood, preventative methods to reduce or reverse ocean acidification through carbon capture are few to none. This project will study direct ocean carbon capture using hollow fiber membranes and pioneer a new field of research through experiments and numerical models. In addition, the flat sheet membrane model developed (Chapter 4) is the first flat sheet membrane model to account for manufacturing variability in channel size. This model will enable us to determine the impact of manufacturing variability on CO_2 separation performance, which enables researchers to better compare flat sheet membranes to hollow fiber membranes. The results of that work will help membrane technology companies (e.g. MTR) to determine which membrane design is optimal for their carbon capture application.

1.1.2 Broader Impact

These projects will fundamentally benefit society by progressing the current state of membranes for carbon capture. The review paper assists with accelerating the adoption of hollow fiber membrane contactors for post-combustion carbon capture and provides structure to the modeling field. I applied these membrane modeling approaches to the emerging field of direct ocean capture to demonstrate a novel approach for removing CO_2 from seawater. The long-term goal of this project is to incorporate this technology into coastal systems to maintain healthy pH levels for high-risk ocean ecosystems (e.g. coral reefs, shellfisheries) while simultaneously performing negative emissions. Finally, the flat sheet model was developed for MTR, a leading company in membrane carbon capture, to aid with pilot testing their newest membrane technology and accelerate their product development to the market. This work helped predict accurate performance due to the incorporation of manufacturing malfunctions and essentially, accelerated pilot testing and minimized costs. These projects presented here have resulted in publications that accelerate research and technology in the carbon capture field, which is a vital research area to minimize global warming.

1.2 Publications

Published

1. **Rivero, Joanna R.**, Panagakos, Grigorios, Lieber, Austin, and Hornbostel, Katherine. "Hollow Fiber Membrane Contactors for Post-Combustion Carbon Capture: A Review of Modeling Approaches." Membranes, 10, 12, 2020, 382. https://doi.org/10.3390/membranes10120382
   - Featured in press release by University of Pittsburgh
   - Chapter 2 in this PhD Thesis
2. **Rivero, Joanna R.**, DaConceicao Acosta, Marcos, Hornbostel, Katherine, Lipscomb, Glenn. "Modeling gas separation in flat sheet membrane modules: Impact of flow channel size variation. Carbon Capture Science & Technology. March, 2023 https://doi.org/10.1016/j.ccst.2022.100093
   - Chapter 3 in this PhD Thesis

Submitted for Review

3. **Rivero, Joanna R.**, Snodgrass, Christoper, Lieber, Austin, Hildebrandt, Donna, Hornbostel, Katherine. "Demonstration of Direct Ocean Carbon Capture Using Hollow Fiber Membrane Contactors."
   - Submitted to Renewable & Sustainable Energy Reviews on October 14, 2022.
   - Chapter 4 in this PhD Thesis
4. Leiber, Austin, **Rivero, Joanna R.**, Davidson, Shanna, Hildebrandt, Donna, Snodgrass, Christopher, Niepa, Tagbo, Hornbostel, Katherine. "Demonstration of Direct Ocean Carbon Capture Using Encapsulated Solvents."
   - Submitted to Renewable & Sustainable Energy Reviews on October 14, 2022.

Finishing Draft

5. DaConceicao Acosta, Marcos, **Rivero, Joanna R.**, Hornbostel, Katherine, Lipscomb, Glenn. "Membrane Gas Separations Module Modelling: A Comprehensive Review."

1.3 Conferences

Oral Presentations

1. "The Effect of Layer Height Variation on CO2 Separation Performance in a Flat Sheet Membrane" **Rivero, Joanna R.**, Nemetz, Leo, DeConceicao Acosta, Marco, Lipscomb, Glenn, Hornbostel, Katherine, *North American Membrane Society (NAMS) 2022.*

Poster Presentations

1. "Multiphysics Simulation of CO_2 Removal from Seawater using Hollow Fiber Membrane Contactors" **Rivero, Joanna R.**, Snodgrass, Christopher, Hornbostel, Katherine, *North American Membrane Society (NAMS) 2020.*
2. "Investigation of Membrane Contactors for Direct Ocean Capture," Lieber, Austin, **Rivero, Joanna R.**, Hildebrandt, Donna , Davidson, Shanna, Usman, Huda, Niepa, Tagbo, Hornbostel, Katherine, *NAMS 2021.*
3. "Plate-and-Frame Membrane Modeling for CO_2 Separation," **Rivero, Joanna R.**, DeConceicao Acosta, Marco, Nemetz, Leo, Lipscomb, Glenn, Hornbostel, Katherine, *NAMS 2021.*
4. "Investigation of Membrane Contactors for Direct Ocean Capture," Snodgrass, Christopher, **Rivero, Joanna R.**, Hildebrandt, Donna, Lieber, Austin, Davidson, Shanna, Usman, Huda, Niepa, Tagbo, Hornbostel, Katherine, *Ocean Visions Summit 2021.*
5. "Modeling the Impact of Channel Size Variation for CO_2 Separation in Flat Sheet Membranes", **Rivero, Joanna R.**, DeConceicao Acosta, Marco, Nemetz, Leo, Lipscomb, Glenn, Hornbostel, Katherine, *NAMS 2022.*
6. "Modeling the Impact of Channel Size Variation for CO_2 Separation in Flat Sheet Membranes", **Rivero, Joanna R.**, DeConceicao Acosta, Marco, Nemetz, Leo, Lipscomb, Glenn, Hornbostel, Katherine, *Carbon Capture, Utilization and Storage - Gordon Research Seminar 2022.*

2.0 "Hollow Fiber Membrane Contactors for Post-Combustion Carbon Capture: A Review of Modeling Approaches"

Hollow fiber membrane contactors (HFMCs) can effectively separate CO_2 from post-combustion flue gas by providing a high contact surface area between the flue gas and a liquid solvent. Accurate models of carbon capture HFMCs are necessary to understand the underlying transport processes and optimize HFMC designs. There are various methods for modeling HFMCs in 1D, 2D, or 3D. These methods include (but are not limited to): resistance-in-series, solution-diffusion, pore flow, Happel's free surface model, and porous media modeling. This review paper discusses the state-of-the-art methods for modeling carbon capture HFMCs in 1D, 2D, and 3D. State-of-the-art 1D, 2D, and 3D carbon capture HFMC models are then compared in depth, based on their underlying assumptions. Numerical methods are also discussed, along with modeling to scale up HFMCs from the lab scale to the commercial scale.

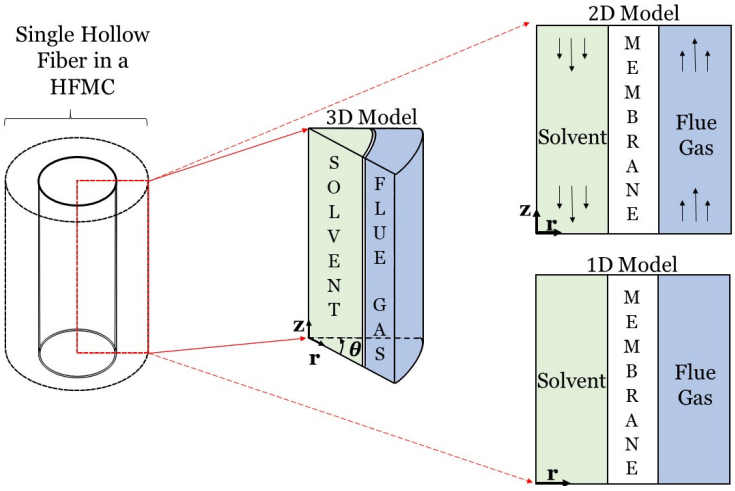

Figure 1: Graphical abstract highlighting the modeling dimensions that can be applied to simulate a hollow fiber membrane contactor. The manuscript specifically shows the modeling dimensionality for carbon capture from flue gas (blue) using absorption processes (solvent is shown in green).

2.1 Nomenclature

Subscripts

l	liquid
m	membrane
g	gas
ov	overall
eff	effective
i	inner
o	outer
h	hydraulic
w	liquid pore
f	membrane pore
max	maximum
r	radial coordinate
CO_2	CO_2 in a domain
θ	tangential
z	axial coordinate
avg	average
A	component
rxn	reaction
t	time
i	domain
th	thermal
j	species

Acronyms

HFM	Hollow fiber membrane
HFMC	HFM contactor
CC	Carbon capture
PCC	Post-combustion carbon capture
RIS	Resistance in series
MTC	Mass transfer coefficient
CFD	Computational Fluid Dynamics

Variables

k	resistance
D	diffusion coefficient
ε	porosity
τ	tortuosity
δ	thickness
d	diameter
L	length
E	enhancement factor
C	concentration
R	fixed radius
r_A	reaction rate constant
φ	volume fraction
γ	surface tension
m	solubility of CO_2
V	volume
κ_D	Darcy permeability
κ_1	inertial permeability
x^*	wetting ratio
$\boldsymbol{v}$	velocity vector
$\dot{v}$	volumetric flow rate
η	effective capture ratio
a	interfacial area
H	Henry's constant
P	partial pressure
B	pore geometry coefficient
T	temperature
θ	contact angle
n	number of fibers
ρ	density
μ	viscosity
$\boldsymbol{g}$	gravity
$\dot{n}$	molar flow rate
∂	partial differential
$\triangle$	difference
$\boldsymbol{b}$	body force vector
$\boldsymbol{L}$	gradient of velocity
f	constitutive parameter

2.2 Introduction

In 2018, the Intergovernmental Panel on Climate Change issued a report detailing the irreversible impact of a global temperature rise of 1.5 °C [12]. Though many countries are transitioning towards clean energy, a complete infrastructural shift from fossil fuels may take several decades. Carbon capture technology is critical to bridge the gap during this transition. Furthermore, natural gas plants may be necessary long-term to provide cheap baseload power to supplement intermittent renewable sources. Coal-fired and natural gas power plants in the United States are a target market for carbon capture (CC). This is because coal-fired power plants contribute 973 Million metric tons (MMmt) of CO_2 to the atmosphere annually [142], and natural gas power plants contribute about 619 MMmt [71]. State-of-the-art methods for power plant CC include (but are not limited to): physical and chemical solvation and adsorption, cryogenic separation, and membrane separation [69, 254]. Membrane-based methods offer several distinct advantages, including: minimal energy input, smaller unit footprint, ease of retrofit and replacement, quick response to power plant dynamics, and environmental friendliness.

Most membrane CC technologies flow power plant flue gas on one side and pull a vacuum on the other side to drive CO_2 diffusion. These membrane systems often pressurize the flue gas before it reaches the membrane to raise the CO_2 partial pressure difference across the membrane, which increases the rate of CO_2 diffusion. Pressurizing the flue gas, however, is energy-intensive and raises operating costs. Conventional CC membranes consist of a selective layer on top of a porous support layer to prevent nitrogen and other gaseous species from crossing over with the CO_2 [68]. These selective layers, however, raise the membrane cost and lower the flux of CO_2 because they add resistance to CO_2 transport.

One alternative design to conventional CC membranes is the membrane contactor, which enables gas exchange between two fluid streams [156]. Membrane contactors use a fluid sweep instead of a vacuum to drive CO_2 across the membrane. Membrane contactors that use a liquid solvent sweep are particularly effective because the solvent is selective to CO_2 over other gas species. This means that the membrane does not need a selective layer to block other gases, which can lower membrane cost and boost CO_2 flux.

Many gas-liquid membrane contactors use carbon capture solvents, which react with CO_2, driving more CO_2 across the membrane. Although energy is required to then strip CO_2 from the solvent in a regeneration process, gas-liquid membrane contactors have several competitive advantages over other membrane configurations: no need to pressurize the flue gas (which requires a lot of energy), higher CO_2 fluxes, no selective layer, and independent flow regulation [24]. Another advantage for membrane contactors is that the mass transfer resistance from the membrane is minimum in comparison to the gas and liquid mass transfer resistance. However, if membrane wetting occurs, the mass transfer resistance on the membrane increases and result in poor separation performance [24]. Gas-liquid membrane contactors used in

post-combustion carbon capture (PCC) are the focus of this review paper.

The membrane in a membrane contactor is generally thin and has a high surface area per unit volume to promote CO_2 transfer. Material selection is half of the challenge when designing a CC membrane contactor. The optimal materials for a CC membrane depend on the makeup and flow rate of the feed gas, system operating conditions, and separation requirements [109]. Although membrane contactors do not require a selective layer (because the solvent is already selective to CO_2), they often require a thin coating to prevent membrane wetting. The main membrane material must also be designed to withstand prolonged contact with flue gas and with the solvent of choice. Many experimental studies have been conducted to study the performance and lifespan of different membrane material and solvent combinations. Tables 1 and 2 cover several common solvents and membrane materials used in PCC gas-liquid membrane contactors [247].

It should be noted that both physical and chemical solvents are used in the field of CC. For the physical solvent, there is no chemical reaction as the system is based purely on gas solubility. However, once a chemical solvent is added to the system, there is a chemical reaction on the solvent side. Although this review paper focuses primarily on modeling membrane contactors, other review papers have done a comprehensive job of comparing membrane materials and physical and chemical solvents [24, 118, 109, 108, 42]. The reaction modeling for membrane contactors using solvents will not be discussed in this review paper. However, the papers cited in Table 1 provide a good starting point for modeling reaction chemistry for these common solvents. Common membrane materials are shown in Table 2.

Table 1: Summary of common solvents used in hollow fiber membrane contactors (HFMCs) for CO_2 separation from flue gas.

Water (H_2O)	[8, 80, 33, 34]
Monoethanolamine (MEA)	[80, 34, 35, 50, 81, 130, 79, 220, 186]
Diethanolamine (DEA)	[252, 95, 231, 186]
Sodium Hydroxide (NaOH)	[64, 159]
Methyldiethanolamine (MDEA)	[200, 217, 114]

Table 2: Summary of common membrane materials used in hollow fiber membrane contactors (HFMCs) for CO_2 separation from flue gas.

Polypropylene (PP)	[8, 252, 95, 79, 65]
Polytetrafluoroethylene ($PTFE$)	[80, 130, 162]
Polyvinylidene fluoride ($PVDF$)	[50, 252, 82, 79, 172, 60, 159]
Polymethylpentene (PMP)	[50]

Carbon capture membrane contactors come in many configurations: tubular/hollow-fiber [67], spiral wound [100], and flat sheet [40]. A common geometric configuration used in PCC is the hollow fiber membrane contactor (HFMC), and this particular design will be the focus of this review paper. HFMCs consist of many long, narrow, hollow fibers packed into bundles. HFMCs are manufactured by first creating a woven fabric-like bundle using a rotating wheel [165]. The ends of the bundle are then fused shut and undergo centrifugal potting to form a tubesheet. This tubesheet's ends are then cut to recreate open-ended fibers. The bundle with tubesheet ends is then placed inside a case that has two ports for the permeate fluid and two headers at each end for the inside of the hollow fiber, known as the lumen access port [230]. HFMCs for PCC systems are relatively inexpensive, have a high surface area per unit volume, and are easy to seal, preventing leakage. HFMCs are also relatively easy to model compared to other CO_2 separation methods due to their simple geometry and flow configuration. HFMCs are commonly operated in a counter-flow configuration (where the sweep gas or solvent runs in the opposite direction that the exhaust gas flows). However, they can also be operated in co-flow (where sweep runs in the same direction to the exhaust) or in cross-flow (where sweep runs perpendicular to the exhaust), as seen in Figure 2.

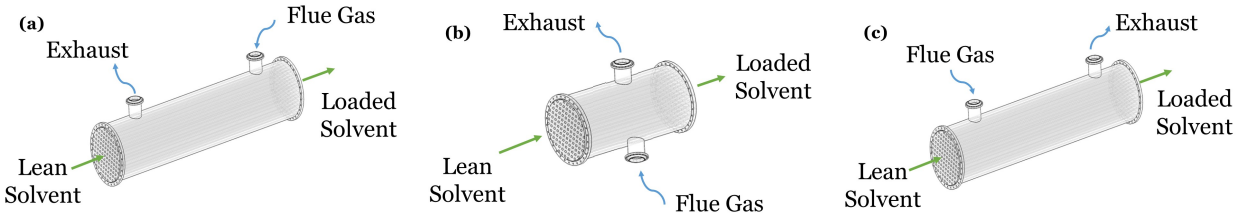

Figure 2: Illustration of flow patterns of a gas-liquid HFMC for post-combustion carbon capture (PCC) (**a**) counter-current flow, (**b**) cross-flow, and (**c**) co-current flow.

A common performance metric for HFMCs is the percentage removal rate, defined as follows [79, 216]:

$$\%\text{ removal of } CO_2 = 100\left(1 - \frac{C_{CO_2,outlet}}{C_{CO_2,inlet}}\right) = 100\left(\frac{(\dot{n})_{inlet} - (\dot{n})_{outlet}}{(\dot{n})_{inlet}}\right), \tag{2.1}$$

where $\dot{n}[\frac{mol}{s}]$ is the molar flow rate defined as the volumetric flow rate times the concentration, $\boldsymbol{\dot{v}} C_{CO_2}$, or, in a more general sense, $\int_S \boldsymbol{u} C \, d\vec{S}$. Another common performance metric in CC HFMCs is the effective capture ratio, η, which is a function of interfacial area, $a[m^2]$, gas velocity $v_g[\frac{m}{s}]$, fiber length, $L[m]$, and the inverse of the CO_2 transfer time, K [255]:

$$\eta = 1 - exp\left(\frac{-KaL}{v_g}\right). \tag{2.2}$$

There are already several review papers on the topic of HFMCs for PCC. An in-depth explanation of gas-liquid HFMCs is offered by Gabelman et al., who address theoretical and

design considerations, mass transfer performance and applications [90]. Ji et al. give a more recent theoretical and application-specific review on membrane-based technology, including HFMCs [120]. Optimization methods, experimental approaches, and energetic and economic evaluations have been performed on HFMCs to stress the highest packing density and lowest cost in comparison to other configurations [233]. Other HFMC review papers have focused on scale-up and industrial application of HFMC CO_2 capture technology [183, 174, 145, 24]. Some review papers also cover wetting effects and mass transfer correlations in 1D and 2D only [56, 50, 255].

These state-of-the-art HFMC review papers also focus on experimental work. A major challenge with performing experimental studies in this field is that it is difficult to translate bench-scale results to a commercial system, particularly when experimental studies do not report costs or system configurations [132]. It often takes over a decade to translate lab-scale technology to commercialization, and this process often requires multiple rounds of expensive pilot testing at facilities like the National Carbon Capture Center (NCCC) [182]. Modeling is necessary to expedite this scale-up process and guide experimental design to save time and money. Furthermore, experiments conducted in this field are often tailored to a unique set of membrane materials and operating conditions. This makes it challenging to compare reported experimental results or determine the optimal membrane contactor design. Modeling is needed to bridge this gap between disparate experimental results and determine the optimal design. Modeling and optimization can help minimize the many costs associated with membrane contactor systems (e.g., membrane materials, manufacturing, and operating costs [110]).

This paper offers a comprehensive review of modeling studies to date for gas-liquid HFMCs for PCC. The purposes of this review are: (1) to present the current field of HFMC carbon capture modeling, (2) to compare 1D, 2D, and 3D HFMC modeling approaches, and (3) to identify areas for future research in HFMC modeling. The paper is organized into 1D, 2D, and 3D modeling sections. These sections are followed by a section comparing the 1D, 2D, and 3D modeling approaches. Finally, numerical approaches and modeling to assist scaling up HFMC technology are discussed.

2.3 Fundamental Theory

Before presenting the theory of 1D, 2D, and 3D modeling, this section will briefly cover the governing equations and constitutive laws used to model HFMCs that can be found in related transport textbooks [27]. This is to stress the need of understanding the fundamentals of mass transport for successful modeling.

2.3.1 Constitutive Laws

The constitutive laws are needed to derive the relevant governing equations for a complete mass transfer analysis. These laws provide micro scale analysis (e.g., describe the molecule interaction) for a complete macro scale analysis (e.g., describe the bulk interaction). The constitutive laws are based on Fick's first law of diffusion (Equation (2.3)), and the strain-rate relationship (also known as Newton's law of viscosity):

$$\boldsymbol{J_j} = -D_j \nabla C_j, \tag{2.3}$$

$$\boldsymbol{\tau} = -\mu(\nabla \boldsymbol{v} + (\nabla \boldsymbol{v})^{\intercal}) + \left(\frac{2}{3}\mu - \kappa\right)(\nabla \cdot \boldsymbol{v})\boldsymbol{\delta}. \tag{2.4}$$

Fick's first law of diffusion is defined based on the diffusion coefficient, $D[\frac{m^2}{s}]$, the concentration, $C[\frac{mol}{m^3}]$, and the species, j. Newton's law of viscosity is defined based on the viscous momentum flux tensor, $\boldsymbol{\tau}[Pa]$, the velocity vector, $\boldsymbol{v}[\frac{m}{s}]$, the fluid viscosity $\mu[Pa \cdot s]$, and the unit tensor, $\boldsymbol{\delta}$. Previous work also assumes monatomic gases at low density, making the dilatational viscosity, κ, equal zero.

In the case heat transfer is being considered, Fourier's law should be considered to derive the thermal energy equation:

$$\boldsymbol{q} = -k \nabla T. \tag{2.5}$$

For Equations (2.3)–(2.5), the material properties do not have to be constant and can be functions of parameters of the system, such as temperature, concentration, and pressure.

2.3.2 Governing Equations

The governing equations of motion used throughout this analysis are the conservation of mass, linear momentum, convection–diffusion, and energy equations [219, 224, 163]. The conservation of mass equation, also known as the continuity equation for species, is derived from Fick's first law of diffusion (Equation (2.3)).

$$\frac{\partial C_j}{\partial t} + \nabla \cdot (C_j \boldsymbol{v}) = r_j + f. \tag{2.6}$$

Equation (2.6) considers the concentration, $C[\frac{mol}{m^3}]$; the velocity vector, $\boldsymbol{v}[\frac{m}{s}]$; the reaction rate, $r_j[\frac{mol}{m^3 s}]$; and a constitutive parameter, f, as a function that is to be determined by the constitutive theory [163]. The equation of motion in terms of the viscous momentum flux (Equation (2.4)) and the continuity equation (conservation of mass) is shown below:

$$\rho \frac{D\boldsymbol{v}}{Dt} = \nabla \cdot \boldsymbol{\tau} + \rho \boldsymbol{b}, \tag{2.7}$$

$$\frac{\partial \rho}{\partial t} + \nabla \cdot (\rho \boldsymbol{v}) = 0, \tag{2.8}$$

where $\frac{D}{Dt}$ is the substantial time derivative, given by: $\frac{\partial}{\partial t} + \nabla(\,)\boldsymbol{v}$. $\boldsymbol{b}$ is the body force vector, $\boldsymbol{v}[\frac{m}{s}]$ is the velocity vector, and $\rho[\frac{kg}{m^3}]$ is the density. Equation (2.7) can be derived if Equation (2.6) is written in a per mass basis and summed over all species j.

In the case where non-isothermal conditions are considered, the energy equation, derived from Equation (2.5), should also be included in the transport analysis [52].

$$\rho \frac{D\epsilon}{Dt} = \boldsymbol{\tau} \colon \boldsymbol{L} - \nabla \cdot \boldsymbol{q} + r_{rxn} \Delta H_{rxn} M. \tag{2.9}$$

Equation (2.9) includes the substantial time derivative, $\frac{D}{Dt}$; the specific internal energy, ϵ; the gradient of the velocity, L; the heat flux vector from Equation (2.5), $\boldsymbol{q}$; and the total reaction rate $r_{rxn}[\frac{mol}{m^3 s}]$, multiplied by the enthaply, $\Delta H_{rxn}[\frac{J}{kg}]$; and the molecular weight, $M[\frac{kg}{mol}]$.

2.4 One-Dimensional Modeling

Dimensionality reduction is a convenient, established, and powerful method for simplifying the system of the coupled partial differential equations (PDEs) that need to be solved for an adequate modeling representation of physico-chemical phenomena and devices, decreasing drastically the computational cost of any numerical implementation. If symmetry around an axis along the longitudinal direction of a HFMC can be justified, a 3D hollow fiber can be as reduced and effectively studied by a 2D model, where angular variations can be ignored for both concentration and velocity, e.g., Reference [217, 215, 198, 220, 184, 189, 4, 92]. Further simplification can be achieved, if translational invariance for the fluid flow is also imposed upon our model along the longitudinal direction, making the axial component of the velocity dependent only on the radial coordinate [43]. An additional reasonable assumption can also be made based on the fact that the dominant component of the mass-transfer driving force, is usually perpendicular to the direction of the flow [27]. All the above taken together, result in an 1D model, where angular and axial variations of mass transfer can be neglected [236]. This section focuses on 1D models of carbon capture HFMCs. As shown in Figure 3, the radial dimension, or r, is typically the one dimension that is resolved in 1D HFMC models [33, 35, 95]. Although the flue gas and solvent streams can flow on either side of the fiber, we assume in Figure 3 and the following equations that solvent flows on the tube-side and that flue gas flows on the shell-side, like, for example, in Reference [215]. All theory presented in this paper will consist of three domains: the tube, membrane, and shell domains. One-dimensional models of HFMCs should either include a mass transfer coefficient or a model that describes the permeate(s) passing through the membrane. This section will focus

first on using the resistance-in-series method to calculate mass transfer coefficients. The solution-diffusion and pore flow models will then be discussed briefly.

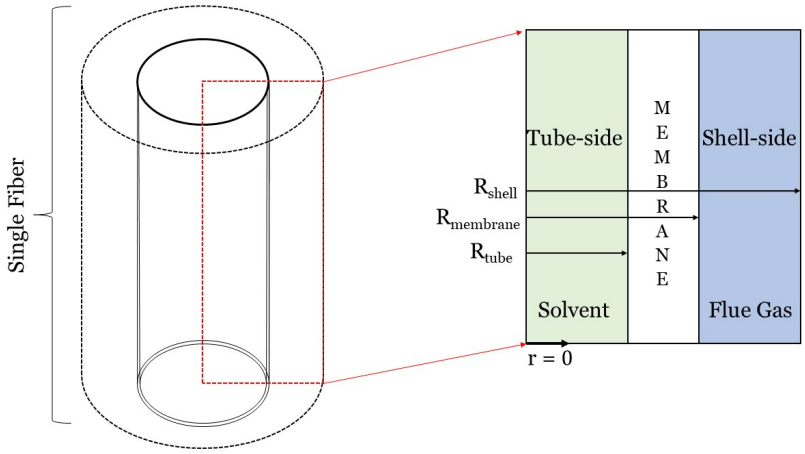

Figure 3: Graphic of the one-dimensional modeling framework for a gas-liquid HFMC. The radial dimension is the one dimension of interest; variations in the axial and angular dimensions are not taken into account. Liquid solvent flows through the inside or "tube-side" of the fiber, while flue gas flows outside or on the "shell-side" of the fiber.

2.4.1 Resistance-In-Series (RIS) Model

The resistance-in-series (RIS) approach is often used to model the overall mass transfer coefficient (MTC) of individual fibers. For the purpose of this review paper, the RIS model will be considered as a 1D model with the mass transfer occurring in the radial direction. The RIS method is widely applicable to HFMC models and can even be used to model multi-stage HFMCs and a range of flow patterns [32, 35]. It is a simple, effective means of determining the rate of CO_2 transfer in HFMCs. The RIS method relies on mass transfer resistances, which are analogous to electrical resistors wired in series [111]. RIS is a simple method that breaks down the mass transfer process in a carbon capture HFMC into a series of steps: CO_2 diffusion through the gas, CO_2 diffusion through the membrane, and CO_2 diffusion through the liquid (as shown in Figure 4). The RIS model for HFMCs is derived from double-film theory, where two fluids (i.e., two films) are considered with a membrane in between [156]. The double-film theory describes mass transfer resistance at the interface(s), or "film(s)", of the liquid, porous media, and gas phases [50]. Figure 4 illustrates the mass transfer through a non-wetted porous membrane for the three domains, where P_A is the partial pressure of component A in the gas phase, and C_A is the liquid concentration of component A.

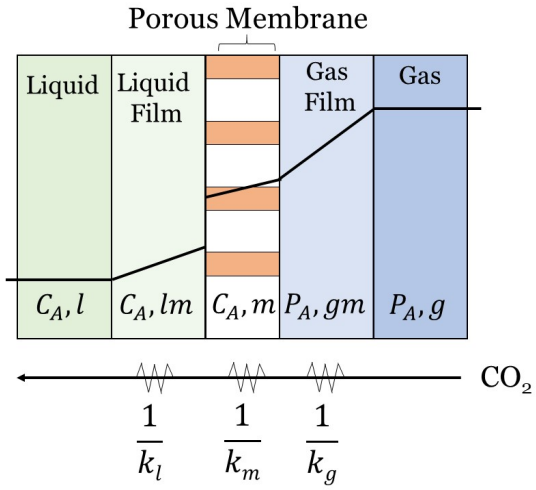

Figure 4: A resistance-in-series (RIS) illustration for CO_2 crossing a membrane in a HFMC. There are mass transfer resistances associated with the gas phase, the membrane, and the liquid phase. Each resistance can be expressed as the inverse of the mass transfer coefficient for that phase. The layers included to accomplish this analysis are the gas, gas film, membrane, liquid film, and liquid.

The RIS model calculates the overall mass transfer coefficient (MTC) that is needed to calculate the flux:

$$J_{CO_2} = k_{ov} \Delta C_{CO_2}. \tag{2.10}$$

The following assumptions and law's are used to derive the overall MTC ($k_{ov}[\frac{m}{s}]$) [20]. A phase equilibrium is assumed at the gas-liquid interface. Fick's first law of diffusion (Equation (2.3)) and Henry's law (Equation (2.11)) for gas-liquid systems are also applied to derive the final flux equation:

$$H = \frac{C_{CO_2,l}}{P_{CO_2,g}}. \tag{2.11}$$

Equation (2.3) is Fick's first law of diffusion, where the flux is defined as the moles of a species moving past a region over a given length. Equation (2.11) shows the relationship between the concentration of CO_2 and the partial pressure of CO_2. This relationship produces Henry's constant, H, to account for physical solubility of CO_2 at the gas-membrane interface. Luis et al. [156] goes through the steps of applying these assumption's and law's to derive the overall MTC and the final flux equation (Equation (2.10)).

With each layer that CO_2 diffuses through in Figure 4, the mass transfer resistance of that layer is the inverse of the mass transfer coefficient of that layer ($R_i = 1/k_i$). Henry's constant (H) must also be included in the domain interface resistance to account for solubility

of gas in the liquid phase. The overall MTC can then be determined by summing these three resistances, as shown in Equation (2.12):

$$\frac{1}{k_{ov}} = \frac{1}{k_l} + \frac{1}{k_m} + \frac{H}{k_g}. \tag{2.12}$$

Equation (2.12) expresses the overall MTC, $k_{ov}[\frac{m}{s}]$, as a function of the MTCs of the liquid, membrane, and gaseous phases: k_l, k_m, and k_g, respectively [167, 206, 203]. The membrane MTC, k_m, is determined by Equation (2.13):

$$k_m = \frac{D_{eff}}{\delta}, \tag{2.13}$$

where the effective diffusivity in the membrane, $D_{eff} = D_{CO_2}\frac{\varepsilon}{\tau}$, is defined as the ratio of the porosity to tortuosity of the membrane in $[\frac{m^2}{s}]$, and $\delta[m]$ is the thickness of the membrane [177]. D_{eff} is determined using the Fickian, Maxwellian (if it is a multi-component system), and Knudsen gas diffusion coefficients [136]. The gas- and liquid-layer MTCs, k_g and k_l, are determined using the following correlations:

$$k_g = \frac{ShD_{CO_2,g}}{d_h}, \tag{2.14}$$

$$k_l = \frac{ShD_{CO_2,l}}{d_i}, \tag{2.15}$$

where Sh is the Sherwood number, $d_i[m]$ is the inner fiber diameter, and $D_{CO_2,g}$ and $D_{CO_2,l}$ are the diffusivities of CO_2 in the gas and liquid domains, respectively, in $[\frac{m^2}{s}]$. Equations (2.14) and (2.15) assume that liquid flows inside the fibers while gas flows on the shell side, as shown in Figure 3. If gas is flowing on the tube side and gas through the fibers, then the d_i and d_h terms in these equations need to be swapped. The gas and liquid MTCs should be modeled with respect to the system setup to consider the correct diameters (d_i or d_h). There is no standard for where the solvent should flow (either the tube- or shell-side), but the hydraulic diameter should be modeled accordingly. Zhao et al. discuss the advantages and disadvantages of modeling the solvent on the tube- and shell-side [255].

The following correlations proposed by Yang and Cussler can be used to determine the Sherwood number for laminar flow on the tube-side and the shell-side of the fibers, respectively, [240]:

$$Sh_{tube} = 1.62\left(\frac{d_i Re}{L}\right)^{0.33}, \tag{2.16}$$

$$Sh_{shell} = 1.25\left(\frac{d_h Re}{L}\right)^{0.93} Sc_{CO_2}^{0.33}, \tag{2.17}$$

where $L[m]$ is the length of the fiber; $Sc_{CO_2} = \frac{\nu_{CO_2}}{D_{CO_2}}$ is the Schmidt number defined using

the kinematic viscosity, $\nu[\frac{m^2}{s}]$; $Re = \frac{\rho V d}{\mu}$ is the Reynolds number defined using the dynamic viscosity, $\mu[Pa \cdot s]$; d_h is the hydraulic diameter; and d_i is the inner diameter. These Sherwood correlations can be applied to gas or liquid phase flows on either side of the membrane. These correlations are specific to the geometric configuration shown in Figure 3, where solvent flows on the tube-side and flue gas flows on the shell-side of a cylindrical fiber. Additional mass transfer correlations for different configurations are covered in Table 2 of Cui et al.'s review paper on HFMCs for CO_2 capture [191].

2.4.1.1 Modeling Chemical Reactions in RIS

If a chemical reaction needs to be modeled, this can be incorporated into the RIS model by using a dimensionless enhancement factor, E. The enhancement factor is the ratio of mass transfer rate with reaction to the mass transfer rate without reaction. Equation (2.12) can thus be modified to incorporate the CO_2 absorption reaction [61, 138], as shown in Equation (2.18):

$$\frac{1}{k_{ov}} = \frac{H d_o}{k_l d_i E} + \frac{d_o}{k_m d_{lm}} + \frac{1}{k_g}. \tag{2.18}$$

The inner, outer, and mean logarithmic diameters of the fiber (d_i, d_o, d_{lm}) are also incorporated into this equation to account for the different diameters where each mass transfer step occurs [156]. For a system considering only a physical absorption, $E = 1$ [57]. For a system considering chemical solvents, E is determined by the infinite enhancement factor (E_∞) and the Hatta number (Ha) [91]. Zhao et al. [255], Cussler et al. [57], and Gaspar et al. [91] provide more information on how to incorporate the enhancement factor into the RIS equation when the reaction is the limiting, partially limiting, or not the limiting step in the overall mass transfer process.

Incorporating an enhancement factor into the RIS model is just one technique for modeling reaction chemistry in HFMCs. However, more often than not, the overall MTC determined by RIS is coupled with a separate solvent reaction chemistry model, as presented in Section 2.5. This approach is more accurate than using an enhancement factor because it incorporates a more detailed set of reactions coupled with transport and conservation equations. Details on how to model the absorption reaction on the liquid side for 1D models using common solvents can be found in Reference [147, 159].

2.4.1.2 Modeling Membrane Wetting in RIS

The examples and discussion so far have focused on ideal HFMCs. Actual HFMCs may experience membrane wetting over time, as reported in some HFMC experiments [95, 204]. Membrane wetting is due to the surrounding environment, chemical reactions, changes in geometry (such as pore swelling), and capillary condensation [16]. To model membrane

wetting in HFMCs, the following assumptions must be made: (1) membrane thickness, δ, is the total pore length, and (2) pores have a doughnut structure (in order to apply the Laplace-Young equation).

For 1D HFMC models, membrane wetting can be incorporated into the RIS equation. The RIS equation for a fully wetted membrane with reaction chemistry is given by [156]:

$$\frac{1}{k_{ov}} = \frac{Hd_o}{k_l d_i E} + \frac{Hd_o}{k_m d_{lm}} + \frac{1}{k_g}, \tag{2.19}$$

where k_m is now defined using the thickness of the wetted part of the membrane, δ_{wetted} [149]:

$$k_m = \frac{D_{eff}}{\delta_{wetted}}. \tag{2.20}$$

However, a more realistic model is a partially wetted HFMC, where the pores are filled with both gas and liquid [175]. In this case, additional resistances (as shown in Figure 5) can be added to the equation using a parameter known as the wetting ratio:

$$x^* = \frac{V_w}{V_f}, \tag{2.21}$$

where V_w is the volume of liquid in the pore, and V_f is the pore volume of the membrane, given by $V_f = n_p \pi \varepsilon (r_o^2 - r_i^2) L$. The pore volume of the membrane depends on the number of pores, n_p; the membrane porosity, ε; the fiber length, L; and the outer and inner radii of the fiber: r_o and r_i, respectively.

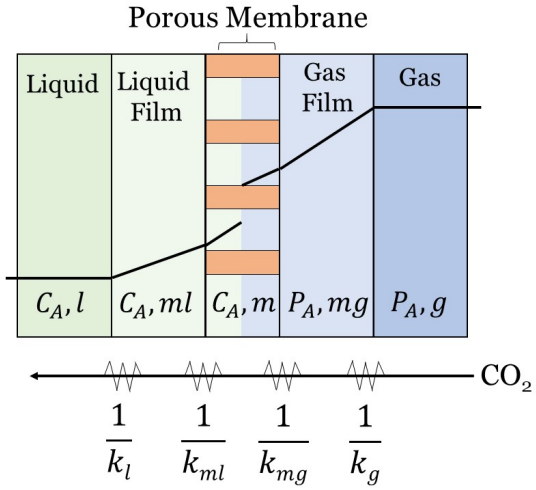

Figure 5: A resistance-in-series illustration for CO_2 crossing a membrane in a HFMC with partial membrane wetting, where both liquid and gas fill the membrane pores.

The RIS equation for a partially-wetted membrane with reaction chemistry is given by:

$$\frac{1}{k_{ov}} = \frac{Hd_o}{k_l d_i E} + \frac{Hd_o x^*}{k_{ml} d_{lm}} + \frac{d_o}{k_{mg} d_{lm}} \left(1 - x^*\right) + \frac{1}{k_g}, \tag{2.22}$$

where the term with x^* accounts for the wetted portion of the membrane, and the term with $(1 - x^*)$ accounts for the non-wetted portion of the membrane. k_{ml} is the membrane mass transfer coefficient for the liquid-filled pores, and k_{mg} is membrane mass transfer coefficient for the gas-filled pores. Sometimes these extra resistances can make the total membrane resistance account for >90% of the overall mass transfer resistance, which underscores the importance of accounting for membrane wetting in models [130, 56]. Membrane wetting can be reduced or eliminated by using a dense skin layer [137]. This can decrease the overall MTC by two or three orders of magnitude [211].

When modeling membrane wetting effects, membrane parameters, such as pore size and distribution, must also be accounted for [33, 34, 206]. Membrane wetting can vary along the length of a membrane as transmembrane pressure varies along a membrane [255]. The transmembrane pressure is defined as the pressure difference across the membrane. Membrane wetting is determined by comparing the breakthrough pressure to the transmembrane pressure [199]. The breakthrough pressure, defined in Equation (2.23), should be used as the critical pressure to determine if the liquid will penetrate into the pores of the membrane and cause membrane wetting [88, 156]:

$$\triangle P = -\frac{4B\gamma cos\theta}{d_{max}}. \tag{2.23}$$

Equation (2.23), known as the Laplace-Young equation, depends on the surface tension of the liquid, $\gamma[\frac{N}{m}]$; the contact angle, θ; and the maximum pore diameter, $d_{max}[\mu m]$. d_{max} is the critical pore diameter, which dictates whether or not membrane pores are wetted. If membrane pore diameter is greater than or equal to d_{max}, then the pores should be modeled as wetted [33, 34]. Pore shape is accounted for in the pore geometry coefficient, B, where $B = 1$ for perfectly cylindrical pores, and $0 < B < 1$ for non-cylindrical pores [255].

2.4.2 Solution-Diffusion Model

The solution-diffusion model is a standard 1D model for dense, non-porous polymeric membranes and as such is not frequently encountered for modeling HFMCs. The permeants are separated because of the differences in the solubilities and the variations in the diffusive rates of the different flue gas species in the membrane. This transport mechanism occurs in the reverse osmosis, pervaporation, and polymeric gas separation membranes. The lack of micro-pores, reasonably justifies the assumption of constant pressure throughout the membrane and the concentration difference being the mass-transfer's driving force [131]. This model follows gaseous CO_2 as it undergoes a three-step process (shown in Figure 6): (1) CO_2

sorption onto the membrane's on the gas side, (2) CO_2 diffusion through the membrane, and (3) CO_2 desorption from the solvent side of the membrane [119, 11].

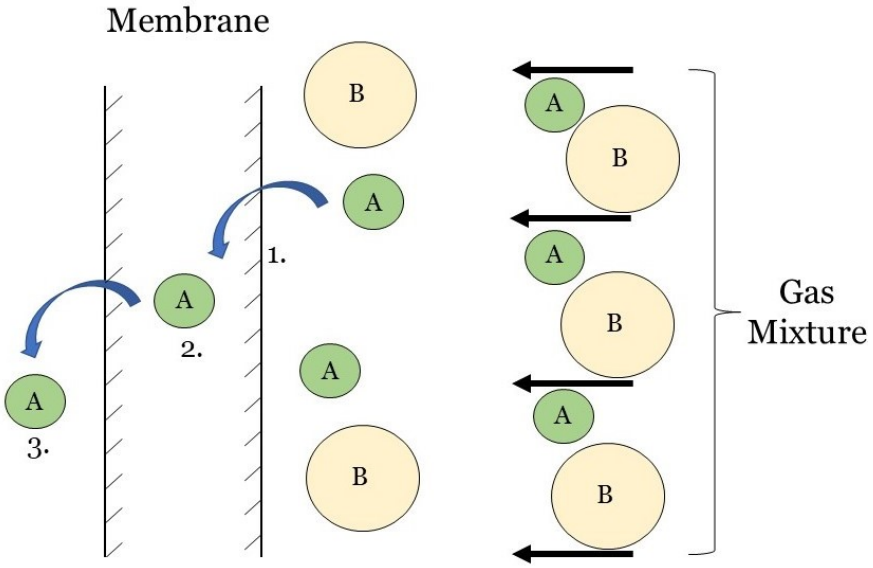

Figure 6: Graphical depiction of the solution-diffusion three-step process in a carbon capture HFMC for gas mixture of molecule A and B: 1. Molecule A sorption at the gas-membrane interface, 2. Molecule A diffusion through the membrane, and 3. Molecule A desorption at the solvent-membrane interface. The permeants are separated because of the differences in the solubilities and the variations in the diffusive rates of the different flue gas species in the membrane [119, 11].

To apply the solution-diffusion model, the following assumptions must be made: (1) the rates of absorption and desorption at the interfaces are much higher than the rate of diffusion through the membrane, (2) equilibrium is assumed between fluids and membrane at the interfaces, (3) there are no visible pores, (4) pressure within the membrane is constant, and (5) the chemical potential is represented only by the concentration gradient. The solution-diffusion model is naturally characterized by Fick's first law of diffusion (Equation (2.3)), which gives the flux of a gaseous species as a function of concentration gradient [55]. Notwithstanding the fact that solution-diffusion model is not endemic to HFMC, it has been reported to predict HFMC behavior in industrial settings [166] and in power plants [131]. The solution-diffusion model is also a quick way to represent membranes to perform membrane system optimization [51] and minimize failure [244, 36]. It has also been used to model multi-component flue gas systems and non-isothermal conditions [228].

2.4.3 Pore Flow Model

Another 1D membrane modeling approach is the pore flow model. Unlike dense polymeric membranes, for applications, like ultrafiltration, microfiltration, and microporous gas flow membranes, the membrane consists of a network of micro-pores. The separation is achieved as a result of filtering, as only species with molecular sizes less than the size of the pores can permeate through the membrane. A direct consequence of the separation mechanism is that the concentration in the membrane is assumed constant, and gas transfers across the membrane by pressure-driven convective flow through the pores as shown in Figure 7 [55, 20]. The pore-flow model can be described on the macro-scale by Darcy's law. For CO_2 as the permeating species:

$$J_{CO_2} = -\frac{k_D}{\mu} C_{CO_2} \frac{\partial P}{\partial x}, \tag{2.24}$$

where $k_D[m^2]$ is the Darcy's Law coefficient, $\frac{\partial P}{\partial x}[\frac{Pa}{m}]$ is the pressure gradient across the membrane thickness, $\mu[Pa \cdot s]$ is the viscosity, and $C_{CO_2}[\frac{mol}{m^3}]$ is the concentration. Both the solution-diffusion and pore flow model are capable of modeling 1D gas transport through a membrane. The main distinction between the two is that concentration difference drives transport in the solution-diffusion model, whereas pressure difference drives transport in the pore flow model. Additionally, the membrane material (i.e., the size and permeance of the pores) is an important factor to consider as it determines which model should be used. The solution-diffusion model is recommended for membranes with pore sizes below 5 Å, while the pore flow model is recommended for membranes with pore sizes of 10–1000 Å.

The RIS method, solution-diffusion model and pore flow model can each accurately represent the physics of CO_2 removal from flue gas in HFMCs. The RIS method uses an estimated overall MTC to estimate the CO_2 flux across the membrane. The solution-diffusion and pore flow models, on the other hand, do not require a MTC to be calculated. Instead, the solution-diffusion model relies on Fick's first law of diffusion to represent the permeance of CO_2 through the membrane as a function of concentration, and the pore flow model uses Darcy's law and pressure difference to determine CO_2 flux. RIS is the most popular method for 1D modeling of HFMCs. The RIS method has the advantage of being able to represent membranes that have both porous and nonporous portions [144]. One-dimensional models using these three approaches can accurately match experimental results, as well as 2D and 3D models [245, 98]. The main drawback of 1D models is that they cannot capture more complex dynamics inside a HFMC fiber or bundle (e.g., concentration profiles, flow distributions), which is where 2D and 3D models add value.

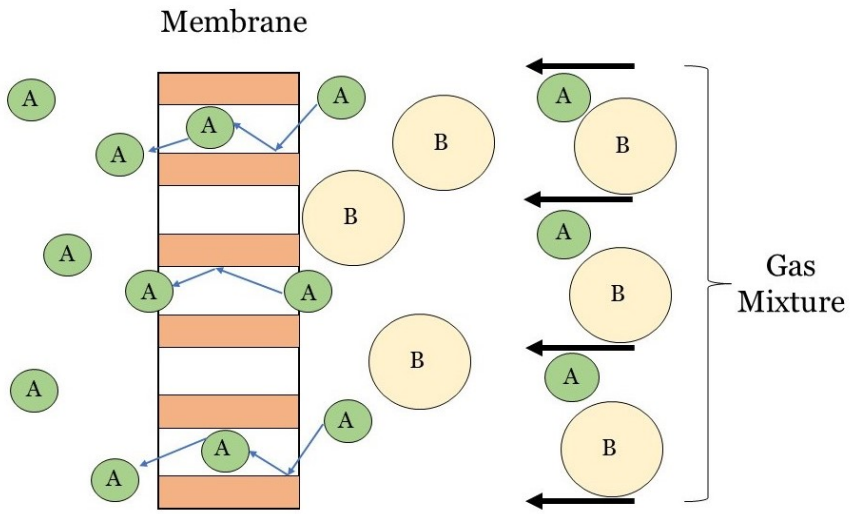

Figure 7: Graphical depiction of the pore flow model, where molecule A crosses the membrane due to a pressure difference. The illustration is not drawn to scale to emphasize the flow through permanent pores [55, 20].

2.5 Two-Dimensional Modeling

Two-dimensional modeling of carbon capture HFMCs typically consists of modeling a single hollow fiber. However, 2D modeling can more precisely account for physics and transport than 1D models by incorporating axial diffusion and convection [114, 251, 64]. To computationally model axial and radial mass transfer characteristics (diffusion, convection, and chemical reactions), a complete mass transfer analysis is necessary using governing equations and constitutive laws. Figure 8 will be used throughout this section to walk through the theory that should be followed to complete a mass transfer analysis for a HFMC. Figure 8 illustrates the 2D modeling framework for a single hollow fiber in a counter-flow HFMC, where liquid solvent flows on the tube-side and flue gas flows on the shell-side. Once the general governing equations and laws are introduced, the equations and laws will be applied to the system presented in Figure 8. These equations will then be modified to account for membrane wetting. It should be noted that this section will demonstrate computation fluid dynamics (CFD) modeling theory behind a single 2D-axisymmetric hollow fiber. If one desires to develop a 2D model of a HFMC bundle, the results can simply be multiplied by the number of fibers in the bundle.

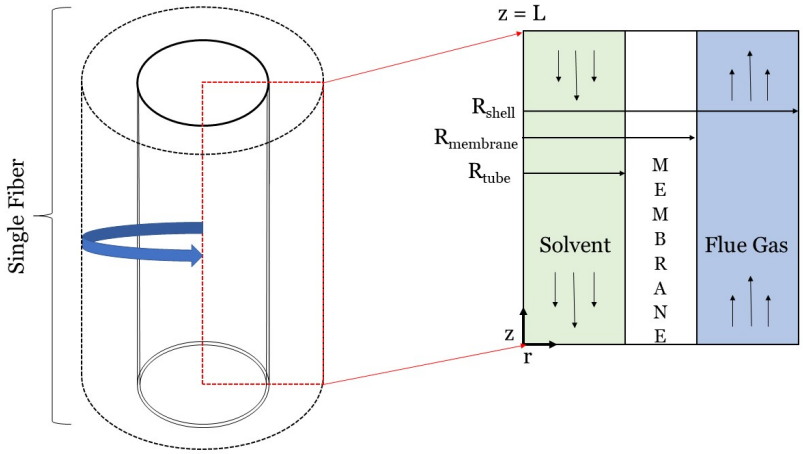

Figure 8: Graphic of the two-dimensional axisymmetrical modeling framework for a gas-liquid HFMC. The axial and radial dimensions are the dimensions of interest; variations in the angular dimension are not considered due to symmetry. In this graphic, solvent flows on the tube-side, while flue gas flows counter-flow on the shell-side.

2.5.1 Governing Equations for a 2D-Axisymmetric HFMC Fiber

Using as starting point the balances of mass, momentum and energy presented in Section 2.3 accompanied by the relevant constitutive laws and applying a set of assumptions, one can get to a system of partial differential equations that mathematically represent the physical setup. For the purposes of this analysis a popular set of assumptions comprises: steady state operation, rotational symmetry for both velocity and concentration fields, translational invariance for the fluid flow, constant material properties leading to incompressibility in the form of $\nabla \cdot \boldsymbol{u} = 0$, and constant membrane properties. The following equations are based on the cylindrical coordinates framework presented in Figure 8. The general mass balance for this system is given by Equation (2.25) and is derived from Equation (2.6) for a 2D-axisymmetric hollow fiber [27].

$$v_z \frac{\partial C_A}{\partial z} - r_A = D_A \frac{\partial^2 C_A}{\partial r^2} + \frac{D_A}{r}\frac{\partial C_A}{\partial r} + D_A \frac{\partial^2 C_A}{\partial z^2}, \tag{2.25}$$

where $D_A[\frac{m^2}{s}]$ and $C_A[\frac{mol}{m^3}]$ are the diffusion coefficient and the concentration of species A, respectively; $v_z[\frac{m}{s}]$ is the axial velocity component; and $r_A[\frac{mol}{m^3 s}]$ is the reaction rate of species A. Equation (2.25) will now be applied to each domain of the system (e.g., tube, membrane, shell) and modified to represent the physics occurring within each domain.

Modeling diffusion in the membrane domain is the simplest application because the chemical reaction rate and convection terms drop out. Therefore, Equation(2.25) reduces to

Equation (2.26) within the membrane:

$$0 = D_{CO_2-mem}\left(\frac{\partial^2 C_{CO_2}}{\partial r^2} + \frac{1}{r}\frac{\partial C_{CO_2}}{\partial r} + \frac{\partial^2 C_{CO_2}}{\partial z^2}\right). \tag{2.26}$$

In comparison, when Equation (2.25) is applied to the tube- and shell-side, additional mass transfer terms must be included. The 2D mass transport equations for the tube- and shell-side, respectively, are shown below [181, 4, 160, 184]:

$$v_{z,tube}\frac{\partial C_{CO_2}}{\partial z} - r_{CO_2} = D_{CO_2-tube}\left(\frac{\partial^2 C_{CO_2}}{\partial r^2} + \frac{1}{r}\frac{\partial C_{CO_2}}{\partial r} + \frac{\partial^2 C_{CO_2}}{\partial z^2}\right), \tag{2.27}$$

$$v_{z,shell}\frac{\partial C_{CO_2}}{\partial z} = D_{CO_2-shell}\left(\frac{\partial^2 C_{CO_2}}{\partial r^2} + \frac{1}{r}\frac{\partial C_{CO_2}}{\partial r} + \frac{\partial^2 C_{CO_2}}{\partial z^2}\right). \tag{2.28}$$

The reaction in the system only occurs within the solvent. Therefore, the reaction rate term (r_{CO_2}) is omitted from the shell-side equation because that is the gas domain. However, r_{CO_2} is included in the tube-side equation to represent the rate of CO_2 absorption into the solvent. Although reaction kinetic models for determining r_{CO_2} are beyond the scope of this paper, it is important to note that r_A is a potential source of non-linearity. For example, if the solvent has a reaction constant that is second or third order, the equation will become nonlinear. This does not only mean that analytical solutions are impossible to get. Even more, non-linearity results in systems of stiff equations, challenging the most advanced, state-of-the-art solvers and numerical algorithms, often rendering the problems untraceable. Other research groups have incorporated chemical absorption into their 2D HFMC models introducing Monoethanolamine (MEA), Methyldiethanolamine (MDEA), and Diethanolamine (DEA), respectively [113, 114, 231].

The fluid velocities on the shell and tube sides, $v_{z,shell}$ and $v_{z,tube}$, are needed to solve Equations (2.27) and (2.28). These velocities are determined by using the 2D cylindrical Navier–Stokes and continuity equations based on Equations (2.7) and (2.8) [200, 184].

$$\rho\left(v_r\frac{\partial v_r}{\partial r} + v_z\frac{\partial v_r}{\partial z}\right) = -\frac{\partial P}{\partial r} + \mu\left(\frac{1}{r}\frac{\partial}{\partial r}\left(r\frac{\partial v_r}{\partial r}\right) - \frac{v_r}{r^2} + \frac{1}{r^2}\frac{\partial^2 v_r}{\partial z^2}\right), \tag{2.29}$$

$$\rho\left(v_r\frac{\partial v_z}{\partial r} + v_z\frac{\partial v_z}{\partial z}\right) = -\frac{\partial P}{\partial z} + \mu\left(\frac{1}{r}\frac{\partial}{\partial r}\left(r\frac{\partial v_z}{\partial r}\right) + \frac{\partial^2 v_z}{\partial z^2}\right), \tag{2.30}$$

$$0 = \frac{1}{r}\frac{\partial (r v_r)}{\partial r} + \frac{\partial v_z}{\partial z}, \tag{2.31}$$

where $v_r[\frac{m}{s}]$ is the radial velocity vector, $v_z[\frac{m}{s}]$ is the axial velocity vector, $\mu[Pa \cdot s]$ is the viscosity of the fluid, $P[Pa]$ is the fluid pressure, and $\rho[\frac{kg}{m^3}]$ is the fluid density. These equations describe steady-state, laminar, incompressible flow of Newtonian fluids. The above equations will be further reduced as translational invariance and no body forces in the r-z

plane, result in the v_r component of the velocity to be zero and the only velocity component that remains is $v_z(r)$.

Analytically solving for the velocity profile on the tube-side, the Navier–Stokes and continuity equations result in the well-established Hagen-Poiseulle velocity profile [87]:

$$v_{z,tube}(r) = 2v_{avg,tube}\left(1 - \left(\frac{r}{R_{tube}}\right)^2\right), \tag{2.32}$$

where $v_{avg,tube}[\frac{m}{s}]$ is the average velocity in the tube-side. The shell-side velocity profile is not as simple as the tube-side solution because it first requires a bundle approximation to determine the shell-side radius. In order to solve for the shell-side velocity profile, the following assumptions are made: (1) the fibers are evenly distributed in the shell space, (2) the bundle's porosity is equal to the fluid's envelope porosity, and (3) there is no friction on the shell side. Equation (2.33) defines the shell-side radius, R_{shell}, as a function of the volume fraction, φ:

$$R_{shell} = R_{membrane}\sqrt{\frac{1}{1-\varphi}}, \tag{2.33}$$

where the packing density of the membrane, φ, depends on the number of fibers in the bundle, n, and the radius of the membrane module, R_{module}. R_{module} is defined as shown in Equation (2.34).

$$1 - \varphi = \frac{nr^2}{R_{module}^2}. \tag{2.34}$$

This relationship describes the volume fraction of the void. Once the shell-side radius is calculated according to Equation (2.33), the shell-side velocity profile is determined using Happel's free surface model [105]. Happel's free surface model describes the axial velocity for flow in the annulus between concentric cylinders as a function of the radial coordinate:

$$v_z(r) = -\frac{1}{4}\mu\frac{\partial p}{\partial x}\left[(R_{tube}^2 - r^2) + 2R_{shell}^2 ln\left(\frac{r}{R_{tube}}\right)\right]. \tag{2.35}$$

Equation (2.35) is integrated with respect to r to give the volumetric flow-rate. The average velocity for a fixed pressure gradient is then obtained, by dividing by the cross-sectional area of the annulus, $\pi(R_{shell}^2 - R_{tube}^2)$:

$$v_{avg} = -\frac{1}{8(R_{shell}^2 - R_{tube}^2)}\mu\frac{\partial p}{\partial x}\left[4R_{tube}^2R_{shell}^2 - 3R_{shell}^4 - R_{tube}^4 + 4R_{shell}^4 ln\frac{R_{shell}}{R_{tube}}\right]. \tag{2.36}$$

Combining Equations (2.35) and (2.36), the analytical solution to Happel's free surface model is given by:

$$v_{z,shell}(r) = 2v_{avg}f(r), \tag{2.37}$$

where $f(r)$ is:

$$f(r) = \left[1 - \left(\frac{R_{shell}}{R_{tube}}\right)^2\right]\left[\frac{(\frac{r}{R_{tube}})^2 - (\frac{R_{shell}}{R_{tube}})^2 - 2ln(\frac{R_{shell}}{r})}{3 + (\frac{R_{shell}}{R_{tube}})^4 - 4(\frac{R_{shell}}{R_{tube}})^2 - 4ln(\frac{R_{shell}}{R_{tube}})}\right]. \tag{2.38}$$

Equations (2.26)–(2.38) describe the flow and concentration distribution for a HFMC in the radial and axial dimensions.

Common concentration boundary conditions used in 2D axisymmetric hollow fiber models are shown in Table 3, where the inlet of the flue gas is at $z = 0$ and the inlet of the solvent is at $z = L$. The physical solubility of CO_2 in the solution is defined as $m[\frac{mol}{L}]$. These boundary conditions are applied to the governing equations in the previous subsection to solve the equations analytically or numerically. For example, Equation (2.4) can be coupled with boundary conditions from Table 3 to solve for CO_2 transport.

Table 3: Concentration boundary conditions in a 2D axisymmetric HFMC with solvent flowing into the tube side at $z = L$ and flue gas flowing into the shell side at $z = 0$, as shown in Figure 8 [215].

Position	**Tube**	**Membrane**	**Shell**
z = 0	$C_{CO_2-tube} = 0$, $C_{solvent} = C_{solvent-inlet}$		
z = L			$C_{CO_2-shell} = C_{CO_2-inlet}$
r = 0	$\frac{\partial C_{tube}}{\partial r} = 0$		
r = R_{tube}	$C_{CO_2-tube} = C_{CO_2-membrane} \cdot m$, $\frac{\partial C_{solvent}}{\partial r} = 0$	$C_{CO_2-membrane} = \frac{C_{CO_2-tube}}{m}$	
r = $R_{membrane}$		$C_{CO_2-membrane} = C_{CO_2-shell}$	$C_{CO_2-shell} = C_{CO_2-membrane}$
r = R_{shell}			$\frac{\partial C_{CO_2-shell}}{\partial r} = 0$

In addition to the transport and conservation equations, 2D HFMC models should account for reaction chemistry on the permeate side. Many 2D models use water as their initial solvent to study diffusion and convection effects without the confounding effect of chemical reactions [172, 60]. Building on those results, the chemical reactions are then incorporated into models to study the chemical adsorption of common solvents, such as MDEA [217, 200, 45], DEA [231], and MEA [79, 81]. For example, Shirazian et al. used this 2D modeling approach to compare different solvents and found that MEA is a better solvent than MDEA based on CO_2 absorption [218]. Other modeling studies compare common solvents [220, 65], blended solvents [186, 93, 180], and ionic liquids [190] for optimized CO_2 separation. These reaction models can be found in the previously cited papers and incorporated into the reaction rate constant in Equation (2.27).

Many 2D carbon capture HFMC models have been used to study the impact of operating conditions on separation performance. This includes varying solvent and gas flow-rates to study how much raising the solvent:gas flow-ratio boosts CO_2 removal rates [8, 216]. Other operating conditions like pressure [80], solvent composition [115], flow direction [82],

and membrane permeability [215] have been varied to study their effect on carbon capture HFMC performance using the 2D mass balance approach. Some groups have also developed nonisothermal 2D HFMC models to study how the heat released by CO_2 absorption impacts performance. Temperature variation within a HFMC can lead to evaporation and condensation within the pores, which impacts membrane performance. Nonisothermal 2D HFMC models must incorporate the thermal energy equation (Equation (2.9)) to account for heat release and temperature variations [93, 255]. Another approach is to consider the temperature effects only on the solvent-side of the HFMC, where the CO_2 binds to the solvent and needs to undergo stripping. In this case, the temperature effect can be added in the reaction rate expression from Equation (2.27) as a function of temperature and concentration.

2.5.2 2D Modeling of Membrane Wetting

As mentioned in Section 2.4.1.2, if the transmembrane pressure surpasses the breakthrough pressure, wetting must be considered in the model. For 2D models, wetting effects can be applied to the governing 2D equations presented above. For a partially wetted system, two additional equations are introduced to account for the diffusion within a pore that is partially filled with gas and the solvent [189]. For the gas filled pore, the membrane mass transfer equation considered only diffusion.

$$0 = D_{CO_2,mg}\left(\frac{\partial^2 C_{CO_2,mg}}{\partial r^2} + \frac{1}{r}\frac{\partial C_{CO_2,mg}}{\partial r} + \frac{\partial^2 C_{CO_2,mg}}{\partial z^2}\right). \tag{2.39}$$

For the liquid filled pore, the mass transfer equation consists of diffusion and the reaction between CO_2 gas molecules and the solvent.

$$0 = D_{CO_2,ml}\left(\frac{\partial^2 C_{CO_2,ml}}{\partial r^2} + \frac{1}{r}\frac{\partial C_{CO_2,ml}}{\partial r} + \frac{\partial^2 C_{CO_2,ml}}{\partial z^2}\right) + r_{CO_2,ml}. \tag{2.40}$$

It should be noted that, with two additional equations, Equations (2.39) and (2.40), four more boundary conditions need to be included in the gas-membrane and liquid-membrane interfaces, as listed in Table 4 [45].

Table 4: Boundary conditions for the two additional mass transfer equations that account for a partially wetted membrane in a 2D axisymmetric HFMC model [156].

Position	**Gas-Membrane**	**Liquid-Membrane**
r = R_{tube}		$C_{CO_2-l-membrane} = C_{CO_2-l}$
r = $R_{membrane}$	$C_{CO_2-g-membrane} = \frac{C_{CO_2-l-membrane}}{m}$	$C_{CO_2-l-membrane} = C_{CO_2-g-membrane}m$, $\frac{\partial C_{CO_2-membrane}}{\partial r} = 0$
r = R_{shell}	$C_{CO_2-g-membrane} = C_{CO_2-shell}$	

For more information on modeling membrane wetting, refer to the following review papers [255, 175, 199, 117]. More often than not, membrane wetting is assumed to be negligible. However, several models do incorporate membrane wetting [79, 252, 158, 154, 189]. Membrane wetting is an important phenomenon that should be accounted for in more carbon capture HFMCs, particularly in situations where membrane wetting is known to occur experimentally.

2.5.3 Benefits of 2D Axisymmetric Modeling

Two-dimensional axisymmetric HFMC models have led to greater understanding of mass transport phenomena (e.g., convection, diffusion, chemical effects) within an individual fiber. These models can produce 3D visualizations by revolving the 2D results around the z-axis, as shown in Figure 9. This 2D axisymmetric approach is sufficient for most cases, where angular variations are negligible. Two-dimensional axisymmetric modeling offers many of the benefits of a 3D model (e.g., visualizing concentration variations throughout the fiber) without the added computational burden of running a full 3D model. This 2D-axisymmetric approach has also been applied to model concentration distribution within a HFMC bundle using the mass balance equations presented earlier [19]. A full 3D model that resolves the physics in the angular direction, as well, can, in principle, be more accurate than the 2D-axisymmetric approach, if there is substantial evidence that the symmetry assumption breaks down. This, for example, could be the case if turbulent flows are induced, since turbulent eddies and the dissipation of energy are inherently 3D structures and effect correspondingly. However, many researchers infer that the angular variation is not critical to the results at hand and choose the 1D or 2D-axisymmetric routes instead.

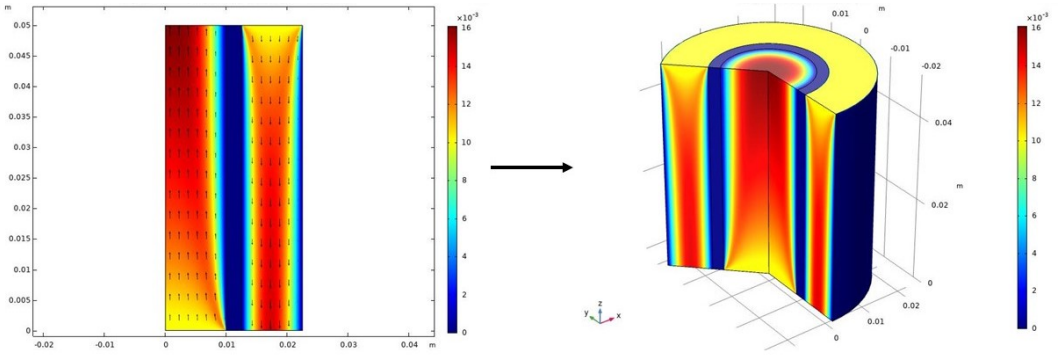

Figure 9: Velocity profiles in a counter-flow, gas-liquid HFMC. The liquid flows on the tube-side, entering at $z = L$, and the gas enters the shell-side at $z = 0$. This 2D-axisymmetric model resolves properties in a 2D cross-section (**left**), then revolves those results around the z-axis to form a 3D plot (**right**). These images were produced using COMSOL Multiphysics 5.5.®).

Although modeling in 2D requires more complex equations and computational power than 1D modeling, the results are more accurate and can better reproduce experimental data for a single fiber. Two-dimensional-axisymmetric models of HFMCs can also be used to study and predict specific phenomena that cannot be explored in 1D, such as slow kinetic reactions and axial convection and diffusion effects. In general, 2D models can offer information for a single fiber, but their results are not immediately transferable to HFMC bundles. However, 3D modeling is often necessary to obtain higher accuracy solutions and resolve more detailed 3D phenomena that cannot be captured with 2D models, e.g., turbulence, flow maldistributions, non-uniform material properties, etc.

2.6 Three-Dimensional Modeling

Three-dimensional modeling of HFMCs is the best way to describe 3D phenomena, ensure the highest degree of accuracy, and capture angular variations along with axial and radial variations. Three-dimensional models are mostly useful when studying non-uniformity throughout a bundle (e.g., non-uniform flow distribution near ports and in the case symmetry does not hold). Figure 10 shows these three dimensions (axial, radial, tangential) for a single hollow fiber. This section discusses 3D modeling of HFMCs at a high level because the governing equations and set-up for modeling a 3D HFMC fiber are similar to those presented in the 2D section but with additional angular equations and terms. The governing equations for 3D models are also often built into software packages, so they do not need to be coded from scratch. Multiphysics software packages (e.g., ANSYS, OpenFOAM®, and COMSOL Multiphysics ®) are often preferred to model these types of systems.

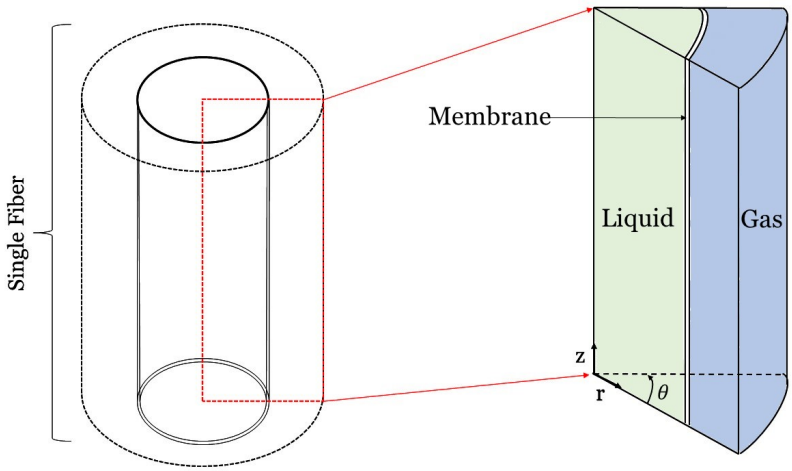

Figure 10: Graphic of the three-dimensional modeling framework for a gas-liquid HFMC. Axial (z), radial (r), and tangential (θ) variations are all resolved. In this graphic, solvent flows on the tube-side while flue gas flows on the shell-side.

One of the main advantages of 3D modeling for HFMCs is that it can be used to study transport variations throughout an entire bundle, not just in a single fiber. Whereas 1D and 2D HFMC models are limited to a single fiber, 3D models can be developed for an entire HFMC bundle. These 3D bundle models can provide information about flow distribution throughout the bundle and be used to study the impacts of fiber non-uniformity. One team used this bundle approach in COMSOL Muliphysics® to calculate the overall MTC to describe the fluid flow for an incompressible fluid [37]. Another research group investigated the effects of temperature variation on chemical reactions in a 3D HFMC bundle by directly coding the 3D energy conservation equations and RIS for heat transfer resistances [38]. There have also been studies that focus on radial variations in a bundle exposed to steady-state turbulent flow to determine the optimal fiber arrangement [225]. Although 3D bundle modeling is the most accurate and detailed approach, it is also the most computationally expensive approach mentioned so far.

One way to simplify the 3D HFMC bundle model (and reduce computational burden) is to treat the bundle as a homogeneous, porous media [253]. Darcy's Law (Equation (2.24)), derived from a simplified Navier–Stokes equation, can be applied to the system to describe the pressure drop and fluid flow within a porous medium. This approach is extensively researched for packed bed models [207, 176, 241, 76], and the same principles apply to flow through a bundle of fibers. The mass balances and MTCs in these porous media models are calculated using the approaches discussed in Sections 2.4 and 2.5. This approach has also been successfully used in other research fields to model reverse-osmosis for water filtration [150, 222] and blood oxygenation devices [84, 221]. These models would provide more insight

into the flow and concentration distributions within HFMC bundles, so future research is recommended in this area.

Three-dimensional models of HFMCs have improved significantly in the past decade due to advances in computational capabilities. However, there is still significant room for improvement in reducing computational cost of these models while maintaining accuracy. Although many 1D and 2D HFMC models have been developed for PCC, 3D HFMC models are relatively new and therefore require further development. The next section compares the 1D, 2D, and 3D modeling approaches for HFMCs in PCC with an emphasis on the assumptions made by each of these models.

2.7 Comparison of 1D, 2D, and 3D Modeling Approaches

Each of the three modeling approaches described in the previous sections has unique merits and drawbacks. This section will compare these three modeling approaches with an emphasis on the different assumptions made by each type. Table 5 compares state-of-the-art 1D, 2D, and 3D carbon capture HFMC models based on their controlling assumptions, which are listed below the table. Table 5 provides a foundation for researchers seeking to develop the best HFMC carbon capture model to meet their particular needs.

One-dimensional models are assumed to have perfect flow distribution, fiber alignment, uniform membrane properties, etc., 1D models assume that reactions and mass transfer occur within a very thin reaction "film," which effectively reduces the axial dimension and leaves only variation in the radial direction [246]. One-dimensional modeling is considered sufficient for many applications, particularly those that involve scaling-up to larger system sizes. One-dimensional modeling is especially well-suited for larger systems because it is computationally expensive to resolve 2D or 3D effects in large HFMC systems. Many researchers prefer 1D models to 2D models for the PCC HFMC application, because 1D models are significantly faster and provide sufficiently accurate results [246]. Overall, 1D models can predict the results from previous experiments and simulations in 2D and 3D [245]. However, 1D modeling is only applicable if the MTCs are known or defined experimentally. If the MTCs are not known prior to the analysis, 2D or 3D modeling techniques may be necessary to determine the overall MTC because they are easier and cheaper than experimentation. Obtaining MTCs from experimental data is not an easy task, since one needs to accurately track the interfacial area between liquid and gas. This requirement in its turn demands state-of-the-art imaging techniques, without which the only way to predict MTCs, necessary for any scale-up attempt or actual system-design effort, is futile. Two-dimensional-axisymmetric and 3D models of a single fiber can give access to the fiber's MTC, while 3D models of the whole bundle can generate the bundle's average MTC.

Most HFMC modeling work thus far has focused on 1D because it is the simplest approach

and provides sufficient accuracy for many applications. For example, one comparison between 1D and 3D HFMC models found only a 2 percent deviation in mass balance results [98]. This suggests that unless the researcher is looking for more detailed information internal to the fiber or bundle, a 1D model should be sufficiently accurate. Another downside of 1D models, besides the fact that it requires pre-determined MTC, is that it is unable to resolve 2D or 3D effects, such as fluid swirling or CO_2 concentration gradients. It is possible to overcome some 1D limitations by enhancing 1D models (e.g., by adding wetting effects). However, some membrane systems are best modeled in 2D or 3D to capture radial and/or angular effects. Table 5 provides common assumptions used for 1D HFMC models in reference to the list (listed after Table 5) in the beginning of this section. The prevalent assumptions among 1D models are assumptions 3–6 and 8–9, where the physics focuses on the membrane interface.

As seen in Table 5, assumptions 10–15 are common assumptions made within 2D models. For example, most 2D species calculations rely on Happel's free surface model offering an analytical calculation of the shell-side velocity profile, as presented in Section 2.5.1. Other assumptions include zero inlet CO_2 concentration on the solvent side. These assumptions allow the modeler to successfully solve the fundamental laws and governing equations, simplifying the simulation of a HFMC. Zaidiza et. al. provide a more thorough comparison of the 1D and 2D modeling approaches for PCC HFMCs [244]. Another approach that combines the advantages of the two modeling approaches is hybrid 1D-2D modeling. For example, Chabanon et al. [50] uses a 1D model for the gas-side and a 2D model for the liquid-side. There is more work in the literature that covers hybrid 1D-3D modeling, such as Bao et al. [23], that studies the correlations of mass transfer coefficients between regularly and randomly packed bundles for gas-gas HFMCs.

Table 5 also provides common assumptions used for 3D models, including Happel's free surface model and zero initial concentration on the solvent side. Although 3D models of HFMCs are less common than 1D and 2D models, they are growing in popularity as advanced algorithms, hardware and software are facilitating 3D modeling simulations. Three-dimensional models of HFMCs bundles, enable researchers to go beyond modeling a single hollow fiber and explore non-uniform effects. Three-dimensional bundle models are recommended for modelers looking to transfer their work into a process or system level simulation for this important technology of CC, assuming they can be computationally handled. Challenges however still remain due to the numerical cost of the calculations [44].

Modeling the bundle as a porous medium, though not common in the carbon capture field, there are other of scientific applications we could get inspiration from. Mazaheri et al. [169] offer a comparison between fiber modeling and porous media for a blood oxygenator device, finding that the velocity distributions are different and the porous media approach may lead to errors when calculating the transport properties. Three-dimensional bundle models can provide useful information about end effects and the impact of manifolds on flow distribution. However, modelers must prioritize the outcome of the project and decide if simplifying a 3D bundle using the porous media approach is right for them, or if they should

simplify their model to 1D or 2D. Overall, 3D models are powerful tools for determining how conditions vary throughout a 3D bundle, not just along the length of an average fiber.

Table 5: State-of-the-art HFMC models for PCC organized by dimensionality. Modeling assumptions (listed in the text) are checked for each model to enable comparison.

Dimension	**References**	**Assumptions**															
		1	2	3	4	5	6	7	8	9	10	11	12	13	14	15	16
1D	Boributh et al. [33]	✓	✓					✓								✓	✓
	Zaidiza et al. [243]	✓	✓	✓	✓	✓										✓	✓
	Khaisri et al. [130]	✓	✓				✓									✓	✓
	Boributh et al. [32]	✓	✓			✓		✓								✓	✓
	Boributh et al. [35]	✓	✓			✓		✓								✓	✓
	Rode et al. [203]	✓	✓						✓							✓	✓
	Zaidiza et al. [244]	✓	✓		✓	✓										✓	✓
	Villeneuve et al. [228]	✓	✓	✓	✓	✓			✓							✓	✓
	Li et al. [147]	✓	✓		✓				✓							✓	✓
	Chu et al. [51]	✓	✓			✓										✓	✓
	Haddadi et al. [98]	✓	✓			✓				✓		✓				✓	✓
	Cui et al. [56]	✓	✓				✓		✓		✓	✓			✓	✓	✓
	Saeed et al. [206]	✓	✓		✓		✓									✓	✓
2D	Al et al. [8]	✓	✓				✓			✓	✓	✓	✓	✓	✓	✓	✓
	Shirazian et al. [216]	✓	✓				✓			✓	✓	✓	✓	✓	✓	✓	✓
	Rezakazemi et al. [200]	✓	✓				✓			✓	✓	✓	✓	✓	✓	✓	✓
	Shirazian et al. [217]	✓	✓				✓			✓	✓	✓	✓	✓	✓	✓	✓
	Shirazian et al. [215]	✓	✓				✓			✓	✓	✓	✓	✓	✓	✓	✓
	Hosseinzadeh et al. [115]	✓	✓				✓			✓	✓	✓	✓	✓	✓	✓	✓
	Faiz et al. [80]	✓	✓				✓				✓		✓	✓	✓	✓	✓
	Ghasem et al. [93]	✓	✓				✓					✓	✓		✓	✓	✓
	Goyal et al. [95]	✓	✓							✓	✓					✓	✓
	Li et al. [149]	✓	✓	✓						✓		✓				✓	✓
	Cao et al. [45]	✓	✓							✓	✓	✓				✓	✓
	Shirazian et al. [218]	✓	✓							✓	✓	✓			✓	✓	✓
	Nakhjiri et al. [180]	✓	✓							✓	✓	✓			✓	✓	✓
	Qazi et al. [189]	✓	✓							✓	✓	✓				✓	✓
	Abdolahi et al. [4]	✓	✓							✓	✓	✓				✓	✓
	Ghasem et al. [92]	✓	✓							✓	✓	✓			✓	✓	✓
	Qazi et al. [190]	✓	✓							✓	✓	✓			✓	✓	✓
3D	Boucif et al. [37]	✓	✓				✓			✓	✓		✓		✓	✓	✓
	Boucif et al. [38]	✓	✓	✓	✓		✓						✓			✓	✓
	Usta et al. [225]	✓	✓				✓									✓	✓
	Cai et al. [44]	✓	✓				✓				✓					✓	✓
	Pozzobon et al. [188]	✓	✓				✓				✓					✓	✓

List of Assumptions in Table 5:

1. Steady-state, laminar, Newtonian, incompressible fluid, and plug flow with fully-developed velocity profiles.
2. Ideal gas law (assumes the gas particles are (1) in continuous, rapid motion, (2) are so small that their volume is negligible, (3) do not interact, and (4) temperature is proportional to the average kinetic energy); and Henry's law (assumes constant temperature and that the vapor phase behaves as an ideal gas).
3. Fick's law of diffusion (assumes constant diffusion coefficient) and thermal conductance through membrane, with adiabatic behavior.
4. Rate-controlled reversible reaction.
5. Heat and mass transfer are equal at the interface (condensation from the temperature difference occurs at the liquid-membrane interface).
6. Uniform membrane properties (constant tortuosity and distribution of membrane pore size, wall thickness, non-wetting).
7. Mass transfer between gas-liquid phases is a result of film diffusion.
8. Curvature effect of the membrane surface on mass transfer is negligible.
9. Happel's free surface model (assumes the bundle's porosity is equal to the fluid's envelope porosity and assumes no friction on the shell-side).
10. Initial zero CO_2 concentration on the solvent side.
11. Zero mass transfer at the two fiber ends.
12. Constant volumetric flow rate.
13. Large mass transfer rate between gas and liquid.
14. Non-wetted operation in which the gas mixture fills the membrane pores.
15. Ideal feed gas (fouling/pollution not accounted for).
16. Fibers are rigid walls (no degradation study is needed).

2.8 HFMC Modeling Road Map

This section summarizes the exposed ideas presented in Sections 2.4–2.6 to guide modelers' decision towards the type of modeling approach and dimensionality they should choose for their research goals. A road map, Figure 11, illustrates possible directions the simulation could take.

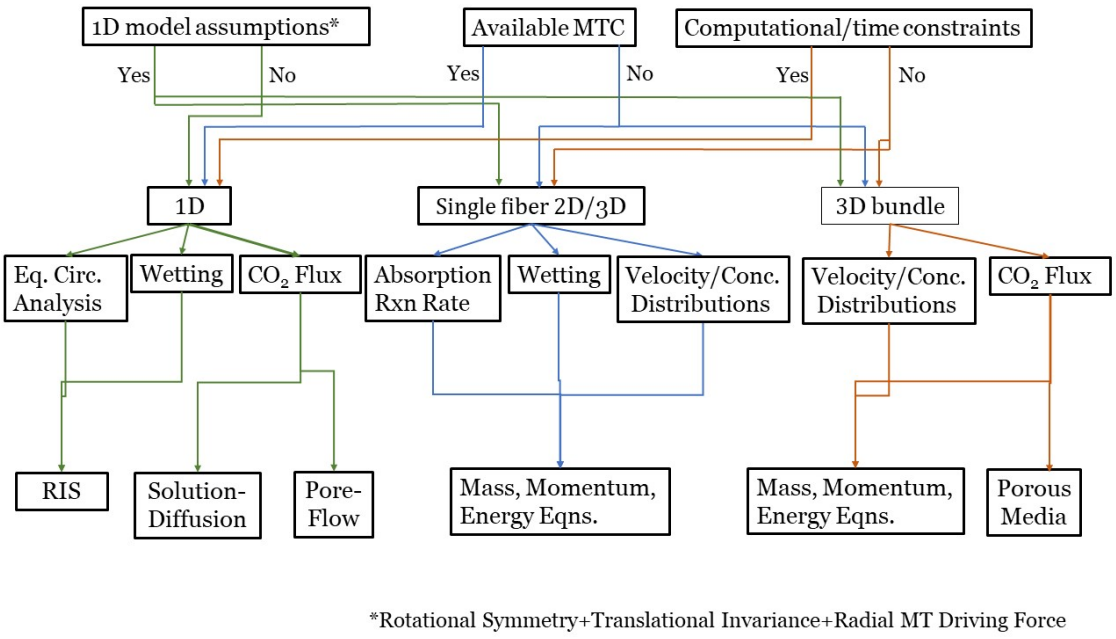

Figure 11: The road map is separated based on three defining questions: (1) Is the modeler taking into account 1D model assumptions? (2) Does the modeler have access to the mass transfer coefficient values? (3) Does the modeler have computational or time constraints? Depending on those qualifications, 1D, 2D, or 3D models can be chosen. Each modeling approach previously described for 1D, 2D, and 3D models provide specific end goal phenomena to be described. These goals for 1D models shown here are solving for the equivalent circuit analysis (eq. circ. analysis), the wetting effects, and CO_2 flux removal. Depending on the overall goal, the RIS, solution-diffusion or pore flow model could be used. For 2D axisymmetric/3D single fiber models, the end goal could consist of observing the absorption reaction rate, the wetting effects and overall velocity and CO_2 concentration profiles. The mass, momentum and energy equations could be coupled to recover the velocity and concentration profiles in all three domains (tube, membrane, and shell domains). Finally, 3D models observe the overall bundle of the HFMC. If the final goal is to determine detailed fluid and concentration distributions within the bundle, the mass, momentum and energy equations should be used for more accurate results. However, if the overall goal is to observe the CO_2 flux rate, the porous media approach should work just as well.

2.9 Applications and Challenges

In the following paragraphs, we wish to highlight the application aspect of several groups' HFMC post-carbon capture 1D, 2D, and 3D models. This section will also cover software implementation issues to model HFMCs and challenges associated with these simulations and models.

2.9.1 Applications of 1D Models

As previously stated, the RIS model can be used to determine the overall MTC needed to calculate the flux across the HFMC. The overall MTC can be modified to include chemical and wetting effects. For example, Boributh et al. [33] contributed to the field by creating a mathematical model to predict the physical absorption of CO_2 and the effects of membrane wetting on pore size, membrane geometry (thickness and fiber length) and fluid flow. The results were validated with the experimental data reported by Achariyawut et al. [16]. Building on their work, this group incorporated the chemical effects of the system to predict the absorption performance of CO_2 from a gas mixture containing methane (CH_4). Using MEA as the absorbent, the group successfully predicted the performance of a PVDF HFMC by incorporating membrane wetting and the enhancement factor, E, to calculate the overall MTC and model the rate of absorption [35]. The RIS model was also used to predict CO_2 separation from a CO_2-N_2 gaseous mixture using a DEA solution and a PP HFMC [95]. This group also incorporated partial membrane wetting into their model and observed a rapid decline in module performance due to the physical geometric changes, such as enlarged pore-size and elevated surface roughness. It was noted the pore-size enlarged quicker using DEA rather than MEA.

The solution-diffusion model is used to model dense membranes, such as dense polymer-supported ionic liquid membranes used to separate CO_2-N_2 and CO_2-CH_4 mixtures [11]. Models predicting the performance of HFMCs using the solution-diffusion approach have successfully investigated process intensification (for scale-up purposes) and solvent leak reduction when considering a volatile solvent, such as aqueous ammonia [228]. This work has been validated against experimental work in the laboratory scale [227]. Chabanon et al. [50] point out a challenge comparing the experimental results against this well-established model: it is unrealistic to compare the results without adjusting any parameter. Therefore, the membrane MTC is adjusted in the model for validation against the experimental results. The solution-diffusion model approach has also been used to model separation CO_2 from multi-component flue gas containing N_2, O_2, H_2O, and CO_2 to find optimal regions of flue gas pressures and membrane area [131].

2.9.2 Applications of 2D Models

Many research groups have applied 2D-axisymmetric HFMC models to post-combustion carbon capture. Many different solvents, operating conditions, flue gas mixtures, and wetting effects have been modeled in this framework. Many of these models have successfully predicted experimental results for PCC applications.

For example, Shirazian et al. [216] developed a 2D-axisymmetric model to study CO_2 removal from 20/80 CO_2-N_2 mixture for general gas separation (coal, natural gas and flue gas). They initially only studied physical absorption to isolate the effects of varying temperature and fluid and gas flow rates. They then studied the impact of chemical absorption by incorporating MDEA [217], diethanolamine [215], DEA [198], MEA, 2-amino-2-methyl-1-propanol (AMP), and potassium carbonate (K_2CO_3) [220] into their models. Their results show that MEA achieved the highest CO_2 removal rate. Another 2D modeling group studied the effect of mixing an ionic liquid into pure water to act as a physical absorbent alongside MEA as a chemical absorbent [184]. Their results showed that including an ionic liquid increases CO_2 absorption in both physical and chemical absorbents.

Other groups have modeled wetting effects in their 2D axisymmetrical models of HFMCs. Non-wetted, partially wetted, and fully wetted models were compared by one team to observe the effect membrane wetting has on separation efficiency, CO_2 flux and overall MTC [189]. They successfully modeled the removal of CO_2 from a 15/85 CO_2-N_2 gas mixture and observed with increasing membrane wetting, there was an increase of mass transfer resistance and therefore lower separation efficiency and CO_2 flux. Abdolahi et al. [4] also modeled a 2D-axisymmetric HFMC with partial membrane wetting and found that even a 10% wetting of the membrane reduces the efficiency of the CO_2 removal process by more than 47%. Their results were compared to experimental data.

Ghasem et al. [92] developed another 2D-axisymmetric HFMC model for the simultaneous absorption/stripping of CO_2 with potassium glycinate. This group was able to use two gas-liquid HFMC in parallel and model both the absorption and stripping process. They were able to model the stripping portion by defining the reaction rate in the solvent-side as a function of temperature and concentration, observing that, as the stripping temperature of rich solvent increases, the stripping efficiency increases. Their work was validated against experimental data.

2.9.3 Applications of 3D Models

Very few 3D models currently exist for HFMCs in PCC applications. Thanks to recent advances in computational ability, this is an emerging research area with room for future development. One research group has developed a 3D bundle model to study the flow passing through different fiber array arrangements for CO_2 removal from CH_4 [225]. Three-dimensional modeling is needed for this group's work to study the radial cross-flow distribution for inline

and staggered fibers in the bundle, as well as momentum mixing. They demonstrated that a bundle with staggered arrangement outperforms the bundle with the inline arrangement after evaluating the CO_2 flux rate across the membrane surface. The porous media approach, while scarce in the PCC field, has recently been applied by Pozzobon et al. [188]. This group created a computational fluid dynamic model that describes the mass transfer at the fiber scale in addition to the fluid flow in the bundle. The purpose of this work is to illustrate how to apply the porous media model to obtain the mass transfer resistance values numerically, rather than using a correlation, like for 1D models, or experimental values, like for 2D models. Their results replicated Whitaker [235] and Fougerit et al. [85, 86] correlation's in addition to experimental runs.

2.9.4 Software Implementations

One of the key challenges with developing HFMC models for PCC is determining whether a 1D, 2D, or 3D model is the best option. The decision to model a HFMC in 1D, 2D, or 3D depends not only on governing assumptions and desired results but also on practical computing constraints. Carbon capture HFMC models require a complex combination of equations that may be linear, non-linear, possibly coupled, ordinary-differential or partial-differential. Therefore, sophisticated modeling software (e.g., MATLAB ®, COMSOL Multiphysics®, ANSYS (CFX and Fluent), ASPEN Custom Modeler, OpenFOAM) are often used. Software selection depends on the complexity of the model and what features need to be studied. For example, MATLAB® is typically sufficient for 1D modeling, but finite-element software products (e.g., ANSYS, COMSOL Multiphysics ®) are often preferred for 2D or 3D modeling as they do not require coding. ANSYS and COMSOL both have user-defined partial differential equations (PDEs) and pre-defined PDEs modules for a wide range of applications, putting less burden on the user during initial model set-up. Although ANSYS and COMSOL Multiphysics ® are used for 1D models, as well, their true advantage is revealed in the 2D and 3D simulations where complexity increases dramatically [222]. MATLAB ® is a popular platform for 1D and sometimes 2D HFMC models [251, 25]. Some 1D models can even be set up in Excel workbooks or similar platforms. Researchers may opt for 1D models based on cost constraints and software availability. ASPEN Custom Modeler incorporates HFMC models as a user defined unit operation to study scale-up modeling [7].

Mesh refinement is required in narrower areas of the geometry demanding higher resolution to guide the computations. For example, the membrane domain in the 2D single fiber analysis will need finer mesh to fully capture the physics that occur within a thinner domain. This is especially true when the model needs to capture membrane wetting effects. Another example where mesh refinement is needed is for a 3D model of the individual fibers to capture the physics within the smaller gaps between the fibers [98]. However, mesh refinement will cause the simulation to become more computationally expensive. Therefore, the modeler needs to determine the most demanding physics of the system using non-dimensionalization and

the knowledge of boundary layers to assess the needed mesh sizes. Mesh independence is another important factor of the meshing methodology, used to determine accurate finite element/volume solutions. It is highly recommended for 2D and 3D simulations of HFMCs. The mesh independence study chosen will provide a less burdensome model that solves the physics to the desired level of accuracy. Once the simulation produces minimal changes between the mesh element or volume solutions for different levels of mesh refinement, the less burdensome mesh will be chosen and the mesh independence study will be complete. In general, models should use the least number of mesh elements necessary to converge on a satisfyingly accurate solution. Examples of authors that have published their mesh study for HFMCs can be found here [225, 4].

One of the main downsides of 3D HFMC modeling is that it is computationally expensive, which may prevent some researchers from pursuing this route. However, sophisticated multi-physics software packages (e.g., ANSYS, COMSOL Multiphysics ®) facilitate 3D modeling of HFMCs. These user-friendly software packages also have built-in short-cuts for reducing computational time (e.g., reducing mesh size, simulating a symmetric portion of the full geometry). Three-dimensional simulations of HFMCs can also often be run in parallel on different machines in a computer cluster to minimize computational time. Recent advances in software and computers have made it possible to perform 3D simulations of HFMCs faster and cheaper. Future advancements in computation will enable more researchers to pursue complex 3D models for carbon capture HFMCs.

2.9.5 Modeling Challenges

One shortcoming of HFMC models for PCC is that no existing models are currently capturing the physical and chemical degradation of the membrane over time. Degradation rates are typically characterized experimentally, but these experiments are expensive and lengthy. Transient models that can predict long-term degradation of HFMCs exposed to flue gas would be immensely helpful. Although it would be theoretically and computationally challenging to develop a detailed mechanistic model for long-term degradation, simple models could be developed to extrapolate short-term experimental degradation data to longer time scales. This kind of model could save time and money on pilot testing and enable quicker scale-up of HFMC technology.

Another challenge that HFMC models face is that they struggle to capture non-idealities in bundle design. Because most HFMC models assume a uniform distribution of fibers with identical stream conditions, they cannot predict the effects of flow maldistribution, non-uniform fibers, or uneven fiber distribution within a bundle. For example, Happel's free surface model (which is used in 2D models to determine the shell-side velocity) assumes that all the fibers are evenly spaced in a triangular or staggered array. The actual shell-side velocity could vary substantially from this model's predictions, if fibers are distributed unevenly. Similarly, most HFMC models assume no friction from the walls of the fiber.

Three-dimensional HFMC models can address many of these short-comings by incorporating wall effects and bundle non-uniformities.

Two other assumptions included in most models that could be considered as rendering the models prone to wrongful representation of the physics are: a) constant permeate and retentate mixture properties, i.e., not function of the local concentration, and b) continuity equation described by incompressible flow, i.e., $\nabla \cdot \boldsymbol{u} = 0$. The latter assumption is posed to apply the continuity equation to solve for the velocity in the tube-side. Both these hypotheses generate concern, since the gaseous system is a multi-component flue gas mixture. Therefore, the density will change as CO_2 is separated. This is an issue that needs to be addressed with most of the relevant reported research and remedied in future modeling undertakings to produce more reliable results.

2.10 Scale-up Modeling from Lab Scale to Commercial Scale

The previous sections have focused exclusively on modeling a single fiber or bundle of fibers in a carbon capture HFMC absorber. However, modeling efforts need to extend beyond small-scale HFMC absorbers in order to scale up work from the lab to the pilot and commercial scales. This would help minimize the transitional time between bench and large scale HFMCs absorbers and minimize the risk and costs for the plant facilities. Scale-up and commercialization efforts tend to increasingly rely on modeling, as necessary stepping stone to design and optimize scale-up for PCC. A characteristic example is the Department of Energy's Carbon Capture Simulation for Industry Impact ($CCSI^2$) program of the National Energy Technology Laboratory (NETL)-Department of Energy. $CCSI^2$ is a computational tool-set of different scale and scope models, ranging from CFD and process modeling to optimization, uncertainty quantification and sequential design of experiments, targeted to de-risk and facilitate up-scaling PCC technology in the United States. Apart from the standard CFD and process models, new capabilities pertaining to Artificial Intelligence are added to the researchers' portfolio. For example, modeling efforts involving systematic design of experiments (referred to as sequential design of experiments) can guide test campaigns and enable teams to get experimental results efficiently. Techno-economic models of carbon capture HFMC systems can also aid with the scale-up process by predicting and optimizing for parameters like size and cost. Some HFMC scale-up models focus exclusively on optimizing the HFMC absorber design (e.g., to minimize size or cost) at a larger scale. Other HFMC scale-up models include the entire carbon capture system or even the whole power plant system. Aspen Custom Modeler and similar software packages are helpful tools for developing and optimizing process models for complex systems like this.

Figure 12 shows a conventional CO_2 capture process using HFMC modules as the absorber. This CO_2 capture system also requires a CO_2 stripper, coolers, pumps, and a reboiler.

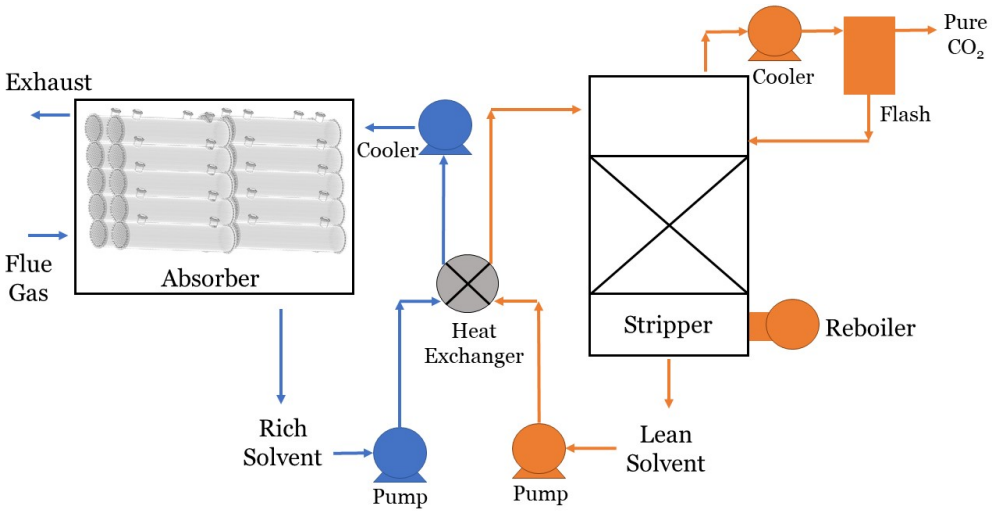

Figure 12: Graphic of a conventional CO_2 capture process using HFMC modules in the absorber. The blue represents the absorption process, and the orange represents the stripped portion of the system.

Although there have been several pilot tests of carbon capture HFMCs [229, 212, 211], modeling efforts for gas-liquid HFMC pilot-scale or commercial-scale modeling are scarce [255]. The following discussion therefore focuses on gas-gas HFMC carbon capture systems, which closely resemble gas-liquid carbon capture HFMC systems. A common metric used to quantify CO_2 capture cost in membrane systems is the gas processing cost. The gas processing cost depends on various parameters (e.g., membrane geometry, operating conditions), so a final product purity must be specified in order to achieve a desired gas processing cost goal [7]. The overall calculation of gas processing cost depends on the capital related costs for installation and fabrication of equipment, the variable operating and maintenance costs, and the cost of hydrocarbons lost in the permeate stream [168]. In most instances, researchers also consider a payout period of 5 years to calculate the total capital cost. Researchers often use gas processing cost to study the impact of non-ideal cases that could occur in industrial applications. For example, variable permeances due to temperature and pressure dependence greatly affect the membrane permeability [6] , and membrane fouling increases the energy requirement [28]. In addition, up to 20% of the base plant costs should be allocated to cover unforeseen events, such as complications with the recycle stream [102, 101]. The same gas processing cost methodology is used across different projects to study the various parameters that affect gas processing cost, such as pressure ratios [116] and flow pattern distributions [153].

Aside from gas processing cost analyses for gas-gas HFM modeling, many researchers shift their modeling efforts from modeling single fibers to modeling pilot-scale membrane

systems when it is time to scale up their technology. ASPEN HYSYS® is a commercial process simulation program that can be used for this task, particularly if the team wishes to integrate their membrane model into a process model for an entire power plant. Modeling in this framework elucidates many bulk effects, such as non-uniform distribution of flow among fibers, that have been used for HFMCs but are difficult to capture in smaller-scale HFMC models [49]. Proprietary platforms, like the Integrated Environmental Control Model (IECM) from Carnegie Mellon University, estimate system and performance costs of power plants with gas-gas membrane carbon capture [250]. In most of these process models, researchers consider a two-stage membrane process: the first membrane operates at an optimal pressure ratio [66], and the second membrane focuses on selectivity [205]. Platforms, like IECM, could likely be used to model gas-liquid HFMCs, as well. This would enable researchers to determine the optimal process design for gas-liquid carbon capture HFMC systems.

System modeling is a crucial step for carbon capture HFMC technology development. Particular emphasis should be placed on characterizing the CO_2 stripping process, which is often overlooked in carbon capture HFMC modeling studies. The most expensive operating cost in a solvent-based CO_2 capture system is typically the cost of desorbing CO_2 from the solvent [238]. Therefore, more effort is needed to model desorption and optimize solvent selection in HFMC systems. These models could complement experimental efforts to minimize costs of HFMC carbon capture systems and make them more competitive with traditional solvent carbon capture systems.

2.11 Conclusions and Recommended Future Work

HFMCs are one of the leading technologies for post-combustion carbon capture. Modeling efforts are needed both to characterize these HFMC technologies and scale them up for commercial adoption. This review paper presented and compared 1D, 2D, and 3D modeling approaches for carbon capture HFMCs. The goal of this review is to help HFMC researchers identify which modeling methods are most applicable to their projects. One-dimensional models are the most efficient and tend to produce accurate results given the correct assumptions (such as treating the interfaces of each domain as "films" for the RIS model). Modeling in 2D has also become a popular option in carbon capture HFMC research, and it provides higher accuracy and more information than 1D models can provide. One-dimensional and 2D models for membrane wetting were also discussed.

Three-dimensional models of carbon capture HFMCs are scarce because they are more computationally expensive than 1D or 2D models. However, they are qualitatively different in the nature of information they can reveal. Three-dimensional models are recommended for researchers that need to study variations within the HFMC bundle, which cannot be encompassed by 1D or 2D single fiber models. Similarly, if what is of interest is understanding

of the underlying mechanisms of mass, energy, and momentum transfer and their interplay, then one has to resort to 3D bundle models or, at the very least, to 2D and 3D single fiber models with some effort to account for non-idealities from up-scaling to the bundle level. For those interested in capturing bundle variations with reduced computational cost, we recommend considering the porous media modeling approach. Further research is also needed to accurately model membrane fouling. These efforts will help researchers better predict HFMC lifespan and minimize degradation.

The transition from bench-scale to pilot-scale modeling was also discussed, and it is an area where further research is needed in order to make HFMCs competitive with other CO_2 separation technologies [133]. While scale-up models exist for gas-gas HFMCs, more scale-up models are needed, specifically for gas-liquid carbon capture HFMCs. Future research on both scale-up modeling and 3D bundle modeling will accelerate the progress and commercialization of gas-liquid carbon capture HFMCs.

3.0 "Demonstration of Direct Ocean Carbon Capture Using Hollow Fiber Membrane Contactors"

The focus of membrane carbon capture to date has been primarily on point source captures, such as power plants and industrial capture. However, membrane technology can also play a role in negative emissions technology, such as direct air capture and direct ocean capture. Direct ocean capture has a few potential advantages over direct air capture, such as avoiding land use and coupling with offshore wind and offshore storage. The use and feasibility of hollow fiber membrane contactors (HFMCs) for direct ocean carbon capture with benign aqueous basic carbon dioxide solvents is assessed here through a multifaceted approach. A 1D HFMC model incorporates fluid dynamics and the chemical kinetics of both ocean water and aqueous sodium hydroxide solvent in order to simulate CO_2 flux behavior in two flow configurations. Lab scale experiments of this system then guide a model refinement and validation process until experimental behaviors are predicted through computation. A preliminary techno-economic assessment then uses computational and experimental results to estimate the carbon capture cost when the system is scaled to remove 0.98 Mtonnes CO_2/year. Computational results suggest that higher seawater flow rates and temperatures relative to the sodium hydroxide solvent improve CO_2 flux. The techno-economic assessment suggests that HFMCs may only be cost-competitive if seawater pH is decreased at the membrane interface, thereby increasing the local concentration of dissolved carbon dioxide. These findings indicate that local pH swing on the seawater side will be necessary to feasibly remove carbon dioxide from seawater using HFMCs.

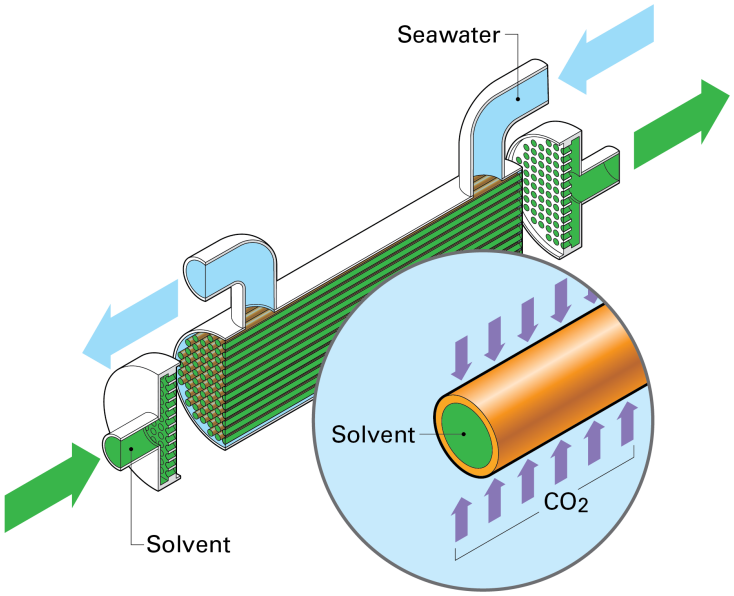

Figure 13: Using hollow fiber membrane contactors to separate CO_2 from seawater. This is facilitated by flowing a solvent through the tube side of the membrane, and the seawater through the shell side in a counter-current direction.

3.1 Nomenclature

Subscripts

s	solvent
m	membrane
oc	ocean
ov	overall
CO_2	CO_2 in a domain
shell	shell side
mem	membrane side
lumen	lumen (or tube) side
h	hydraulic
i	inner
o	outer
eff	effective
i	component or species

Variables

k	resistance
D	diffusion coefficient
d	diameter
ε	porosity
τ	tortuosity
δ	thickness
L	length
C	concentration
J	flux
δP	pressure drop
T	temperature
N	number of fibers

Acronyms

PCA	Paris Climate Agreement
DAC	Direct Air Capture
DOC	Direct Ocean Capture
HFMC	HFM contactor
RIS	Resistance in series
TEA	Techno-economic analysis
EAOC	Equivalent Annual Operating Costs

3.2 Introduction

The 2016 Paris Climate Agreement (PCA) set an international standard for global temperature rise to be no higher than 1.5 °C above pre-industrial temperatures [77]. This temperature threshold suggests that atmospheric concentrations of carbon dioxide (CO_2) must not exceed 450 ppm to mitigate the risks outlined in the PCA [29, 106]. However, global CO_2 emissions have continued to rise, causing atmospheric CO_2 to reach 416 ppm in 2019 [124, 125]. Negative emissions technologies will need to remove more than 10 gigatonnes of CO_2 each year from the environment by 2050 in order to remain within the 1.5 °C temperature threshold [29].

Direct air capture (DAC) is one of the key negative emissions technology categories proposed to mitigate climate change. DAC systems scrub CO_2 from the atmosphere, typically using adsorptive solids or caustic solutions [128, 74, 148, 152]. DAC technologies, however, are limited by low atmospheric concentrations of CO_2, leading to high capture costs of ∼$500-$600/tonne CO_2 [140, 17]. One alternative to DAC that has received less attention is direct ocean capture (DOC). Oceans store ∼27% of atmospheric CO_2 [141], and maintain equilibrium with the CO_2 in the surrounding atmosphere [89]. Although CO_2 partial pressure in seawater is low, like in the air above it, seawater has high concentrations of bound CO_2 (in the forms of bicarbonate and carbonate ions) that can potentially be accessed during DOC [249]. Additionally, seawater is ∼1,000 times denser than air, which could result in a smaller system size. DOC could also potentially be performed offshore (e.g. on an abandoned offshore oil platform) to avoid using land space, and be co-located with offshore wind and/or offshore storage. Finally, direct ocean capture could potentially reverse ocean acidification in high-risk niche areas, such as coral reefs or shellfisheries. All of these advantages could make DOC a promising alternative or complement to DAC systems, which require lots of energy, take up large amounts of land, and often require CO_2 transportation to storage sites [13].

Existing state-of-the-art systems for DOC require an energy-intensive salt-splitting process to separate seawater into basic and acidic streams before stripping CO_2 from the acidic stream [237, 73]. The main advantage of this approach is that gaseous CO_2 is more abundant at low pH levels, so higher CO_2 fluxes are possible once seawater has been acidified [248]. The main drawback of this salt-splitting approach, however, is that the electrodialysis membrane required to split the seawater into acidic and basic streams is expensive and requires a lot of energy [107]. Although these DOC methods make sense for niche markets (e.g. jet fuel production for naval ships at sea [237]), they are currently too expensive to compete with DAC [197].

Passive membrane contactors have yet to be employed for DOC but offer several potential advantages over salt-splitting methods: reduced energy consumption, low cost, and ease of scalability. Hollow fiber membrane contactors (HFMCs) are a passive membrane technology that has been optimized for post-combustion carbon capture and may be suitable for the

DOC application [48, 255]. HFMCs consist of many narrow, hollow tubes (fibers), packed tightly into a cylindrical jacket. The membrane material in HFMCs is typically a flexible polymer (e.g. polypropylene) that is gas-permeable but not liquid- or ion-permeable at ideal conditions. These devices are ideal for a large-scale gas exchange process with slow kinetics as they provide a large contact surface area per unit volume for the two fluids that need to exchange gas(es). The most common drawbacks of HFMCs for carbon capture are cost, pressure drop, and membrane fouling [147].

In this paper, we examine the use and feasibility of HFMCs for DOC. The proposed HFMC would flow seawater on shell side and a solvent on the tube side, driving CO_2 through the membrane from the seawater side into the solvent side, as shown in Figure 13.

On the solvent side, we investigate the use of aqueous sodium hydroxide (NaOH) because 1) NaOH is benign if it leaks into the ocean [9], 2) NaOH can osmotically balance with the surrounding seawater because of its sodium ions, 3) NaOH is a fast-acting CO_2 solvent that has already been well-characterized for DAC systems [128, 157, 46, 171, 194], and 4) NaOH has been studied for post-combustion CO_2 capture in marine environments, illustrating its potential for this system [59]. While solvent regeneration is not explored in this paper, regeneration of NaOH has been studied by other investigators for DAC systems [9, 209, 226], and the same regeneration methods could be employed for DOC. The primary goal of this work is to examine the efficacy of HFMCs at separating CO_2 from seawater using a NaOH solvent stream. To this end, lab-scale experimental data collection (Section 3.3) and computational modeling of HFMCs (Section 3.4) are used. A preliminary techno-economic assessment is then performed to determine the competitiveness of this technology with DAC systems (Section 3.6). The results of this work demonstrate that HFMCs with NaOH solution can remove CO_2 from seawater, and that this system could be cost-competitive with DAC if seawater pre-treatment or membrane surface treatment brings the local seawater pH down to improve CO_2 flux across the membrane.

3.3 Experimentation

3.3.1 Methodology

Hollow fiber membrane contactors (HFMCs) are a promising technology for direct ocean capture because they're a well-established carbon capture technology with a high packing density and easy module assembly [24]. In order to demonstrate their feasibility for this application, lab-scale experiments were conducted with a Liqui-Cel MM-1x5.5 Series Membrane Contactor purchased from 3M™. Synthetic seawater and NaOH solution were flowed through the two sides of the HFMC mini-module, and dissolved CO_2 readings were taken on samples at the seawater outlet, as shown in Figure 14. The physical experimental setup is shown in

Figure 15.

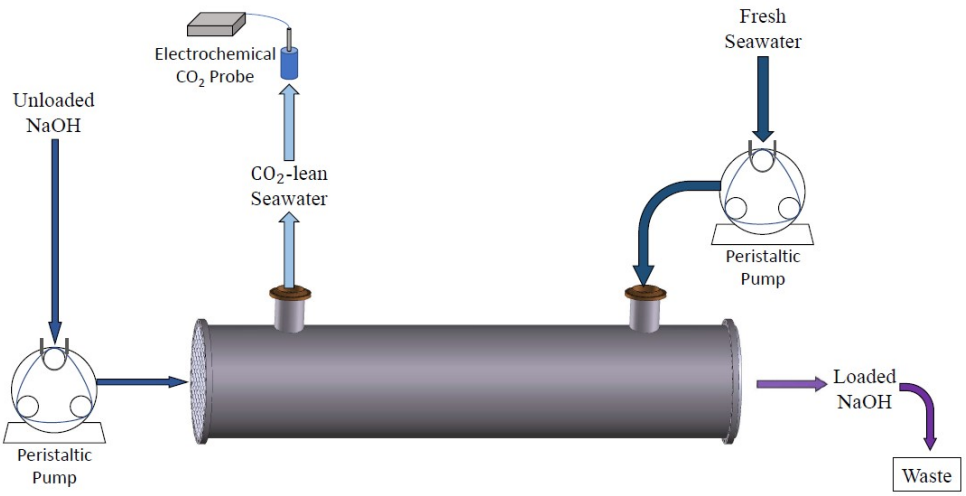

Figure 14: Schematic diagram of the laboratory experimental setup for direct ocean capture (DOC) using HFMCs. Counter-current flow is depicted as the seawater enters through the shell-side, and the solvent (NaOH solution) enters the tube-side of the membrane. Samples are taken at the seawater outlet to measure CO_2 concentration.

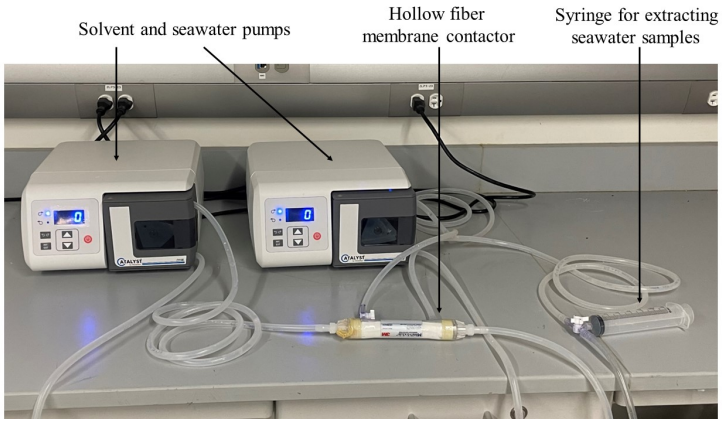

Figure 15: Picture of HFMC experimental setup at the University of Pittsburgh. The HFMC is in the center of the experiment, with pump tubing attached to each inlet and outlet. The two peristaltic pumps flow the seawater and NaOH through the HFMC module, and a syringe extracts samples from the seawater outlet periodically to measure dissolved CO_2 using a Thermo Fisher Scientific^{TM} sensor (not shown).

Synthetic seawater was prepared by mixing the proper proportion of Instant Ocean sea salt into deionized (DI) water. The solution was then exposed to air in an open container for at least 24 hours to allow the solution to equilibrate with the CO_2 in the surrounding air. 0.6 M NaOH solution was made by mixing DI water and NaOH pellets purchased from Belle Chemical. Before passing the liquids through the membrane apparatus, the Thermo Scientific™ Orion™ Versa Star pH/ISE Measurement Module (i.e. the CO_2 electrode) was calibrated using reference points obtained from CO_2 calibration standards purchased from Thermo Fisher Scientific™ and the synthetic seawater solution. During experiments, NaOH solution was pumped through the tube side while synthetic seawater was pumped through the shell side of the HFMC mini-module using Catalyst FH100 Peristaltic Pumps purchased from Cole-Palmer®.

A three-way stopper connected to an airtight syringe is built into the tubing on the seawater outlet side of the HFMC bundle. For each flow-rate combination tested, the CO_2 concentration in the seawater feed was measured. Data samples were then collected from the syringe at the seawater outlet after allowing both liquids to flow through the HFMC for 10 minutes to reach steady-state. At the 10 minute mark, three seawater samples were collected using the syringe. The Thermo Scientific™ Orion™ Versa Star pH/ISE Measurement Module was then used to measure dissolved CO_2 in the seawater samples. The results of these lab experiments are discussed in Section 3.5.

3.4 Modeling

3.4.1 Governing Chemistry of Ocean Water

The ocean's bicarbonate buffer system is governed by five equilibrium reactions that contain three participating dissolved inorganic carbon (DIC) species: $CO_{2(aq)}$, HCO_3^-, and CO_3^{2-} [213].[1]

$$H_2O_{(l)} + CO_{2,(aq)} \underset{k_{r1}}{\overset{k_{f1}}{\rightleftharpoons}} H^+ + HCO_3^- \tag{3.1}$$

$$CO_{2,(aq)} + OH^- \underset{k_{r2}}{\overset{k_{f2}}{\rightleftharpoons}} HCO_3^- \tag{3.2}$$

$$CO_3^{2-} + H^+ \underset{k_{r3}}{\overset{k_{f3}}{\rightleftharpoons}} HCO_3^- \tag{3.3}$$

[1] A fourth carbonaceous species, pure carbonic acid (H_2CO_3), is not included in the DIC term. This acid seldom exists in nature due to its rate of dissociation from H_2CO_3 into the bicarbonate anion (HCO_3^-) and is therefore assumed to entirely contribute to the initial concentration of $CO_{2(aq)}$.

$$HCO_3^- + OH^- \underset{k_{r4}}{\overset{k_{f4}}{\rightleftharpoons}} CO_3^{2-} + H_2O_{(l)} \tag{3.4}$$

$$H_2O_{(l)} \underset{k_{r5}}{\overset{k_{f5}}{\rightleftharpoons}} OH^- + H^+ \tag{3.5}$$

To model the instantaneous characteristics of each reaction, several relations between the equilibrium constants and their temperature-dependent expressions (Table 7) and the differential forward and backward rate constants of each reaction are needed (Table 8). Equations 3.6-3.10 describe the rates of accumulation in mol/s of each species in the seawater model:

$$rate_{CO_2} = (k_{r1}[H^+] + k_{r2}) - (k_{f1} + k_{f2}[OH^-])[CO_2] \tag{3.6}$$

$$\begin{aligned} rate_{HCO_3^-} = (k_{f1} + k_{f2}[OH^-])[CO_2] - (k_{r1}[H^+] + k_{r2})[HCO_3^-] + \\ (k_{f4}[H^+] + k_{r4})[CO_3^{2-}] - (k_{r3} + (k_{f4}[OH^-])[HCO_3^-] \end{aligned} \tag{3.7}$$

$$rate_{CO_3^{-2}} = (k_{r3} + k_{f4}[OH^-])[HCO_3^-] - (k_{f3}[H^+] + k_{r4})[CO_3^{2-}] \tag{3.8}$$

$$rate_{H^+} = k_{f1}[CO_2] - (k_{r1})[H^+][HCO_3^-] + (k_{r3}[HCO_3^-]) + (k_{f5}) - (k_{r5}[H^+][OH^-]) \tag{3.9}$$

$$\begin{aligned} ate_{OH^-} = (k_{r2}[HCO_3^-]) - (k_{f2}[OH^-][CO_2]) - (k_{f4}[OH^-][HCO_3^-]) \\ +(k_{r4}[CO_3^{2-}]) + (k_{f5}) - (k_{r5}[H^+][OH^-]) \end{aligned} \tag{3.10}$$

Table 6: Seawater pH and chemistry, derived using Henry's constant, K_H, for CO_2 diffusion between the atmosphere and ocean. The atmospheric partial pressure of CO_2 was set to 413 ppm [124, 125]. The temperature was assumed to be 298.15 K, with a salinity of 35 and K_H = 29.1144 atm/M [208]. The resulting total concentration of dissolved inorganic carbon (DIC) is compared against a tabulated value of approximately 2.3 mM [192].

Seawater Initial Condition	**Concentration (M)**
pH	8.05
$[CO_{2(aq)}]$	$1.4185x10^{-5}$
$[HCO_3^-]$	$2.2157x10^{-3}$
$[CO_3^{2-}]$	$2.9553x10^{-4}$
$[H^+]$	$8.9125x10^{-9}$
$[OH^-]$	$1.1220x10^{-6}$
$[DIC] = [CO_2]+[HCO_3^-]+[CO_3^{2-}]$	$2.5254x10^{-3}$

Table 7: Reaction equilibrium constants for seawater, and their dependence on temperature, T=298.15K, and salinity, S=35.

Equilibrium Constant	**Dependence on T and S**	**Ref.**
$K_1^* = \frac{[H^+][[HCO_3^-]}{[CO_{2(aq)}]} = 1.39 \times 10^{-6}$	$lnK_1^* = 2.83655 - \frac{2301.1266}{T} - (1.5529413\, lnT) - (0.20760841 + \frac{4.0484}{T})S^{0.5} + (0.08468345S) - (0.00654208S^{1.5}) + ln(1 - 0.001005S)$	[63]
$K_2 = \frac{[H^+][CO_3^{2-}]}{[HCO_3^-]} = 1.19 \times 10^{-9}$	$lnK_2 = -9.226508 - \frac{3351.6106}{T} - (0.2005743lnT) + (-0.106901773 - \frac{23.9722}{T})S^{0.5} + (0.11310822S) - (0.00846934S^{1.5}) + ln(1 - 0.001005S)$	[63]
$K_{w1} = [H^+][OH^-] = 6.06 \times 10^{-14}$	$lnK_{w1} = (\frac{-13847.26}{T}) + 148.9652 - 23.6521lnT + (\frac{118.67}{T} - 5.977 + 1.0465lnT)\sqrt{S} - 0.1615S$	[63]

Table 8: Reaction rate constants and their respective dependencies on temperature , T in K, and salinity, S [213]. The dependence of k_{f2} uses a value $A_4 = 499002.24 \times e^{(4.2986\times10^{-4}S^2+5.75499\times10^{-5}S)}$, and the ideal gas constant R = 8.31451 J/(mol· K) [63].

Rate Constant	**Value at T = 298.15 (K), S = 35**	**Dependence on T and S**	**Ref.**
k_{f1}	3.71 $\times10^{-2}$ (1/s)	$e^{(1246.98-(\frac{6.19\times10^4}{T})-(183\,lnT))}$	[122]
k_{r1}	2.67 $\times10^{4}$ (kg/mol·s)	$\frac{k_{f1}}{(K_1^*)}$	[213]
k_{f2}	2.23 $\times10^{3}$ (kg/mol·s)	$\frac{A_4\, e^{-90166.83(RT)}}{K_{w1}}$	[122, 18]
k_{r2}	9.72 $\times10^{-5}$ (1/s)	$\frac{k_{f2}K_{w1}}{K_1^*}$	[122]
k_{f3}	5.0 $\times10^{10}$ (kg/mol·s)	None	[26]
k_{r3}	59.44 (1/s)	$\frac{k_{f3}}{K_2}$	[122]
k_{f4}	6.0 $\times10^{9}$ (kg/mol·s)	None	[26]
k_{r4}	3.06 $\times10^{5}$ (1/s)	$\frac{k_{f4}K_{w1}}{K_2}$	[122]
k_{f5}	1.40 $\times10^{-3}$ (kg/mol·s)	None	[26]
k_{r5}	2.31 $\times10^{-3}$(kg/mol·s)	$k_{f5}K_{w1}$	[122]

3.4.2 Governing Chemistry of NaOH Solvent

The absorption of CO_2 in aqueous NaOH solutions proceeds through the following set of reactions [47]:

$$CO_2 + OH^- + \underset{k_{r6}}{\overset{k_{f6}}{\rightleftharpoons}} HCO_3^- \tag{3.11}$$

$$HCO_3^- + OH^- \underset{k_{r7}}{\overset{k_{f7}}{\rightleftharpoons}} CO_3^{2-} + H_2O \tag{3.12}$$

$$OH^- + H^+ \underset{k_{r8}}{\overset{k_{f8}}{\rightleftharpoons}} H_2O \tag{3.13}$$

$$CO_2 + H_2O \underset{k_{r9}}{\overset{k_{f9}}{\rightleftharpoons}} HCO_3^- + H^+ \tag{3.14}$$

The individual rates of accumulation for each species in the NaOH solution are calculated using each reaction's rate and equilibrium constants, their respective temperature-dependent expressions (Table 9), and the following equations:

$$rate_{CO_2} = k_{r6}[HCO_3^-] - k_{f6}[CO_{2(aq)}][OH^-] + k_{r9}[HCO_3^-][H^+] - k_{f9}[CO_{2(aq)}] \tag{3.15}$$

$$\begin{aligned} rate_{OH^-} = {} & k_{r6}[HCO_3^-] - k_{f6}[CO_{2(aq)}][OH^-] + k_{r7}[CO_3^{2-}] \\ & - k_{f7}[HCO_3^-][OH^-] + k_{r8} - k_{r8}[OH^-][H^+] \end{aligned} \tag{3.16}$$

$$\begin{aligned} rate_{HCO_3^-} = {} & k_{f6}[CO_{2(aq)}][OH^-] - k_{r6}[HCO_3^-] + k_{r7}[CO_3^{2-}] \\ & - k_{f7}[HCO_3^-][OH^-] + k_{f9}[CO_{2(aq)}] - k_{r9}[HCO_3^-][H^+] \end{aligned} \tag{3.17}$$

$$rate_{CO_3^-} = k_{f7}[HCO_3^-][OH^-] - k_{r7}[CO_3^{2-}] \tag{3.18}$$

$$rate_{H^+} = k_{r8} - k_{f8}[OH^-][H^+] + k_{f9}[CO_{2(aq)}] - k_{r9}[HCO_3^-][H^+] \tag{3.19}$$

Table 9: Rate and equilibrium constant values at 297 K are provided for equation 3.15 - equation 3.19 along with their respective temperature-dependent expressions, which are valid for temperatures between 291 K and 314 K. Here, k_{f6}^{∞} is the forward rate constant for k_{f6} at infinite dilution. The density of water, ρ_w, is assumed to be constant at 997 kg/m^3. The concentrations of Na^+ and CO_3^{2-} are set to 1.0 M and 0.5 M, respectively. "N/A" indicates that a reaction constant does not vary with respect to temperature [47].

Rate Constant	**Value at T = 298.15 K, S = 35**	**Dependence on T and S**	**Ref.**
k_{f6}	7.809 $\times 10^1$ (m^3/mol $\cdot$ s)	$\log(\frac{k_{f6}}{k_{f6}^{\infty}})$=1.1$\times 10^{-4}$ [Na^+] + 1.7 $\times 10^{-4}$ [CO_3^{2-}]	[187]
k_{r6}	1.703 $\times 10^{-4}$ (1/s)	$\frac{k_{f6}K_{w2}}{K_3}$	[70]
k_{f7}	6 $\times 10^6$ (m^3/mol $\cdot$ s)	None	[72]
k_{r7}	1.211 $\times 10^6$ (1/s)	$\frac{k_{f7}}{K_4}$	[112]
k_{f8}	1.40 $\times 10^8$ (m^3/mol $\cdot$ s)	None	[72]
k_{r8}	1.280 $\times 10^0$ (m^3/mol $\cdot$ s)	$\frac{k_{f8}}{K_{w2}}$	[223]
k_{f9}	2.4 $\times 10^{-2}$ (1/s)	None	[223]
k_{r9}	5.71 $\times 10^1$ (m^3/mol $\cdot$ s)	$\frac{k_{f9}}{K_3}$	[223]
K_3	4.193 $\times 10^{-4}$	$e^{(-(12092.1(T)^{-1})-36.781ln(T)+235.48)}$	[70]
K_4	4.956 $\times 10^0$	$log(K_4) = 1568.94(T)^{-1} - 2.5866 - (6.737 \times 10^{-3}T)$	[112]
K_{w2}	9.143 $\times 10^{-9}$	$log(\frac{K_{w2}}{\rho_w^2}) = -5839.5(T)^{-1} - 22.477log(T) + 61.206$	[223]

3.4.3 Governing Mass Transport

A 1D model using the resistance-in-series (RIS) approach [156] was developed to simulate the performance of an HFMC for direct ocean capture. This approach was taken because it is the simplest approach and has produced successful results for other similar applications [255, 35, 91, 199]. The RIS model is widely trusted in the gas separation field and is a simple, effective means of determining the rate of CO_2 transfer in HFMCs by breaking down the

mass transfer process into a series of steps: CO_2 diffusion through the gas, CO_2 diffusion through the membrane, and CO_2 diffusion through the liquid (as shown in Figure 16). In order to apply this approach, the following assumptions were made: steady-state, isothermal, uniform membrane properties; no membrane wetting; no axial mixing; and no deformation due to pressure effects.

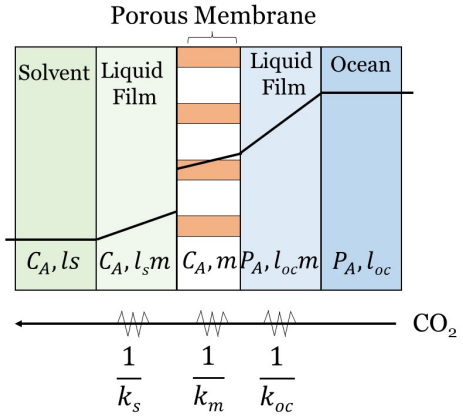

Figure 16: Our resistance-in-series (RIS) model for CO_2 transport in a seawater/solvent HFMC. There are mass transfer resistances associated with the tube-side liquid phase, the membrane, and the shell-side liquid phase. Each resistance can be expressed as the inverse of the mass transfer coefficient for that phase. The layers included to accomplish this analysis are the liquid on the solvent side, the solvent liquid film, the membrane, the ocean liquid film, and the liquid on the ocean side. Figure was modified from [201]

.

The CO_2 flux across the HFMC is given by multiplying the overall mass transfer coefficient by the CO_2 concentration difference, ΔC_{CO_2}:

$$J_{CO_2} = K_{ov} \Delta C_{CO_2}, \tag{3.20}$$

where the RIS model is used to determine the overall mass transfer coefficient, K_{ov}:

$$\frac{1}{K_{ov}} = \frac{1}{k_{shell}} + \frac{1}{k_{mem}} + \frac{1}{k_{lumen}} \tag{3.21}$$

Mass transfer correlations are needed to determine the two liquid-side mass transfer coefficients, k_{shell} and k_{lumen}. For this model, the ocean water flows through the shell side, and the solvent flows through the lumen side. The ocean mass transfer coefficient (k_{shell}) is given by:

$$k_{shell} = \frac{Sh D_{CO_2}}{d_h}. \tag{3.22}$$

where D_{CO_2} (m^2/s) is the diffusivity of CO_2 in the ocean, d_h (m) is the hydraulic diameter, and Sh is the Sherwood number. The hydraulic diameter is defined as $d_h = 4(\frac{\pi D^2}{4N} - \frac{\pi D_o^2}{4})/(\pi d_o)$, where D (m) is the module diameter, N is the number of fibers and d_o is the outer fiber diameter.

The solvent mass transfer coefficient, k_{lumen}, is defined similarly:

$$k_{lumen} = \frac{ShD_{CO_2}}{d_i}, \tag{3.23}$$

where D_{CO_2} (m^2/s) is the diffusivity of CO_2 in the solvent, d_i (m) is the inner fiber diameter, and Sh is the Sherwood number correlation for flow through a tube (or lumen-side). The Sherwood correlations for both sides of the membrane were proposed by Yang and Cussler for laminar flow on the shell and lumen sides of cylindrical fibers [240]. The Sherwood number correlation for the shell side is given by:

$$Sh_{shell} = 1.25\left(\frac{d_h Re}{L}\right)^{0.93} Sc_{CO_2}^{0.33} \tag{3.24}$$

where d_h (m) is the hydraulic diameter, L (m) is the membrane length, Re is the Reynolds number, and Sc_{CO_2} is the Schmidt number. The Reynolds number is given by: $Re = \frac{\rho V d_h}{\mu}$, where ρ (kg/m^3) is the fluid density, V (m/s) is the velocity, and μ (Pa ·s) is the dynamic viscosity. The Schmidt number is defined using the kinematic viscosity, ν (m^2/s), and the diffusivity of CO_2 in seawater ($D_{CO_2,oc}$): $Sc_{CO_2} = \frac{\nu}{D_{CO_2,oc}}$. The Sherwood number correlation on the lumen side is defined using the inner fiber diameter, d_i (m), the membrane length, L (m), and the Reynolds number, Re:

$$Sh_{lumen} = 1.62\left(\frac{d_i Re}{L}\right)^{0.33} \tag{3.25}$$

If we decided to flow seawater on the lumen side and solvent on the shell side, then the inner and hydraulic diameters, d_i and d_h, in these equations would need to be swapped. Zhao et al. discuss the advantages and disadvantages of modeling the solvent on the tube and shell sides [255], and we consider both flow arrangements in our parametric studies later in this paper.

The membrane mass transfer coefficient is also needed to determine the overall mass transfer coefficient:

$$k_m = \frac{D_{eff}}{\delta} \tag{3.26}$$

where the effective diffusivity in the membrane, $D_{eff} = (D_{CO_2}\varepsilon)/\tau$, is defined as the diffusivity of CO_2 in m^2/s, multiplied by the ratio of the porosity to tortuosity of the membrane. The effective diffusivity is divided by the thickness of the membrane, δ (m) [177].

In addition to obtaining the CO_2 removal rate from the seawater, the overall pressure

drop is calculated for the tube and shell sides of the HFMC. The pressure drop for flow through the tube-side is calculated using the Hagen-Poiseuille equation:

$$\Delta P_{tube} = \frac{128 Q \mu_s L}{N \pi d_i^2} \tag{3.27}$$

where Q (m^3/s) is the total flow-rate through the fibers, μ_s ($Pa \cdot s$) is the viscosity of the solvent at the corresponding temperature, L (m) is the length of the fiber, N is the number of fibers, and d_i (m) is the inner fiber diameter. The pressure drop for the shell side is calculated using Equation 3.28 [178]:

$$\Delta P_{shell} = \frac{192 Q \mu_{oc} N L d_o (D + N d_o)}{\pi (D^2 - N d_o^2)^3} \tag{3.28}$$

where d_o (m) is the outer fiber diameter, μ_{oc} (Pa·s) is the viscosity of the seawater, and D (m) is the inner diameter of the module.

3.4.4 1D MATLAB® Model

The 1D, steady-state model for laminar flow through an HFMC was created using MATLAB®. The model calculates the CO_2 removal rate on a per stage basis along the length of the fibers for either the co-flow or counter-current flow configuration. The numerical scheme of the code is shown in Figure 17.

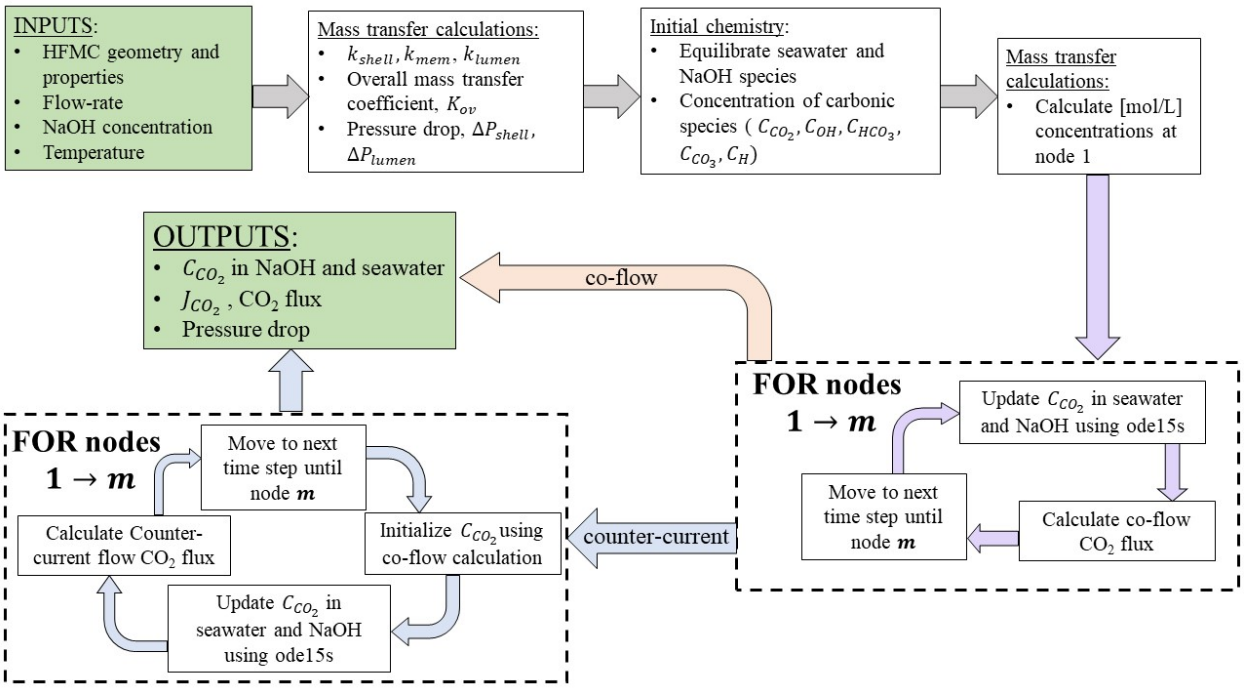

Figure 17: Flow-chart of the 1D, steady-state model used to solve for CO_2 flux in an HFMC exposed to NaOH solvent and seawater. The step-by-step process is illustrated for both the co-current and counter-current flow configurations. The co-current model only needs to iterate through the first loop (with purple arrows), whereas the counter-current model needs to also iterate through the second loop (with blue arrows) after completing the first loop.

Each model is subdivided into nodes along the length of the fibers, as shown in Figure 18. The ocean and solvent domains are illustrated using blue and green, respectively. CO_2 flux at each node ($J_{CO_2,i}$) is determined by the difference in CO_2 concentrations between the seawater and solvent at that node ($C_{CO_2,oc,i} - C_{CO_2,s,i}$), and the overall mass transfer coefficient at that node (K_{ov} from Equation 3.21).

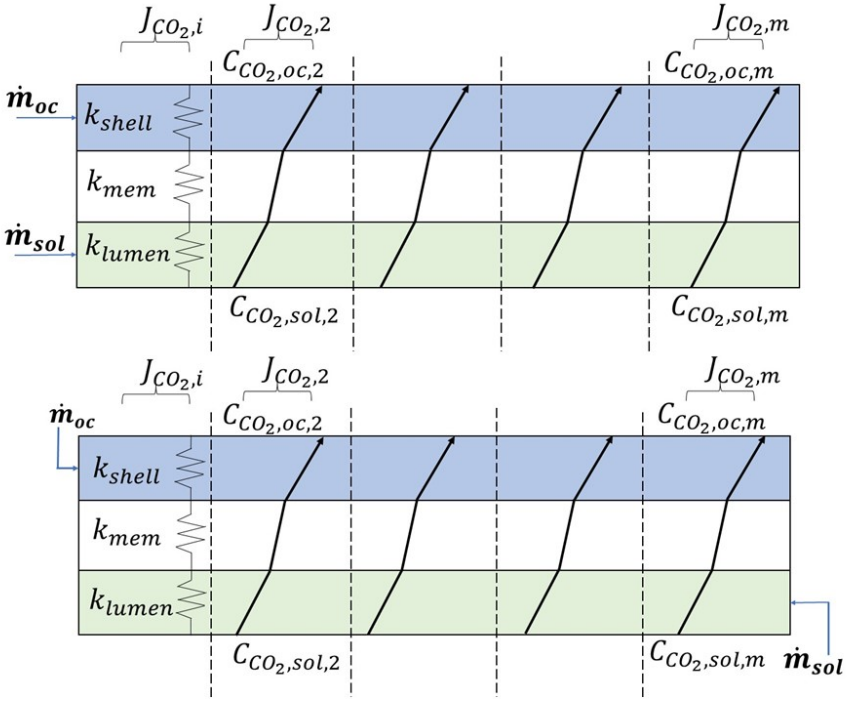

Figure 18: Graphics of 1D Matlab ® models for co-current (top) and counter-current (bottom) HFMC flow configurations. The seawater domain is blue; the membrane domain is white; and the solvent domain is green. The model is 1D in the flow-direction of the seawater, and the CO_2 flux at each node ($J_{CO_2,i}$) is determined by the concentration difference in that node and overall mass transfer resistance at that node.

3.5 Results and Discussion

3.5.1 Model Validation

The purpose of this section is to validate our 1D MATLAB® model against lab-scale experiments. The properties of our lab-scale membrane device and experimental conditions are summarized in Table 10. The membrane properties in this table come from the specification sheet for the 3M® mini-module used in our lab. All of the properties listed in Table 10 were put into our 1D model in order to compare it to our experimental data. No fitting parameters or unknown inputs were used in this validation to fit the model to our data.

Table 10: Membrane device properties and other parameters from our lab-scale experiment that were inputs to our 1D model to perform our validation.

Lab-scale Membrane Properties [2]		**Other Lab-Scale Experimental Conditions**	
Material	Polypropylene/ Polyurethane	Flow rate (mL/min)	10-1000
Shell-side volume (mL)	25	Temperature (K)	298
Tube-side volume (mL)	16	D_{CO_2} (m^2/s)	2.3227E-9
Number of fibers	2.3E3	ρ (kg/m^3)	1.0233E3
Outer fiber diameter (m)	3E-4	μ_{oc} (Pa ·s)	9.661E-4
Inner fiber diameter (m)	2.3E-4	μ_{sol} (Pa · s)	8.988E-4
Hydraulic diameter (m)	0.025	Salinity	35
Membrane length (m)	0.1		
Porosity	0.5		

We tested a range of seawater flow-rate ratios experimentally and collected multiple samples at the seawater outlet to measure CO_2 outlet concentration at each flow-rate ratio. The experiments were conducted in the co-current configuration for seawater:solvent flow ratios of 1:1, 2:1, 4:1 and 8:1. The seawater was pumped through the shell side of the HFMC, and 0.6 M NaOH solution was pumped through the tube side of the HFMC, as shown in Figure 14. The results of this experiment are compared to MATLAB® model predictions in Figure 19. The experimental results are in moderate agreement with the code predictions for seawater outlet CO_2 concentration, especially considering that we used no fitting parameters to get our model to match the experimental data. The main reason for the discrepancies between the experimental and the modeled results is that the Thermo Scientific™ Orion™ CO_2 electrode sensor becomes less accurate at lower CO_2 concentrations (below 4.4 ppm). For future work, a new sensor designed for accurate low CO_2 concentration measurements should be used. An in-line CO_2 sensor should also be used in the future to limit atmospheric exposure to the sample collected at the seawater outlet while transferring it to be measured. In addition, the HFMC used for the experiment was additionally used for testing trial runs. After months of use, it is safe to assume some wetting might have occurred which could

alter the final CO_2 concentration. However, these results demonstrate that CO_2 can be removed experimentally from seawater using our proposed HFMC design. These results also demonstrate that our model does a decent job of predicting performance.

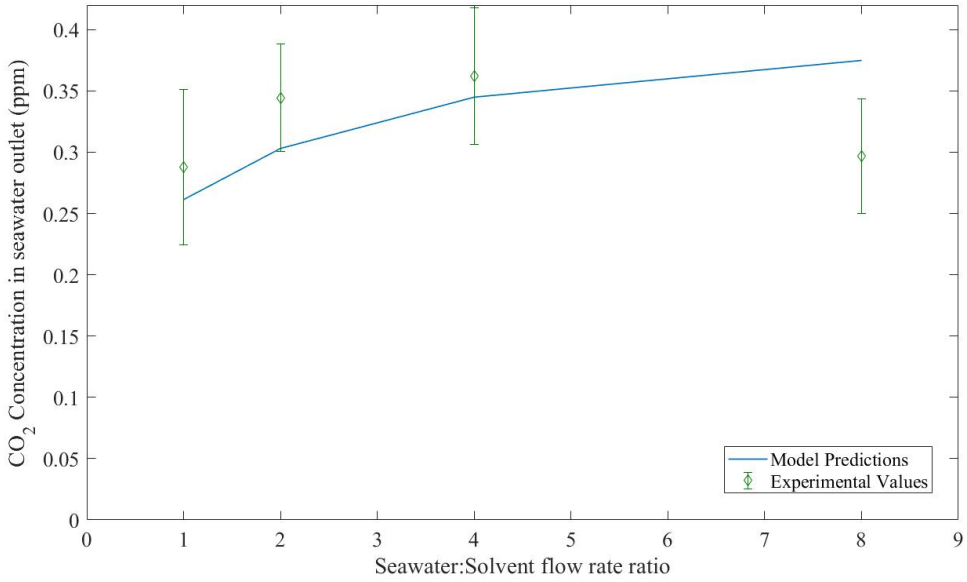

Figure 19: CO_2 concentration in seawater outlet vs. seawater:solvent flow ratio for lab-scale experiments (shown as green markers with error bars) and our 1D Matlab model (shown as a solid blue line). Error bars were calculated by taking the sample standard deviation for all data collected at the given flow-rate ratio. Solvent flow-rate was fixed at 200 mL/min for all results, while seawater flow-rate was varied from 200-1200 mL/min.

3.5.2 Parametric Studies

The previous validation section used a small, lab-scale membrane device in order to compare our model to the data collected with our mini-module in the lab. However, for the rest of this paper, we will work with a much larger membrane from the 3M® catalog in order to predict performance of a full-scale membrane bundle that could be used for pilot and commercial systems. The membrane dimensions for our large-scale membrane bundle are compared to the dimensions of our lab-scale bundle in Figure 20.

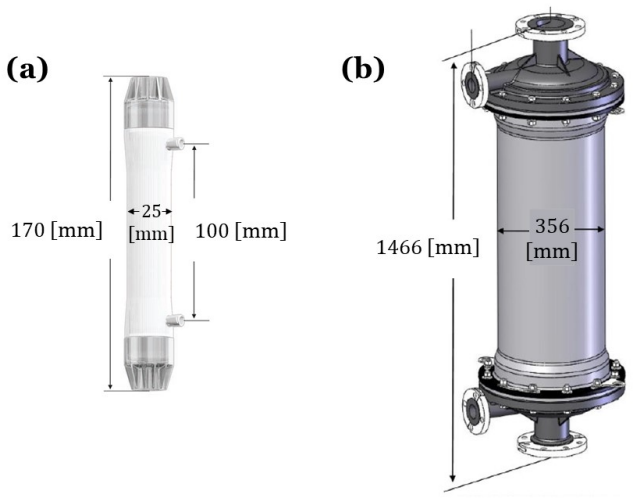

Figure 20: HFMC bundle dimensions for a) our lab-scale experiments and model validation (Section 3.5.1), and b) the full-scale model parametric studies ($\sim$ 8x larger) and TEA (Sections 3.5.2 - 3.6). Membrane dimensions for both devices come from 3M™'s specification sheets [2, 1]

.

The dimensions of the larger bundle shown in Figure 20 are used for the rest of this paper come from the 3M™ Liqui-Cel
texttrademark EXF-14x40 Membrane Contactor [1]. Table 11 details the membrane properties and other parameters that are inputs to our model to match this larger bundle design.

Table 11: Membrane bundle properties and other model input parameters used to model a large HFMC bundle in Matlab®.

Large Membrane Bundle Properties [1]		**Other Model Input Parameters**	
Material	Polypropylene	Velocity (m/s)	0.5 - 10
Shell-side volume (L)	51.3	Temperature (K)	298 - 308
Tube-side volume (L)	23.8	D_{CO_2} (m^2/s)	2.3227E-9
Number of fibers	1.95E5	ρ_{oc} (kg/m^3)	1.0233E3
Outer fiber diameter (m)	3E-4	ρ_{sol} (kg/m^3)	9.97E2
Inner fiber diameter (m)	2.3E-4	μ_{oc} ($Pa \cdot s$)	9.661E-4
Hydraulic diameter (m)	0.0019	μ_{sol} $Pa \cdot s$)	8.988E-4
Membrane length (m)	1.016	Salinity	35
Porosity	0.5		

i Impact of Flow Configuration on Performance

Flow configuration (co-flow vs. counter-flow) and liquid placement (shell- vs. tube-side) are studied here to determine the optimal conditions for CO_2 removal rate. Figure 21 compares CO_2 fluxes for the co-current and counter-current configurations and for seawater on the shell side vs. the tube side of the membrane. The results from Figure 21 indicate that flow configuration has a minimal effect on CO_2 flux. The similar performance of co-current and counter-current makes sense in light of the fact that CO_2 loading is minimal in the NaOH solution along the length of the membrane. Therefore, running NaOH solution counter-current to the seawater doesn't add much benefit since the inlet and outlet CO_2 concentrations in the NaOH are so similar. However, CO_2 flux does increase when pumping seawater through the shell side of the membrane rather than the tube side. This result indicates that the mass transfer resistance on the tube side is more dominant, therefore decreasing flux, due to the smaller fiber volume in relation to the shell side (i.e., Equation 3.22 uses the hydraulic diameter rather than the inner diameter of the fiber). Based on the results in Figure 21, we can conclude that flowing seawater on the shell-side increases CO_2 flux, but co-current and counter-current flow result in similar CO_2 fluxes. The remaining results presented in this section will only illustrate counter-current flow with the seawater flowing through the shell side.

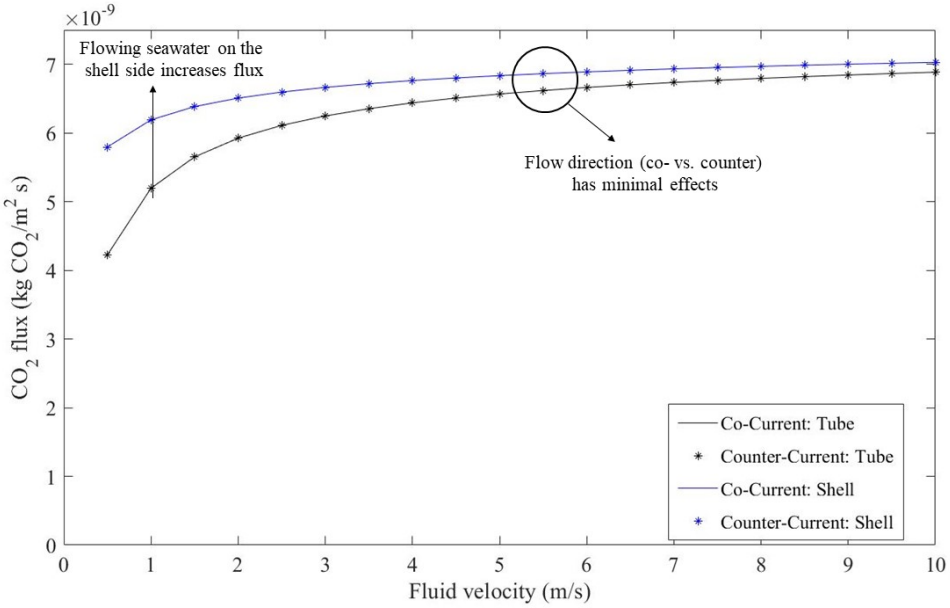

Figure 21: Modeled CO_2 flux vs. velocity of both liquid for four designs: co-current vs. counter-current for seawater on the tube side and seawater on the shell side. The * symbols represents counter-current flow, and co-current flow is represented by lines. The blue lines and markers depict seawater flowing through the shell side, and the black lines and markers depict seawater flowing through the tube side. There are minimal effects between flowing the liquids in co- or counter-current direction. However, flowing seawater on the shell side increases flux.

ii **Pressure Drop in the HFMC**

Pressure drop is an important factor in designing a HFMC device, so we investigate the pressure drop across the tube- and shell-sides of the device over a range of fluid velocities here. Figure 22 shows the pressure drop as a function of fluid velocity on both sides of the HFMC. As expected, the shell-side velocity is smaller than the tube-side due to the fact that fluid has to flow through narrow channels on the tube-side. Whereas pressure drop stays below 10 bar on the shell-side even at 10 m/s, the tube-side pressure drop quickly rises above 10 bar at a fluid velocity of just 1.5 m/s. These results indicate that fluid velocity on the tube-side should be kept small to minimize pressure drop and therefore operating costs. Furthermore, these results provide further justification for flowing seawater on the shell side because seawater will need to flow much faster than the solvent in order to provide sufficient CO_2 and give the solvent time to load.

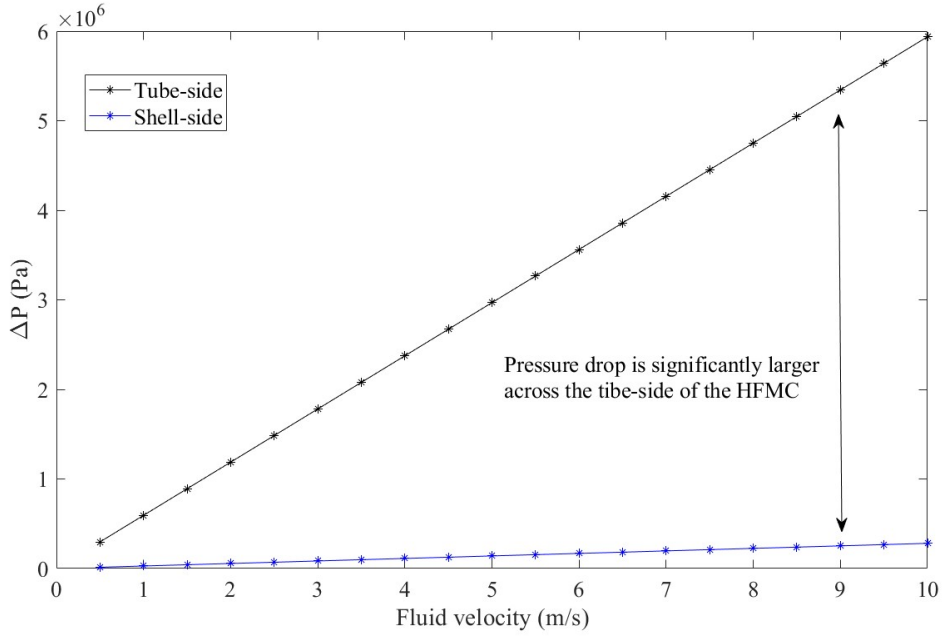

Figure 22: Pressure drop across the shell-side and tube-side of the HFMC bundle as a function of fluid velocity. Pressure drop is minimal across the shell-side, but increases dramatically with respect to velocity across the tube-side.

iii **Effect of temperature**

The effect of temperature on CO_2 flux is shown in Figure 23 for a 1:1 seawater:solvent flow ratio. The operating temperature was varied from 292 – 308 (K) in accordance with the temperature limits of our kinetic models. This temperature range is also around the national average temperature range of surface seawater. As shown in Figure 23, CO_2 flux increases with increasing operating temperature. This is expected because the rate of the absorption reaction between NaOH and CO_2 increases with temperature. These results suggest that our technology might be better suited for seawater at warmer climates.

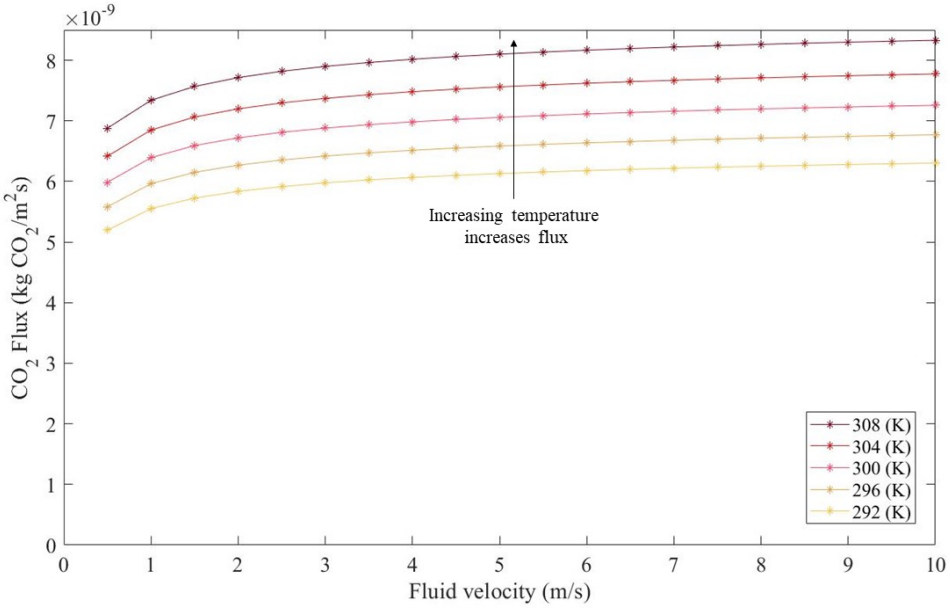

Figure 23: CO_2 flux (kg/m^{2}s) as a function of solvent and seawater velocity (m/s) for a range of temperatures (K). Lighter colors correspond to lower temperatures; darker colors correspond to higher temperatures. CO_2 flux increases with respect to temperature.

iv **Effect of membrane thickness**

Figure 24 shows CO_2 fluxes for a range of membrane thicknesses. The membrane thickness was varied in order to observe the role of membrane mass transfer resistance in the system. As expected, the CO_2 flux increases as the membrane thickness decreases. More specifically, CO_2 flux roughly doubles when the membrane thickness is halved from 40 to 20 microns. This indicates that membrane mass transfer resistance is a dominant resistance in the overall mass transfer process. These results imply that more effort should be focused on minimizing membrane thickness than on minimizing other mass transfer resistances in order to optimize CO_2 flux for our system.

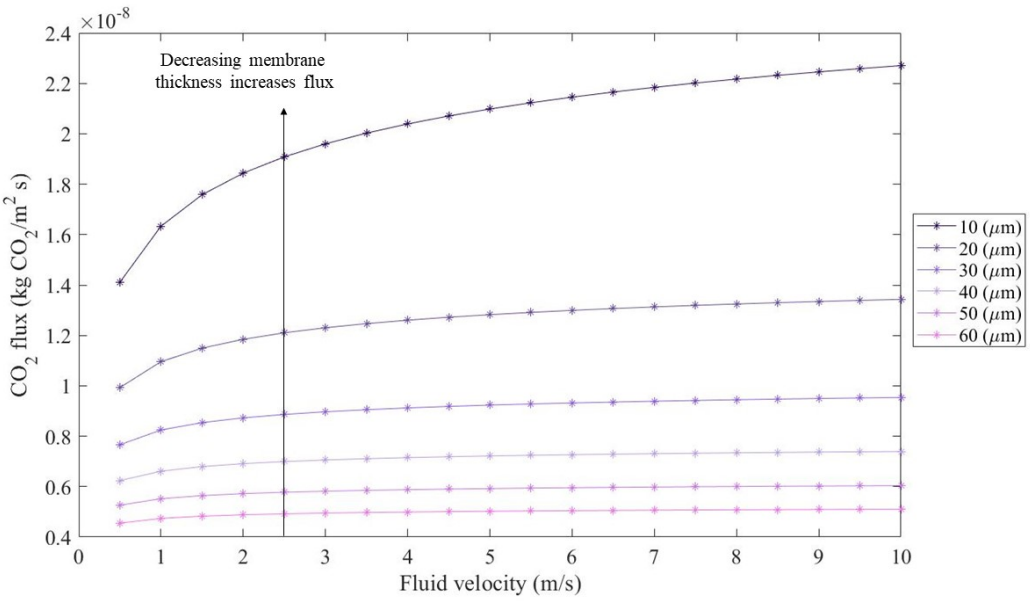

Figure 24: CO_2 flux as a function of fluid velocity for a range of membrane thicknesses. Lighter colors correspond to thicker membranes; darker colors correspond to thinner membranes. Decreasing the membrane thickness dramatically increases the CO_2 flux.

3.5.2.1 Loading Time Study

The previous parametric studies all assumed that unloaded NaOH solvent flowed once through a HFMC device and never recirculated. However, in a real system, this would likely lead to very low NaOH loading and therefore high regeneration costs since a lot of solvent would need to be regenerated to extract a small amount of CO_2. In order to investigate how long NaOH solvent would need to be in contact with seawater to fully load, we ran our model under conditions where the solvent was held stagnant on one side of the HFMC while seawater flowed on the other side. For this study, the temperature was varied from 292-308 (K) to study the impact of temperature on loading time. Seawater velocity was fixed at 10 m/s, and all other model parameters were fixed at the values listed in Table 11. Based on the results of this study (shown in Figure 25), the solvent reached a final capacity of around 0.38-0.39 mol CO_2/L over the course of 16-20 hours (higher temperatures result in faster loading). This loading time on the order of hours is consistent with DAC processes, which tend to be slower than point-source capture processes due to the lower CO_2 concentrations [170, 123]. Since the residence time for NaOH solution flowing through an HFMC is on the order of seconds rather than hours, a real system would either need to recirculate NaOH solution many times or hold it stagnant until it loads before regenerating (a batch process).

This is a practical system design limitation that should be explored further in future work.

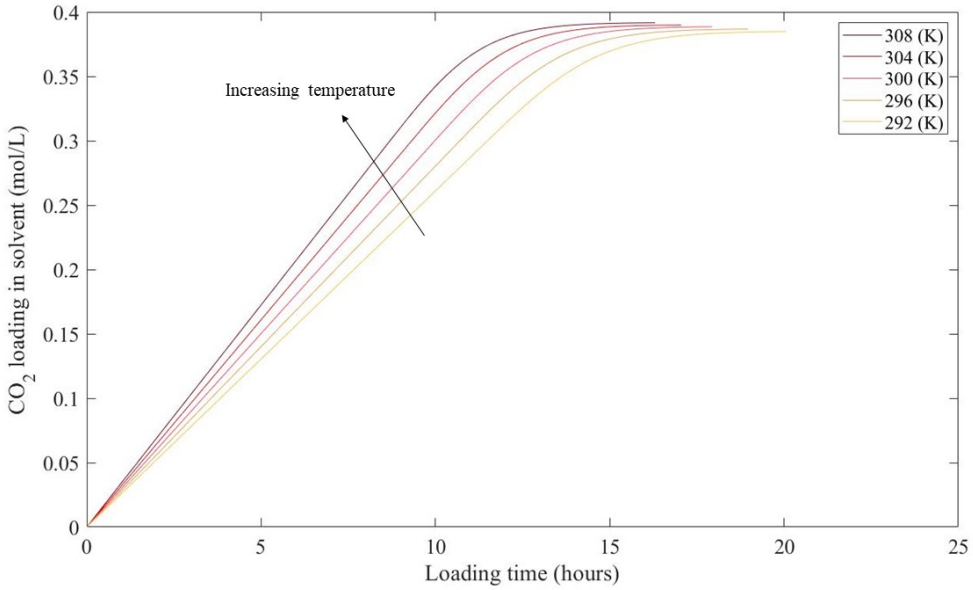

Figure 25: NaOH solvent loading as a function of time for stagnant solvent-exposed to fresh seawater in an HFMC. The maximum observed capacity is approximately 0.38-0.39 (mol CO_2/L) and is reached at around 16-20 hours.

3.6 Techno-Economic Assessment

A preliminary techno-economic assessment (TEA) was performed to determine the feasibility of scaling up this concept to a large direct ocean capture facility. Due to the novelty of the system design, the TEA was based on a theoretical system mimicking a direct air carbon capture plant. For this TEA study, we used the time-averaged CO_2 flux for 300 K obtained from our NaOH loading study (Section 3.5.2.1), which came out to 5.839e-09 (kg CO_2/m^2s). The system size was matched to the CO_2 capture rate of Carbon Engineering's proposed DAC system, which captures 980,000 CO_2 tonnes/year [126]. The TEA here considers both capital and operating costs for all components needed for absorption, regeneration and CO_2 compression for a greenfield installation. A simplified graphic of the capture and regeneration process is shown in Figure 26 to highlight the components that were considered.

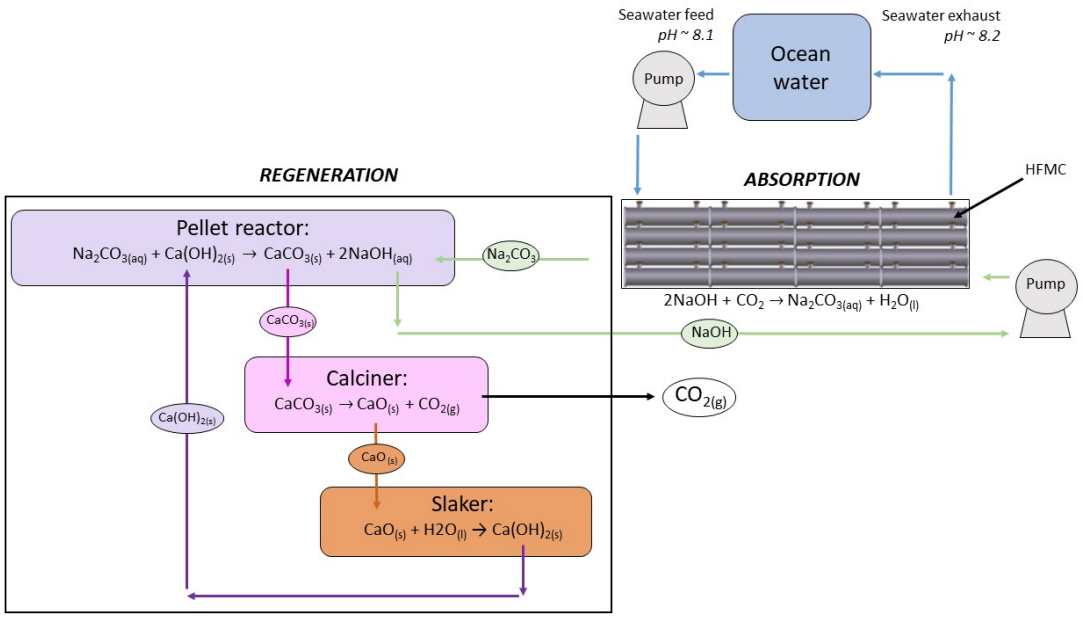

Figure 26: Graphic of our proposed system design for HFMC direct ocean capture. Many HFMC contactor bundles separate CO_2 from seawater using NaOH solution, increasing the seawater pH. The regeneration process is the same one used by Keith et al. [128] to regenerate NaOH solution for DAC. The pellet reactor converts Na_2CO_3 back to NaOH; the calciner removes CO_2 from $CaCO_3$, and the slaker converts CaO to $Ca(OH)_{2(s)}$ [58].

The breakdown of the capital and operating costs for our system is given in Table 12. The equivalent annual operating cost (EAOC) in Table 12 is calculated using the equation below, where YOC is the yearly operating costs, $i = 10\%$ is the assumed discount rate, and $n = 20$ years of plant life [134]:

$$EAOC = CapitalCost(\frac{i}{1-(1+i)^{-n}}) + YOC \tag{3.29}$$

Table 12: Estimated capital and operating costs for a direct ocean capture HFMC plant that captures 980,000 CO_2 tonne/year. The total capital and equivalent annual operating costs (EAOC) shown are based on a seawater pH of 8.1 and all costs are in 2022 Dollars, where K is thousands, M is millions, and B is billions.

Capital Costs			
Equipment	**Quantity**	**Unit Cost**	**Reference**
0.6 M of NaOH	4.20E08	\$4.04/lb	American Elements® Quote
EXF 14x40 HFM	2.61E4	\$ 5K/HFM	3M™ Quote with 20% Discount
Seawater pump	5.06E07	\$ 7.5K/pump	Sulzer Quote
NaOH pump	5.06E06	\$ 7.5K/pump	Sulzer Quote
CO_2 compressor		\$ 17.2M	[129]
Slaker		\$ 4.38M	[129]
Calciner		\$ 4.38M	[129]
Pellet Reactor		\$ 76.9M	[129]
Total Capital Costs		**\$ 93.2B**	
Operating Costs			
Pumps for seawater	1 year	\$ 7.59B	[127, 126, 3]
Pumps for NaOH	1 year	\$75.9M	[127, 126, 3]
Regeneration	1 year	\$74.5K	[129]
Total Operating Costs		**\$8.34B**	
EAOC		**\$ 8.83B**	
CO_2 Costs	\$ / tonne CO_2	9,565	

As shown in Table 12, the cost of a plant based on our technology is exorbitant in comparison with benchmark DAC costs ($\sim$ 16x more expensive) of a few hundred dollars per tonne of captured CO_2. The main reason the cost is so high is due to the low CO_2 fluxes, which are a result of the low CO_2 concentrations in seawater. Although our previous parametric studies show that optimizing some input variables (e.g. flow-rate, temperature, membrane thickness) can improve CO_2 flux, the benefit of optimizing these parameters will be insufficient to make this system cost-competitive with DAC. One way to make DOC cost-competitive with DAC is to lower the pH of the seawater, which in turn releases gaseous CO_2 and increases CO_2 flux (reducing the number of membranes needed). We ran our 1D model for pH values ranging from 5 - 8.1 and updated the carbonaceous species concentrations for each corresponding pH. Figure 27 shows the cost of capture per tonne of CO_2 for four pH values: 5, 6, 7 and 8.1 (current ocean pH), and shows the capital, operating, and EAOC cost breakdown per pH. For this analysis, we assumed that the membrane cost would double

each time the pH was lowered another whole number to account for the extra cost of locally treating seawater pH. As shown, the capture cost decreases dramatically as pH drops, even after introducing additional cost that account for membrane surface treatment to lower the pH. This result suggests that the primary way to drive down system cost is to reduce the number of membranes (by reducing the pH, which in turn raises CO_2 flux).

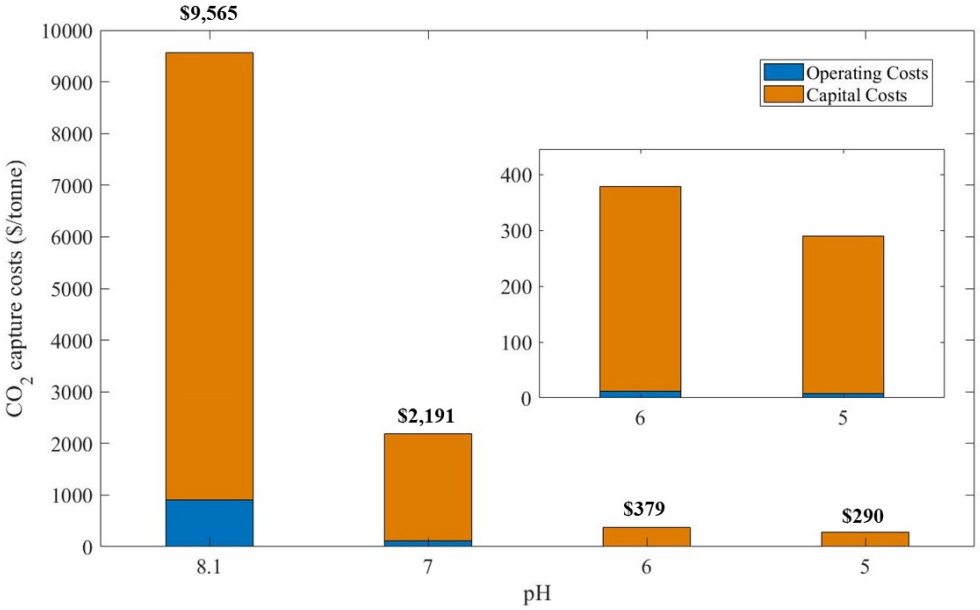

Figure 27: Cost per tonne of CO_2 captured for four pH's. Each bar is broken down into operating costs (in blue) and capital costs (in orange). The results show a significant decrease in capture cost as pH decreases, although capital costs seem to be the dominating contributor. This could be because of the number of membranes needed to achieve similar capture costs as the DAC system that is being compared.

The results of this preliminary TEA indicate that our proposed design is prohibitively expensive unless the seawater pH is lowered. However, the technology becomes competitive with state-of-the-art direct air capture systems (∼$200-300 dollars/tonne CO_2) if local pH can be lowered below about 6. Further research should be focused on membrane surface treatment of HFMCs to raise CO_2 flux and make them competitive with DAC technologies. Although it would be energy-intensive to lower the pH of the entire seawater stream [237, 73], one promising workaround is to passively lower the local pH of seawater at the membrane surface by adding chemical groups to the membrane surface on the seawater side. For example, introducing carbonic anhydrase (a mimic of the enzyme in mammal blood that converts bicarbonate to gaseous CO_2) could significantly raise gaseous CO_2 levels at the membrane surface. Carbonic anhydrase has been coated on HFMCs for flue gas carbon capture, and has significantly raised CO_2 fluxes [15, 94]. This catalyst has also been incorporated into

HFMC systems that focus on CO_2 separation from blood flow following similar methodologies [173, 221].

3.7 Conclusions

In this paper, we successfully demonstrated through lab-scale experiments and simulations that CO_2 can be separated from seawater using HFMCs. We were able to validate our 1D MATLAB® model using lab-scale dissolved CO_2 measurements on an HFMC mini-module. Parametric studies using our 1D Matlab model showed that CO_2 flux can be optimized by increasing temperature, increasing flow rates, and decreasing membrane thickness. We performed a simulation of NaOH solvent loading vs. time, and found that the solvent reaches a final capacity of around 0.39 mol/L after 16-20 hours. This long loading time indicates that a batch process will likely be needed to ensure a long solvent residence time. Our techno-economic assessment showed that a system based on our design would be too expensive under normal seawater conditions due to low CO_2 fluxes, which lead to prohibitively high membrane costs. However, our TEA results show that this technology could be cost-competitive with DAC if local pH could be lowered below about 6 on the seawater side.

As future work, membrane surface treatments using carbonic anhydrase or other amine groups should be applied to the seawater-side of the membrane to locally lower pH levels and raise CO_2 flux. Future research should also go into coupling our technology with desalination membranes to reduce capital and operating costs by taking advantage of existing infrastructure. This could either be done directly (e.g. a hybrid membrane that simultaneously removes CO_2 and water from seawater) or indirectly (e.g. placing a DOC membrane downstream of a desalination membrane). This kind of coupling would reduce DOC operating costs and provide a platform for rapid scale-up of DOC technology. Further modeling work is also needed to predict CO_2 fluxes at higher NaOH concentrations and with other solvents with faster kinetics. Additionally, more complex 2D-axisymmetric and 3D models should be developed to investigate and optimize mass transport in a direct ocean capture HFMC bundle. Other membrane configurations should also be investigated, such as encapsulated solvents, that could lead to higher surface areas and reduced mass transfer resistance. Overall, direct ocean capture (DOC) using HFMCs is a nascent concept that requires further investigation and optimization. This paper demonstrates that CO_2 separation from seawater using a HFMC is possible, and identifies design improvements and future research directions to make HFMC direct ocean capture economically viable.

3.8 Acknowledgements

The authors gratefully acknowledge financial support from the University of Pittsburgh's, Swanson School of Engineering from the Mechanical Engineering and Materials Science Department. In addition, we would like to thank Will Penman from Composition Coaching for his assistance with revising this manuscript, and we would like to thank graphical artist Rick Henkel for his assistance with creating the graphical abstract for this paper.

4.0 "Modeling Gas Separation in Flat Sheet Membranes: Impact of Flow Channel Size Variation"

Flat sheet membranes offer many advantages over other membrane configurations, (e.g. ease of maintenance and low-pressure drops) that make them a strong candidate for post-combustion carbon capture. A performance model for a stacked flat sheet membrane module is reported in this work. The model is based on the reported specifications for the Gen 2 Polaris™module developed by Membrane Technology & Research (MTR) and predicts performance based on the solution of the governing momentum and mass balance equations. The model accounts for variability in flow channel heights within the module that can arise during module manufacturing. The model is first verified against similar membrane models. Simulations are then performed over a wide range of conditions to demonstrate how much performance declines as channel height variability increases. As per the performance metrics, the dimensionless feed flow rate processed per unit membrane area (f-curve) shows the greatest decline. The changes in performance are comparable to those that occur with hollow fiber membrane modules that possess similar fiber size variations. Together, the results of this study indicate that flow channel height variation in flat sheet membrane modules can hurt CO_2 separation performance, but the impact is minor except at low CO_2 retentate compositions with large channel height variation (e.g. a 10% decline in stage cut performance for a mixture with 94% CO_2 in the permeate stream and 30% channel height variation). However, high variation has a significant impact on overall membrane area with a 30% increase at 30% variation.

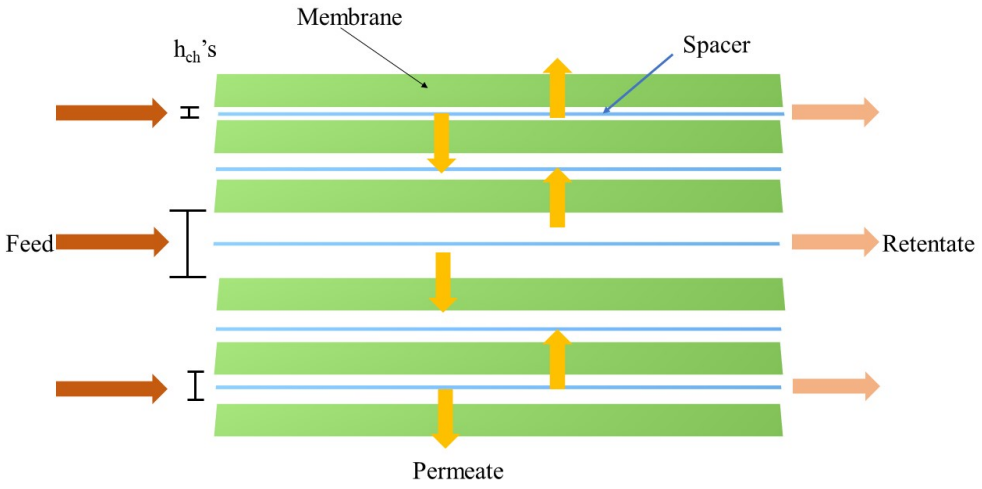

Figure 28: Graphical abstract representing the channel height variation between the membrane sheets in a flat sheet membrane in cross-flow.

4.1 Introduction

Membranes act as a permeate barrier to separate gas components based on molecular diffusivity and solubility. Membranes have been successfully developed for carbon capture processes where CO_2 is separated and stored from flue gas streams to mitigate global warming caused by greenhouse gases. The most common membrane configurations for CO_2 separation are: hollow fiber [193], spiral wound [22], and flat sheet [21] membranes (as shown in Figure 29). Flat sheet membranes (Figure 29a) consist of many flat membrane sheets stacked on top of each other; hollow fiber membranes (Figure 29b) consist of thousands of hollow fibers packed into a bundle; and spiral-wound membranes (Figure 29c) are essentially flat sheet membranes rolled into a collection tube. For the purposes of this work, spiral wound membranes will be considered a different membrane configuration.

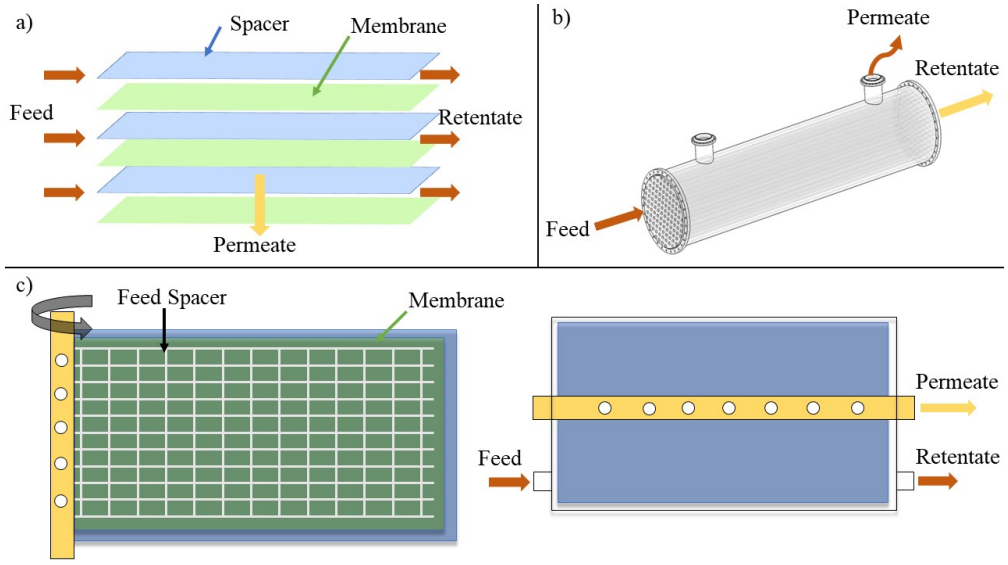

Figure 29: Graphic illustrations of three membrane configurations: a) flat sheet membrane in cross flow, b) hollow fiber membrane in co-current flow, c) spiral wound membrane before and after spinning.

Hollow fiber membranes (HFMs) are the most studied configuration for gas separation purposes, where modeling efforts date back to 1950 [234]. This is because they have a high surface area per unit volume, i.e. high packing density, to promote gas transfer [230]. With increasing demands to mitigate global warming, many membrane modeling studies have focused their efforts on carbon capture using HFMs [185, 53, 135, 202, 10], studying non-ideal conditions such mass transfer resistance [188], non-binary CO_2 separation [41, 143], and non-ideal flow distributions [225, 14].

While HFMs have been developed for CO_2 separation purposes, they have some downsides, such as fiber plugging and high pressure drops [191]. In contrast, flat sheet membranes, also known as plate-and-frame membranes, offer advantages that combat these obstacles, such as lower pressure drops and improved mass transfer due to the feed spacer [21, 239, 83, 121]. Additionally, flat sheet membranes are simple to manufacture and easy to clean [30]. Most studies for flat sheet membranes focus on experimentation or membrane materials for carbon capture. Experiments have observed the effect that fine particles in a gas mixture have on CO_2 separation using flat sheet membranes [232], as well as testing membrane material performance for carbon capture, including surface modification and mixed matrix membranes [179, 78, 99, 210, 62, 139, 31].

Due to the advantages of flat sheet membranes, different applications, such as vapor permeation [155] and desalination [96, 214], have developed models to predict their performance. However, few flat sheet modeling efforts have been documented for carbon capture applications. Bougie et al. developed a model to study flat sheet membrane contactors (i.e.,

a liquid and a gas flows through the membrane) for CO_2 removal from gas mixtures using amines [39]. Rasouli et al. also studied a flat sheet membrane contactor using immobilized carbonic anhydrase for CO_2 capture via experimental and computational efforts [196, 195]. A 2D model was developed to investigate mass transfer within flat sheet membrane contactors for CO_2 separation [161]. Membrane separation processes can be advantageous relative to such absorption processes in that the membrane process is continuous, not cyclic, and membranes do not require solvent regeneration.

Current literature on flat sheet membrane modeling without solvents for carbon capture is limited. A 1D flat sheet model for CO_2 separation was developed by Brinkmann et al., who implemented countercurrent flow to maximize the partial pressure driving force for gas separation [40]. Moreover, this literature has not considered the impact of non-ideal conditions such as manufacturing defects. Incorporating manufacturing defects into computational models is an important next step to predict performance under realistic conditions.

Spiral wound membranes (Figure 29c) have a few studies investigating manufacturing non-idealities, such as spacer channel configuration. The spacer configuration has been compared and optimized for specific conditions [146, 5]. Hollow fiber membrane modeling studies have also shown that membranes can be highly sensitive to variations in the manufacturing process, such as variation in the fiber properties [151], fiber inner diameter [75], and fiber wall thickness [54]. These manufacturing variations can all lead to a dramatic reduction in separation performance. For example, a 10% variation in fiber inner diameter decreases the retentate recovery and product flow rate by 35% and 50%, respectively [151]. This directly affects the membrane area and work required to reach the desired capture rate of 99%. This large decrease in performance for HFMs motivates the need to study how geometric variations effect flat sheet membrane performance. Although there are no publications to our knowledge that model manufacturing variability in carbon capture flat sheet membranes, the literature has emphasized that dispersing sheets uniformly improves CO_2 separation performance in flat sheet modules [242]. This claim further supports the need to investigate non-uniform conditions in flat sheet membranes for carbon capture.

A flat sheet membrane module model is presented here for gas separation that characterizes performance over a range of anticipated operating conditions and analyzes the effects of flow channel height variation. Specifically, a 1D model was developed here to mimic Membrane Technology & Research (MTR)'s Gen 2 Polaris™membrane design that has recently undergone pilot testing at Technology Centre Mongstad. First, we present the methodology used for incorporating channel height variation in the governing momentum and mass balances to predict CO_2 separation performance. Next, the model is validated with ideal (uniform) conditions and the effect of non-uniform channel heights evaluated. Finally, the results are compared against a non-uniform hollow fiber membrane model to test which module type yields better performance.

4.2 Model Description

4.2.1 1D Flat Sheet Model Overview

Our 1D flat sheet model is based on fundamental mass balance equations. Flow channel heights vary within the flat sheet bundle, as shown in Figure 30.

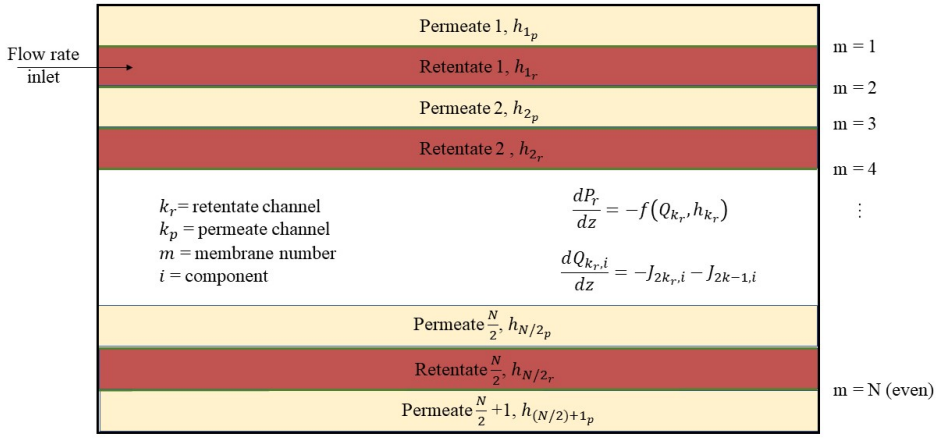

Figure 30: Graphic representation of the 1D model of a flat sheet bundle with varying channel heights. The graphic illustrates the relationships between each channel and the mass balance equations. The channel heights, h (m), are defined based on the type of channel (permeate, p, or retentate, r), channel number, k, and membrane number, m, which varies from 1 to N. The component number is defined as i,. The pressure, P (Pa), is defined as a function of the flow rate, Q (mol s^{-1}), and channel height for the retentate (r) channels. The permeate (p) channel flow rate deviations are considered negligible because this is for a cross-flow configuration. The permeate channel flow rate is described in Equation 4.6.

Figure 30 is used to identify the permeate and retentate channels that contact a membrane m. Gas permeation rate across the membrane are given by:

$$Evenk : J_{m,i} = q_{m,i}a(x_{(m/2),i}P_{r_k,m/2} - y_{(m/2)+1,i}P_{p_k,(m/2)+1}) \tag{4.1}$$

$$Oddk : J_{m,i} = q_{m,i}a(x_{(m+1)/2,i}P_{r_k,(m+1)/2} - y_{(m+1)/2,i}P_{p_k,(m+1)/2}) \tag{4.2}$$

where the membrane flux, J (mol $m^{-2}s{-}1$), is calculated as the product of gas permeance, membrane area, and gas partial pressure difference for a given component (i). In Equations

4.1 and 4.2, q (mol m^{-2} s^{-1} Pa^{-1}) is the membrane permeance (assumed constant for each membrane sheet), a (m^2) membrane area, x retentate (high pressure) mole fraction, y permeate (low pressure) mole fraction, m membrane number, and P retentate and permeate pressures (Pa). Note that the retentate and permeate channel numbers for the channels that contact membrane m are indicated in Equations 4.1 and 4.2 by the subscripts on x, y, and P. Additionally, $J_{m,i}$ is set to 0 for m=0 and m=N+1 in the first and last permeate channel mass balances, respectively.

The following assumptions were made to obtain mass balance equations for the flat sheet membrane module:

1. Retentate and permeate flow channels use similar spacer materials.
2. Membrane properties (i.e., gas permeance, solubility, diffusivity) are uniform along the length of the membrane.
3. System properties (i.e., viscosity, density) are considered constant.
4. Mass transfer resistance in the gas phase is negligible.
5. Axial diffusion in the direction of gas flow is negligible.
6. Membrane geometry does not undergo deformation due to pressure effects.
7. Membrane module operates under steady-state and isothermal conditions.

The flow channel heights were calculated assuming a Gaussian distribution of heights with a mean value (μ) of 250 μm and a range of standard deviations (σ): 0% (no variation), 10% (low variation), 20% (medium variation), and 30% (high variation). Standard deviations are reported as a percentage of the mean, e.g., 10% variation corresponds to a standard deviation of 25 μm. Simulations were performed for a 100 membrane stack corresponding to the number of membranes in MTR's module, with channel heights for the feed and permeate channels selected randomly from the Gaussian distribution [104, 103]. Since the membrane area was set as a constant value, the permeate channels were thus also randomized in reference to the channel height of the surrounding retentate channels. The Gaussian distribution generated a uniform set of random numbers between 0 and 1 and solved for the value of height for which the cumulative distribution function was equal to the random value. This was repeated for 50 different samples of the Gaussian distributions, and the channel heights were averaged to obtain a final set for module performance for each standard deviation considered. Sample flow channel height distributions are illustrated in Figure 31.

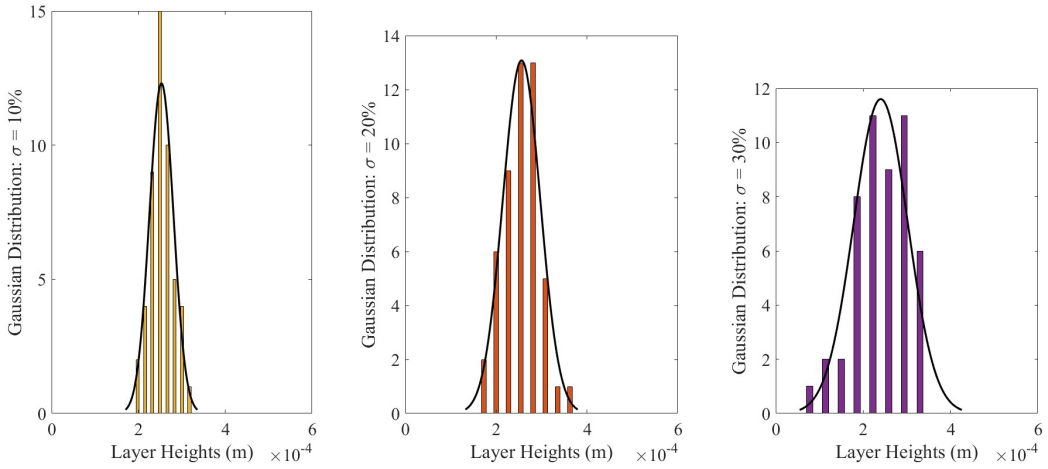

Figure 31: Distributions of 100 channel heights for standard deviations of 10% (left), 20% (middle) and 30% (right). Here, each distribution is compared to its theoretical Gaussian distribution (black curve), showing good agreement with expected values.

4.2.2 Theoretical Implementation & Numerical Methodology

For each standard deviation percentage, the calculated channel heights were used as inputs to the model to calculate the inlet cross-sectional area for the inlet feed flow rate. The modeling methodology, shown in Figure 32, is discussed in incremental order; however, the code itself is nested into three main loops: red loop (re-initialize), blue loop (integration along length), and purple loop (calculate permeate until convergence).

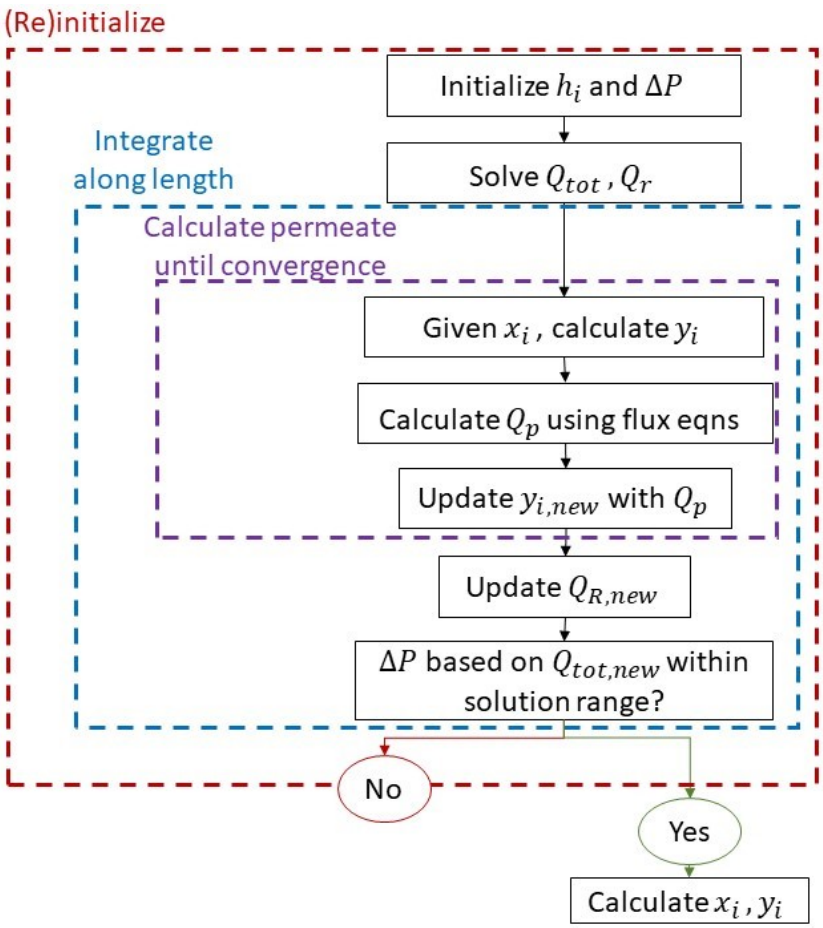

Figure 32: Flow-sheet representing the flat sheet membrane code methodology, which consists of three nested loops: 1) the red, outermost loop is where simulation parameters are (re)initialized; 2) the blue, middle loop integrates the flux equations and mass balances along the length of the membrane; and 3) the purple, innermost loop applies the fundamental equations on a per-channel basis.

4.2.2.1 (Re)initialize calculations until solution is reached (outermost red loop in Figure 32)

The pressure drop (ΔP) across each flow channel is assumed to be constant and must be specified prior to solving the mass balances. The flat sheet membrane module simulated mimics MTR's Gen 2 Polaris™membrane, which has 100 membrane sheets. A pressure drop ranging from 15,000 Pa to 40,000 Pa was chosen to achieve a CO_2 retentate composition of 2% to 18%. For a given pressure drop, the flow rate per channel is determined iteratively to obtain the specified value.

First, the initialized pressure drop is used to calculate the initial guess for the feed flow rate (Q_{tot}). This is a necessary step to be able to apply the value to the fundamental equations (Equations 4.4 - 4.12). The pressure drop and volumetric flow rate relationship used is shown in Equation 4.3 [97]:

$$\frac{\Delta P}{L} = \frac{12\mu}{h_{ch}^3 W \rho} Q_{tot_{k_r}} \tag{4.3}$$

where W (m) is the width of the membrane, L (m) is the length of the membrane, ρ ($mole \cdot m^{-3}$) is the density of the stream mixture, μ ($Pa \cdot s$) is the viscosity of the stream mixture, $h_c h$ (m) is the channel height, and k_r is the channel number. Applying this relationship, the friction factor is calculated as $\lambda = (12\mu L)/(h_{ch}^3 W \rho)$, i.e., $\Delta P = \lambda(Q_{tot_{k_r}})$.

Then, the feed flow rate is used to calculate the inlet component flows, $Q_{k_r,i}$ ($mol \cdot s^{-1}$), based on the known feed composition, φ_i, as shown in Equation 4.4.

$$Q_{k_r,i} = z_i Q_{tot_{k_r}} \tag{4.4}$$

The initial estimates of flow rates for each retentate channel are passed onto the next loop that integrates along the length of the membrane to solve the fundamental equations along the length of the module.

4.2.2.2 Integration along the length of the membrane (blue, middle loop in Figure 32)

Although we are considering non-uniform channel heights, the rest of the model is ideal (see assumptions listed above). Therefore, established mass balance equations are used to solve for the change in gas concentration along the length of the membrane. This approach has been used in previous work and proven to provide accurate results for an ideal membrane model [185]. The length of the membrane is divided into a series of n stages, as shown in Figure 33.

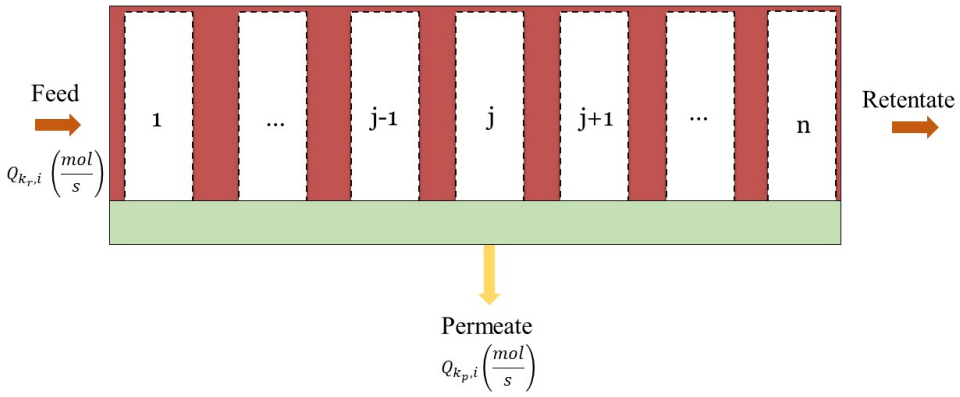

Figure 33: A single retentate channel in the membrane module (red), with the membrane below (green). The gas feed enters at the left-hand-side of the graphic, and the retentate gas exits at the right. The membrane model is discretized into n nodes along the length of the retentate channel, where j represents the current node. $Q_{k_r,i}$ are the retentate flowrates on a per channel, k_r, basis for i gas components, and $Q_{k_p,i}$ are the permeate flow rates.

For the cases considered in this work, 100 stages were deemed appropriate after a grid independence study was performed to demonstrate the results change by less than 0.2% upon increasing the stage number from 100 to 150. Computational times were less than one minute for each case. All the module performance variables, such as the retentate and permeate channel flow rates, take each stage number j into consideration.

4.2.2.3 Solve momentum and mass balances for each stage (purple, innermost loop in Figure 32).

After initializing the feed rate, momentum and mass balances are solved for each stage. The calculation of the permeate composition in each permeate channel requires an iterative procedure due to the contribution of two feed/retentate channels to each permeate channel (except for the first and last permeate channel) and the implicit nature of the mass balances for cross-flow. An example is illustrated in Figure 34.

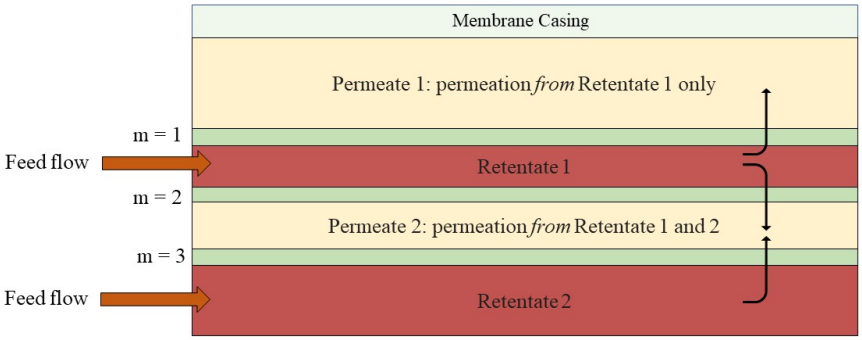

Figure 34: The feed will enter in through the retentate channels bordered by membrane sheets. The gas feed permeates through the membrane into the permeate channels.

For the initial stage ($j = 1$), the initial guess for the permeate composition is calculated based on the feed composition as shown in

$$y_{k_p,i} = \varphi_i \tag{4.5}$$

Using the initial guesses for permeate mole fractions, cross-flow component permeate flow rates are calculated as the sum of the component permeate flows from the two neighboring retentate channels:

$$Q_{k_p,i} = q_{i,u}(P_{H,u}x_{i,u} - P_{L,k_p}y_{k_p,i}) + q_{i,l}(P_{H,l}x_{i,u} - P_{L,k_p}y_{k_p,i}) \tag{4.6}$$

where $Q_{k_p,i}$ $(mol \cdot s^{-1})$ is the permeate flow rate on a per-channel (k_p) and component (i) basis, q_i is the fixed permeance per component, P_H and P_L are the high and low pressures of the system in Pascals (also called the "feed" and "permeate" pressures, respectively), u and l indicate the upper and lower membranes for permeate channel k_p, respectively,and $y_{k_p,i}$ and x_i are the permeate and retentate mole fractions, respectively.

Improved estimates for $y_{k_p,i}$ are obtained through a direct substitution method using Equation 4.7 to obtain each subsequent estimate:

$$y_{k_p,i} = \frac{Q_{k_p,i}}{Q_{tot_{k_p}}} \tag{4.7}$$

where the total permeate flow rate $(Q_{tot_{k_p}})$ is the sum of the component flow rates over all of the components.

For permeate channels adjacent to the external case, permeation occurs from only one retentate channel. This is shown in Equation 4.8 for the first permeate channel, $k_p = 1$. For the last permeate channel, $k_p = N/2 + 1$, permeation only occurs from the last retentate channel (Equation 4.9):

$$y_{1,i} = \frac{q_{i,1}(P_{H,1}x_{i,1})}{Q_{tot_1}} \tag{4.8}$$

$$y_{(N/2)+1,i} = \frac{q_{i,N/2}(P_{H,N/2}x_{i,N/2} - P_{L,(N/2)+1}y_{i,(N/2)+1})}{Q_{tot_{(N/2)+1}}} \tag{4.9}$$

Equations 4.6 – 4.9 are repeated until the permeate compositions reach the convergence criteria, defined within an error of 1e-6 and 25 maximum iterations. Once the permeate channel information is calculated per channel, the information is fed back to the middle, blue loop to calculate the retentate channel information on a per-stage basis.

4.2.2.4 Calculate the retentate flowrates test solution range for convergence (returning to middle, blue loop in Figure 32)

After the permeate flow rates and mole fractions are calculated, the retentate flow rates from each stage are recalculated using the information from the permeate channels. Permeation from the feed channel occurs to both an upper (u) and lower (l) permeate channel as given by Equation 4.10:

$$Q_{k_r,i} = Q_{k_r,i} - L_j q_{i,u}(P_H \frac{Q_{k_r,i}}{Q_{tot_{k_r}}} - P_{L,u}y^*_{i,u}) - L_j q_{i,l}(P_H \frac{Q_{k_r,i}}{Q_{tot_{k_r}}} - P_{L,l}y^*_{i,l}) \tag{4.10}$$

In Equation 4.10, $y^*_{i,l}$ and $y^*_{i,u}$ corresponds to the solutions found in Equations 4.8 and 4.9 for the two adjacent permeate channels. The length is taken on a per-stage basis, L_j. With the updated retentate flow rate, the pressure within the retentate channel at that stage is calculated using the friction factor correlation in Equation 4.3:

$$P_{k_r} = P_{k_r} - \lambda Q_{k_r,i} L_j \tag{4.11}$$

These fundamental equations are all integrated on a per-stage basis, updating along the length of the membrane. The final calculation is fed to the original red loop to either complete the simulation or re-initialize the input parameters if the pressure drop conditions are not met (below).

4.2.2.5 Calculate the final solution per assigned pressure drop condition (returning to red, outer loop in Figure 32)

Finally, after completing the blue and purple loops, the red loop is reintroduced, which tests if the calculated pressure drop solution has converged within the desired pressure drop range. Per retentate channel, the pressure drop is calculated in reference to the feed pressure, P_h, and the pressure calculated in Equation 4.11. The pressure drop needs to match the assigned pressure drop within an absolute tolerance of 0.1% of the feed pressure for the solution to be considered converged.

If the pressure drop calculated does meet the desired criteria, the solution has converged, and the code is exited. If the pressure drop is not within the tolerance assigned, the feed flow rate calculated in Equation 4.11 is replaced with a new value that is either increased or decreased by a ratio of the assigned pressure drop and the calculated pressure drop:

$$Q_{r_{k,i}(new)} = Q_{r_{k,i}(old)} \frac{\Delta P_{(assigned)}}{\Delta P_{(calculated)}} \tag{4.12}$$

4.2.3 Key Performance Metrics

In order to assess membrane module performance as a function of channel height variation, we will use the following three standard performance metrics:

1) Stage cut

Stage cut, θ_s is defined as the ratio of permeate flow rate to feed flow rate:

$$\theta_s = \frac{Q_p}{Q_{tot}} \tag{4.13}$$

2) Recovery

Recovery, θ_r, is defined as the ratio of retentate flow rate to feed flow rate:

$$\theta_r = \frac{Q_r}{Q_{tot}} \tag{4.14}$$

Stage cut and recovery both define the purity of a stream. There is a trade-off between stage cut or recovery and the component concentration. The summation of stage cut and recovery should be equal to 1 thus, at high recovery and low stage cut values, there will be low purity and vice-versa.

3) Dimensionless feed flowrate (F-curve)

The dimensionless feed flowrate, θ_f, is defined below:

$$\theta_f = \frac{Q_{tot}}{q_{CO_2} a P_H} \tag{4.15}$$

where q_{CO_2} (GPU) is the CO_2 membrane permeance, a (m^2) is the membrane area, P_H (Pa) is the feed pressure of the system, and Q_tot ($mol \cdot s^{-1}$) is the total feed flow rate. The

dimensionless feed flow rate plotted against the retentate compositions is called the "f-curve." The f-curve is representative of capital costs of the system because it defines the required membrane area to reach the desired CO_2 composition in the retentate stream. For gas separation, typically the feed flow rate, feed pressure and membrane permeance are known parameters. Therefore, the area of the membrane will be the design variable that will change to reach certain purities.

4.3 Model Results

4.3.1 Validation Results

To the best of our knowledge, our group is the first to incorporate flow channel height variation into a flat sheet membrane model. Also, the most reputable carbon capture modeling results out there are for hollow fiber membranes rather than for flat sheet membranes. Thus, to validate our model, we recreated a published hollow fiber membrane model by C. Y. Pan [185] that considers ideal conditions. Then, this model was updated to incorporate flat sheet membrane geometry conditions while still matching their overall membrane area requirements from Pan. Note, this model does not include the channel relationships presented in the previous methodology section but still considers the same governmental momentum and mass balance equations. This comparison is suitable for validation purposes because for a gas-gas membrane system, the membrane configuration does not affect the overall performance at ideal conditions if the membrane properties and operating conditions remain the same. The results of the two ideal models are shown in Figure 35, and are in excellent agreement.

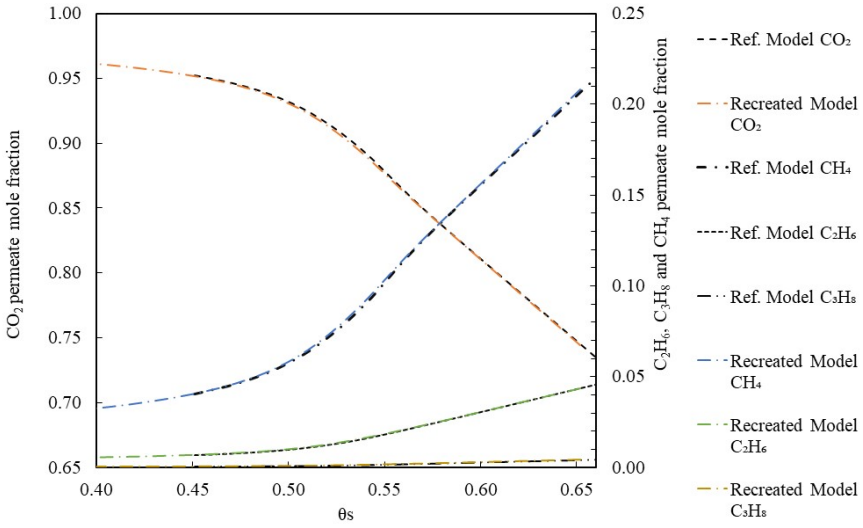

Figure 35: An ideal membrane model that was recreated to verify that the flat sheet membrane configuration will perform identical to hollow fiber membranes when considering the exact conditions [185].

The model presented here was then compared against the verified, recreated flat sheet membrane model at uniform conditions (i.e., 0% standard deviation) using the same conditions from Pan's paper. These results indicate that our model is trustworthy when no channel variation is present, and future plots in this paper (Figures 37-39) verify that our model also matches hollow fiber membrane model predictions when channel height variation is present. The validation results are shown in Figure 36.

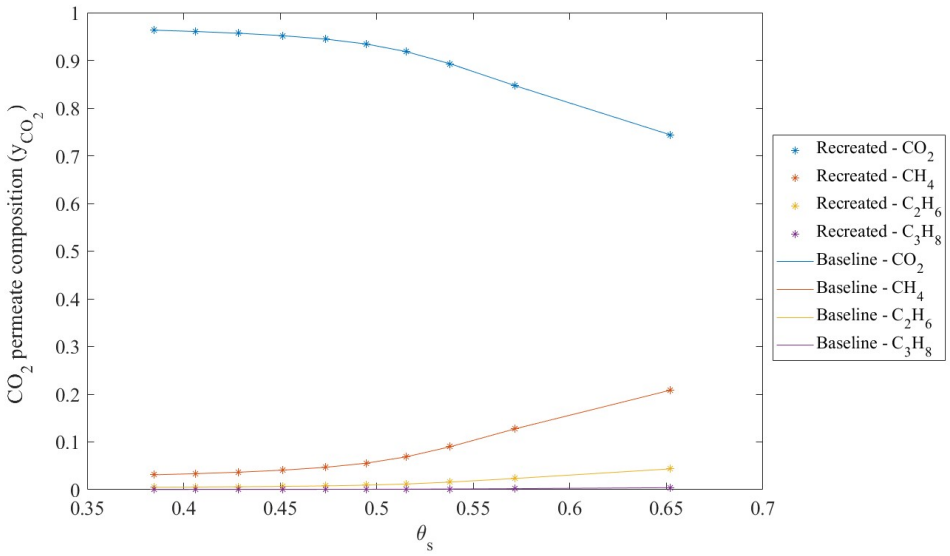

Figure 36: The uniform channel height (0% standard deviation) model vs. the replicated ideal flat sheet model that was validated against a hollow fiber membrane model by C.Y. Pan [185].

4.3.2 Impact of Channel Height Variation on Module Performance

The purpose of this section is to investigate the impact of channel height variation on various module performance metrics to quantify how much manufacturing variability could hurt performance. The flat sheet membrane properties and simulation parameters considered for this study are listed in Table 13. Many of these properties come from MTR's Gen 2 Polaris™flat sheet membrane module [103], which is a state-of-the-art carbon capture membrane design that has already undergone pilot testing. Therefore, the results of this study can inform carbon capture membrane companies of how much manufacturing variability could affect their module performance. For simplification purposes, a binary gas mixture of CO_2/N_2 is chosen.

Membrane parameters	**Variables**	**Values**
Total surface area (m^2)	a	100
Channel height (μm)	h_{ch}	250
Permeances (GPU)	q_i	$q_{N_2} = 0.4$, $q_{CO_2} = 20$
Width (m)	W	1
Length (m)	L	1
Number of membranes	m	100
Membrane thickness μm	t	200
Simulation parameters	**Variables**	**Ranges**
Gas composition	x_{N_2}, x_{CO}	$x_{N_2} = 0.80$, $x_{CO} = 0.20$
Feed pressure (Pa)	P_h	405,300
Permeate pressure (Pa)	P_l	40,530
Temperature (K)	T	298.15
Pressure drop (Pa)	ΔP	1500 – 40,000
Standard deviation (%)	σ	0, 10, 20, 30
Stages along the length of the membrane	N	100

Table 13: Membrane properties and simulation parameters used for the cross-flow flat sheet membrane model. Membrane geometric parameters simulate MTR's Gen 2 flat sheet membrane module [103, 104, 164].

The results presented here were generated by varying the pressure drop across the module to generate curves that ranged from approximately 0.02-0.18 in CO_2 mole fraction in the retentate outlet. The solution for each prescribed pressure drop is represented by an asterisk in the plots. Each figure includes four curves to represent a range of standard deviations in channel height variation: 0%, 10%, 20% and 30%.

4.3.2.1 Impact of Channel Height Variation on Channel Flow Rates

The most obvious model output that should be affected by channel height variation is retentate channel flow rate, since flow rate varies with height cubed (h_{ch}^3), as shown in Equation 4.3. We would expect, therefore, that increasing the variation in channel heights would significantly increase the spread in channel flow rates. In order to investigate the impact of channel height variation on retentate channel flow rate variation, we plotted the standard deviation in channel flow rate as a function of the standard deviation in channel heights in Figure 37. As anticipated, channel height variation had a strong impact on retentate channel flow-rate variation. A 30% standard deviation in channel height resulted in a standard deviation greater than 80% in retentate channel inlet flow rates. These results confirm that channel flow rates vary significantly with variation in channel heights.

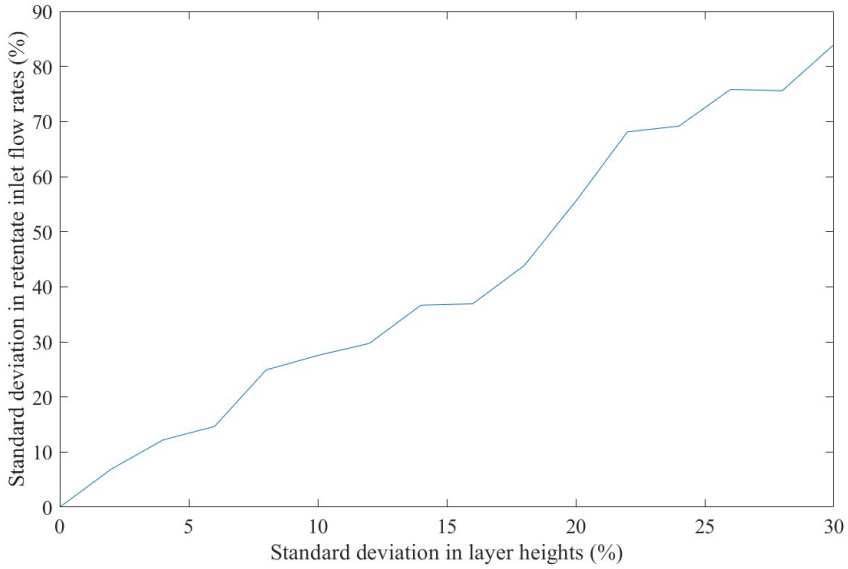

Figure 37: Standard deviation in retentate channel flow rates as a function of standard deviation in channel heights. Channel flow rate variation is a strong function of channel height variation.

4.3.2.2 Impact of Channel Height Variation on Stage Cut

Stage cut, defined in Equation 4.13, is shown in Figure 38 as a function of CO_2 mole fraction in the retentate outlet for the four channel height distributions (0%, 10%, 20%, 30%). For the stage cut design parameter, the lower the stage cut value, the better the performance because that results in lower membrane power requirements. Stage cut is defined as the ratio of the permeate flow rate and the total feel flowrate, or the fraction of the feed gas that permeates the membrane. Therefore, at smaller stage cuts, less gas is lost due to permeation, and energy losses due to gas depressurization are reduced. Typically, lower stage cut values are associated with increasing flow rates (i.e., with increasing pressure drop initializations, as shown in Figure 38).

The results in Figure 38 indicate a slight decrease in performance with increasing distribution of channel heights. For example, at a CO_2 retentate composition of 0.06 (6% not captured), stage cut for the high variation setting increases by approximately 10% relative to the baseline results. This can be explained by the fact that gas flow rates are higher in the larger channels, which leads to a higher flow rate to membrane area ratio and less CO_2 removal. Therefore, more gas must be permeated to reduce the combined retentate composition to the same level relative to the uniform flow channel case.

At larger retentate compositions, the distribution of channel heights does not have as

much of an effect. However, the lower range of CO_2 retentate compositions is of greater interest in an industrial setting since the goal of a carbon capture membrane is to remove as much CO_2 from the feed as possible. Therefore, the key takeaway from these results is that manufacturing variability in channel heights can result in up to a 10% increase in stage cut (based on the results around a CO_2 mole fraction of 0.06).

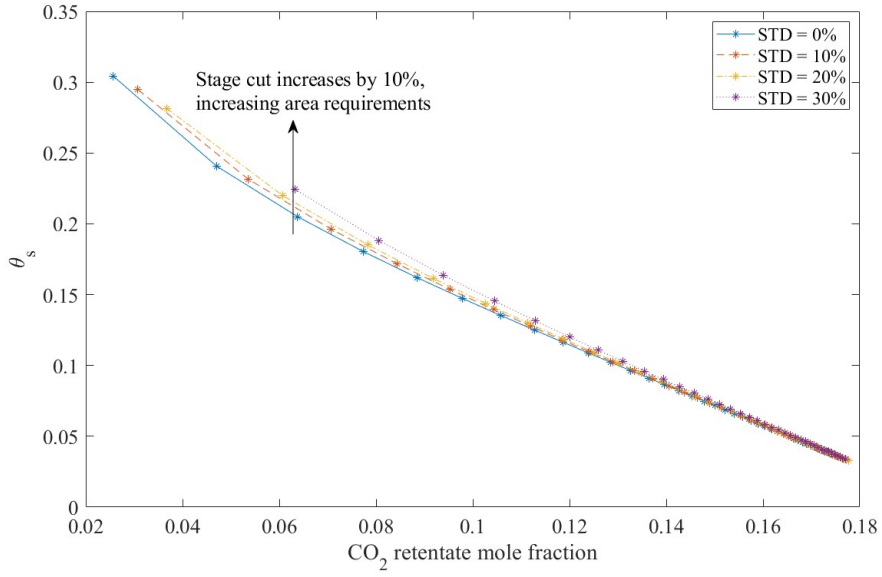

Figure 38: The stage cut, θ_s, defined in Equation 4.13, is plotted against the assigned CO_2 retentate composition for four variations in channel heights: 0%, 10%, 20%, and 30%. At favorable (lower) CO_2 retentate compositions, the stage cut increases with respect to the standard deviation in channel height for a given CO_2 retentate composition. This indicates that stage cut performance declines with increasing spread in channel heights and will require a larger membrane area to achieve the same CO_2 retentate composition.

4.3.2.3 Impact of Channel Height Variation on Recovery

The total recovery, as defined in Equation 4.14, is plotted as a function of CO_2 retentate composition for the four channel height variations in Figure 39. Better performance is associated with higher recovery for a given retentate composition. The recovery curve is expected to increase with increasing pressure drop conditions regardless of the channel height distribution constraints. The results in Figure 39 indicate that variation in channel heights has a slight impact on the recovery curve, particularly at lower CO_2 retentate compositions, which are the most important range to consider on this plot. At a low retentate composition of 0.06, recovery decreases by approximately 2% between the 0% and 30% channel height variation results.

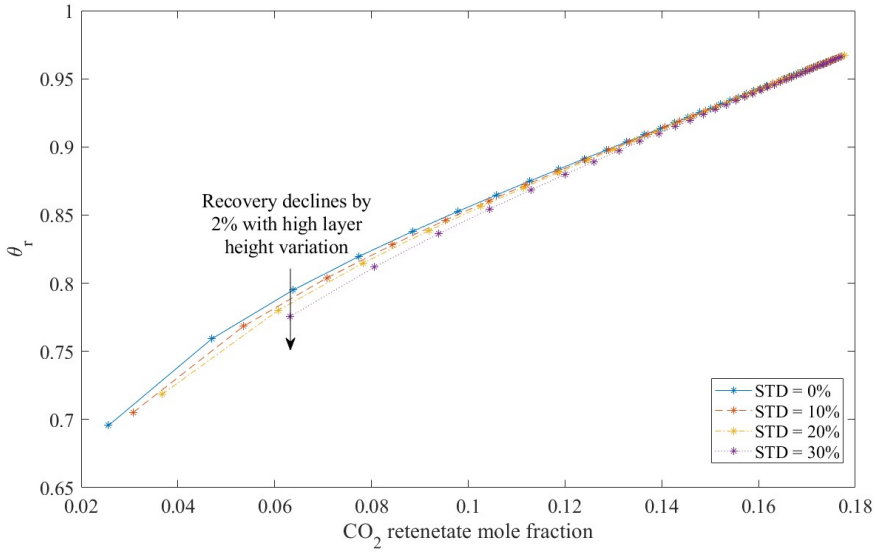

Figure 39: Recovery, θ_r, is plotted against the CO_2 retentate composition for four standard deviations in channel heights: 0%, 10%, 20% and 30%. Recovery decreases with increasing channel height variation at low CO_2 retentate compositions.

4.3.2.4 Impact of Channel Height Variation on F-curve

Finally, the dimensionless feed flow rate, defined in Equation 4.15, represents the capital costs of the system as a dimensionless ratio between the feed flow rate and the membrane area. Figure 40 plots the f-curve, which shows the dimensionless feed flow rate calculated over a range of pressure drops against the associated CO_2 retentate composition. This design parameter is especially sensitive to the channel heights because it is highly dependent on the total feed flow rate (Q_{tot}) calculated as the final solution. Therefore, the f-curve trend differs from the stage cut and recovery variables, where variation is shown regardless of low or high CO_2 retentate compositions.

The f-curve performance decreases given a specific retentate composition with increasing channel height variation. At low CO_2 retentate mole fractions, a larger area is required for the same flow rate at a given product purity. For example, at a CO_2 composition of 0.06, the high variation (standard distribution of 30%) produces a smaller value for the f-curve in comparison to the baseline case (0%, i.e., uniform). When comparing these two dimensionless feed flow rate values, there is a decrease of ∼30%, which corresponds to an increase of 30% in needed membrane area. Using these f-curve values, the area needed to reach such purities can be calculated using Equation 4.15, where the feed flow rate, feed pressure and membrane permeances remain constant. Thus, larger f-curve values are desired since the membrane

area is inversely proportional to the dimensionless feed flow rate, as shown in Equation 4.15. Using this design parameter, one can clearly see the increase in area due to a decrease in the dimensionless feed flow rate needed to achieve the same purity condition at higher channel height variations.

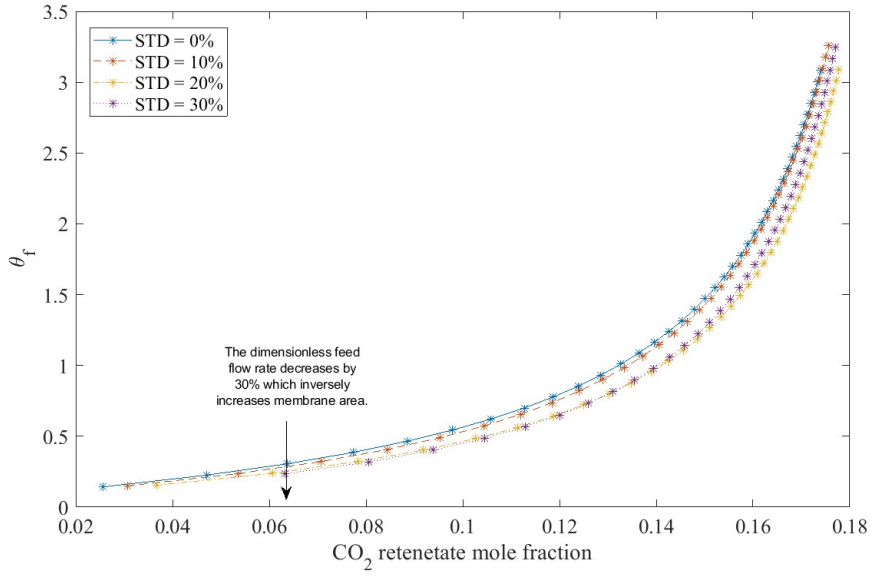

Figure 40: The dimensionless feed flow rate, θ_f, plotted against the CO_2 retentate composition for four standard deviations in channel heights: 0%, 10%, 20% and 30%. The dimensionless feed flow rate values drop as channel height variation increases over the whole f-curves.

The results presented in this section have validated the methodology used and illustrated that a variation in the channel heights for a flat sheet membrane does affect the overall performance in terms of stage cut, recovery, and f-curve. For the example where 94% CO_2 removal from the feed gas (0.06 CO_2 retentate mole fraction) was considered, stage cut decreased by 10%, recovery decreased by 2%, and the dimensionless feed flow rate decreases by approximately 30% at high channel height variation.

The effects of channel height variation are more pronounced at smaller CO_2 retentate compositions, which is the desired purity for most industrial systems. These slight deviations in performance could increase capital or operating costs by a reasonable amount (depending on the system size and the CO_2 capture rate desired), and should be factored into any techno-economic assessments of flat sheet membrane systems. However, in a broader perspective, channel height variation in a single module (not in a system level) has surprisingly little impact on the stage cut and recovery design parameters, even for the medium (20% variation) and high (30% variation) defect settings. However, this was not the case for the dimensionless feed flow rate, where the membrane area increases substantially (by 30%) when channel

height variation is high. This result indicates that membrane size and capital costs are a strong function of manufacturing variability in channel heights.

4.3.3 Flat Sheet vs. Hollow Fiber Membrane Module Performance

The goal of this section is to compare our flat sheet model to a hollow fiber model in order to determine which design is impacted more by geometric variation. For all of the results in this section, we will compare our flat sheet model to a previously published hollow fiber membrane (HFM) model that incorporates an inner fiber diameter variation [39]. The hollow fiber membrane model has a variable inner fiber diameter, whereas and the flat sheet membrane has a variable channel height (both with mean values of 250 μm). For this study, two gas separation cases are considered: 1) CO_2/N_2 (carbon capture), and 2) O_2/N_2 (air separation). For the first case (CO_2/N_2), we put the flat sheet membrane properties and operating conditions (shown in Table 13) into the HFM model for comparison. For the second case (O_2/N_2), the flat sheet membrane model parameters were modified to match the conditions from the published HFM paper for air separation, which are listed again here in Table 14 [39]. The results for these two case studies are presented and discussed below.

4.3.3.1 Case 1: CO_2/N_2 Separation

Figures 41-43 compare the effect of non-uniform channel height on CO_2/N_2 separation performance for hollow fiber membranes (HFMs) vs. flat sheet membranes. As shown in Figure 41, the stage cut curves are almost identical for the HFM and flat sheet designs for a given standard deviation in flow channel dimension. This is also the case for the recovery curves (Figure 42) and the f-curves (Figure 43). Together these results indicate that channel size variation has the same impact on membrane performance regardless of design (hollow fiber vs. flat sheet). As was seen in Figure 40, the f-curve decreased by over 30% for a flat sheet membrane with 30% channel height variation. This is not the case for hollow fiber membranes when comparing no variation to 30% variation in the inner fiber diameter. As shown in Figure 43, there is only a 6.6% decrease in the f-curve at 0.19 CO_2 retentate composition. In all three figures, performance only drops slightly as channel variation increases (e.g. $< 10\%$ decrease in performance when channel height variation goes from 0% to 30% at $x_{CO_2} = 0.06$). These results indicate that manufacturing variability in channel heights will only result in minimal carbon capture performance drops for both HFM and flat sheet membranes.

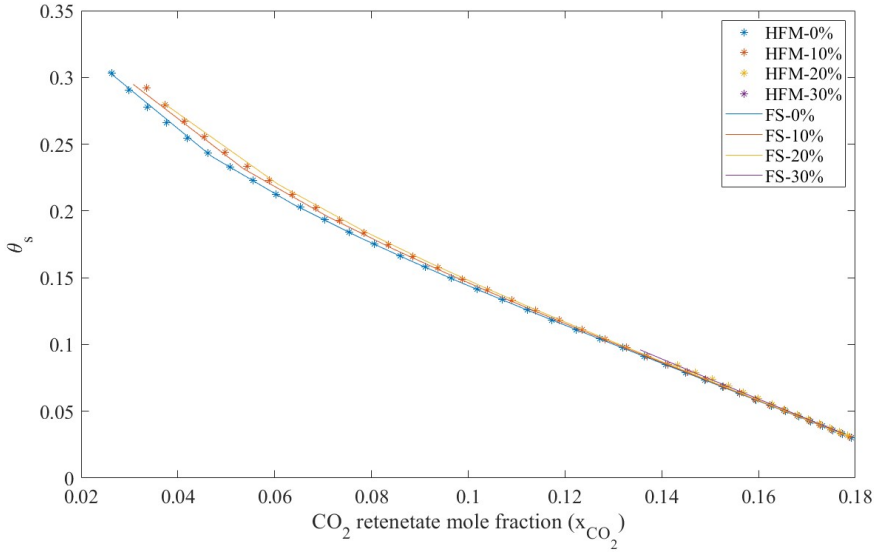

Figure 41: Stage cut as a function of CO_2retentate composition (x_{CO_2}) for CO_2/N_2 separation for both hollow fiber membranes (*) and flat sheet membranes (–). Four standard deviations in channel height are shown: 0%, 10%, 20% and 30%.

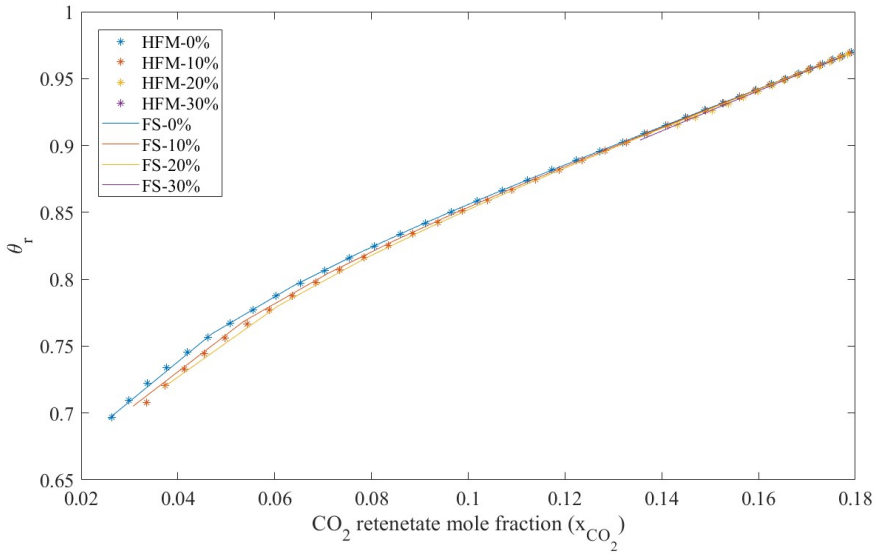

Figure 42: Recovery as a function of CO_2retentate composition (x_{CO_2}) for CO_2/N_2 separation for both hollow fiber membranes (*) and flat sheet membranes (–). Four standard deviations in channel height are shown: 0%, 10%, 20% and 30%.

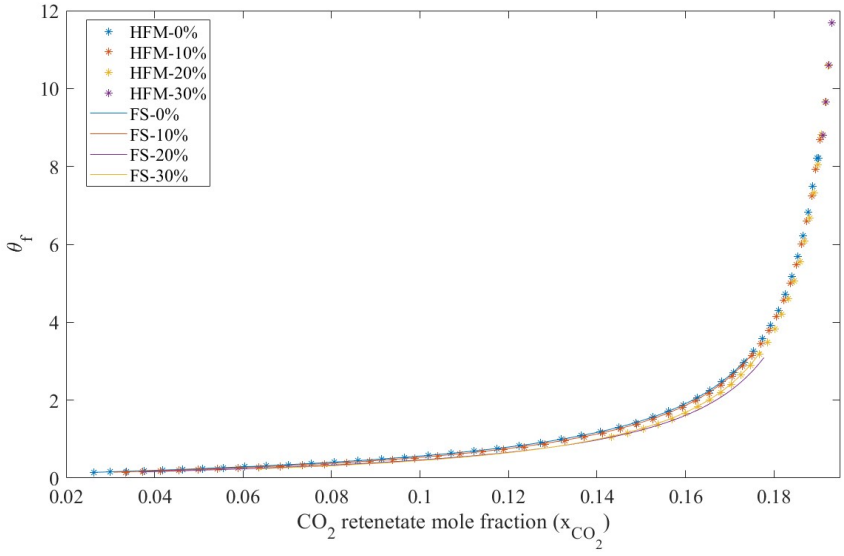

Figure 43: The dimensionless feed flow rateas a function of CO_2retentate composition (x_{CO_2}) for CO_2/N_2 separation for both hollow fiber membranes (*) and flat sheet membranes (–). Four standard deviations in channel height are shown: 0%, 10%, 20% and 30%.

4.3.3.2 Case 2: O_2/N_2 Separation

For the second case study, the flat sheet membrane model parameters were modified to those previously published in a hollow fiber membrane modeling paper that performed a similar investigation on the impact of fiber diameter variation [151]. These new parameters are shown in Table 14. To obtain O_2 retentate compositions of 0.02-0.18, the pressure drop was varied from 900 – 3,900 Pa. The standard deviation percentages that were used for this case were 0% (baseline), 5% (low), and 15% (medium) to match the variation from the published work.

Membrane parameters	**Variables**	**Values**
Total surface area (m^2)	A	94.24
Channel height (μm)	h_{ch}	250
Permeances (GPU)	q_i	$q_{N_2} = 1$, $q_{O_2} = 10$
Width (m)	W	0.9424
Length (m)	L	1
Number of membranes	m	100
Membrane thickness μm	t	200
Simulation parameters	**Variables**	**Ranges**
Gas composition	x_{N_2}, x_{CO}	$x_{N_2} = 0.79$, $x_O = 0.21$
Feed pressure (Pa)	P_h	1,034,000
Permeate pressure (Pa)	P_l	103,400
Temperature (K)	T	298.15
Pressure drop (Pa)	ΔP	900 – 39,000
Standard deviation (%)	σ	0, 5, 15
Stages along the length of the membrane	N	100

Table 14: The flat sheet membrane model parameters used to simulate O_2/N_2 separation and compare against a previously published hollow fiber membrane modeling study [151].

Figures 44-46 compare the effect of non-uniform geometric conditions on O_2/N_2 separation performance for HFMs vs. flat sheet membranes. The results in these three figures indicate that HFM and flat sheet membranes have nearly identical performance for a given standard variation in either inner fiber diameter or channel height. In all three figures, performance decrease is negligibly small as channel height variation increases. These results indicate that manufacturing variability in channel heights will only result in minimal oxygen separation performance drops for both HFM and flat sheet membranes. This is partly due to the fact that channel height variations are capped at 15% in these figures (vs. 30% in Figures 41-43). Overall, the results of this case study indicate that manufacturing variability won't cause performance problems for HFMs or flat sheet membranes used for air separation.

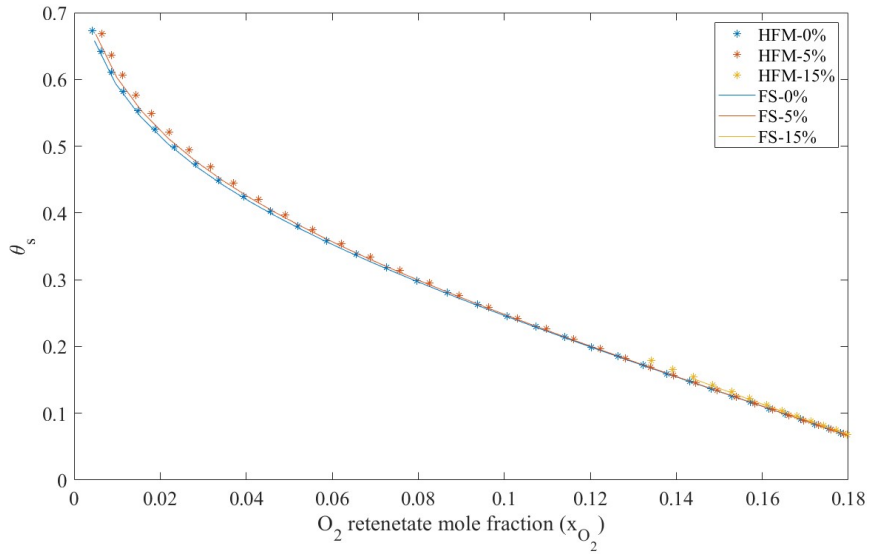

Figure 44: Stage cut as a function of O_2retentate composition (x_{O_2}) for O_2/N_2 separation for both hollow fiber membranes (*) and flat sheet membranes (–). Four standard deviations in channel height are shown: 0%, 5%, 15%.

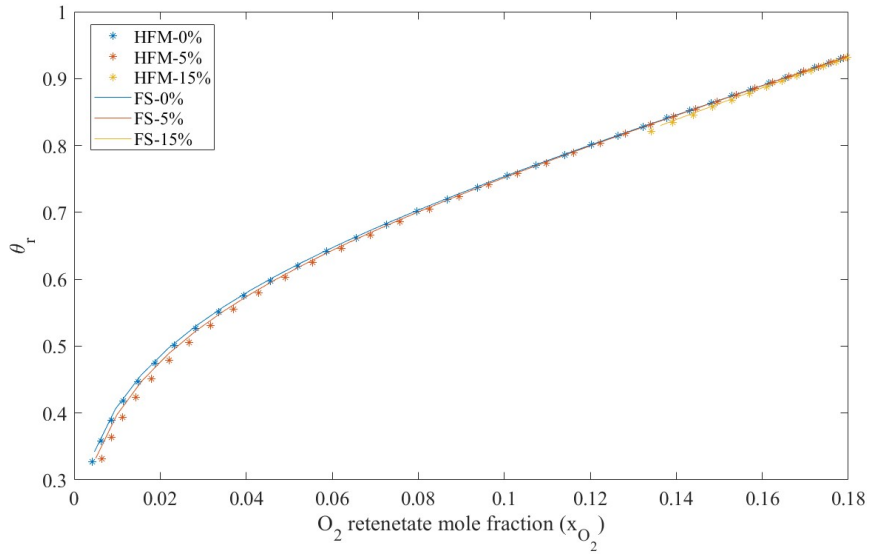

Figure 45: Recovery as a function of O_2retentate composition (x_{O_2}) for O_2/N_2 separation for both hollow fiber membranes (*) and flat sheet membranes (–). Four standard deviations in channel height are shown: 0%, 5%, 15%.

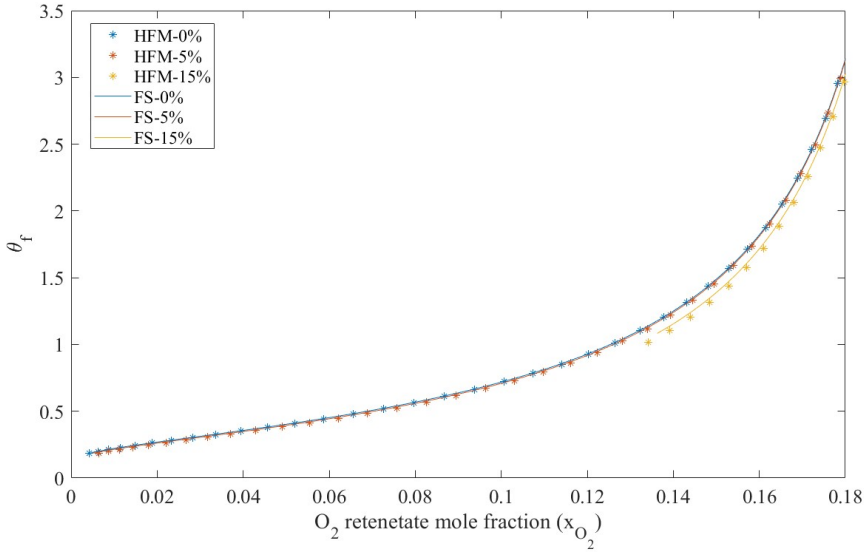

Figure 46: The dimensionless feed flow rate as a function of O_2retentate composition (x_{O_2}) for O_2/N_2 separation for both hollow fiber membranes (*) and flat sheet membranes (–). Four standard deviations in channel height are shown: 0%, 5%, 15%.

4.4 Conclusions

A 1D, non-uniform flat sheet membrane model was developed to investigate the impact of channel height variation on gas separation performance (stage cut, recovery, and dimensionless feed flow rate). Gaussian distributions of heights with standard deviations of 0-30% were fed into the model to generate and compare performance curves. Results indicate that there is a slight decrease in CO_2/N_2 separation performance when aiming for small CO_2 retentate compositions with increasing channel height variability. This is especially prevalent in the dimensionless feed flow rate parameter, where there was a 30% increase in membrane area to achieve 94% CO_2 separation when considering a 30% channel height variation. Companies should therefore tighten their manufacturing process to limit any deviation in channel heights to improve overall CO_2 separation performance.

Additionally, the flat sheet membrane model was compared against a hollow fiber membrane model that also incorporates non-uniform fiber diameters. This comparison was done to compare how the two membrane designs are impacted by size variation. The results indicate that flat sheet membranes and hollow fiber membranes perform almost identically for both CO_2/N_2 and O_2/N_2 separation over a range of geometric standard deviations. Both

designs perform well for both separation applications, even at high channel variations. These results indicate that manufacturing variability in channel height shouldn't cause much of a performance hit for either membrane design with the exception of dimensionless feed flow rate at 30% channel height variation for CO_2/N_2.

In the future, more studies should focus on flat sheet membranes for gas separation and investigate the impact of other non-ideal conditions. Future studies can investigate flow distribution within membrane modules that do not assume uniform channel heights. Additionally, increasing dimensionality of the model (e.g. 2D axisymmetric, 3D) could predict more detailed performance. To expand on this work, a techno-economic analysis could be performed using the CO_2 recovery rates to study how the non-uniform channel height distribution affects capital and operating costs at a systems level.

5.0 Conclusions

With increased efforts to further carbon capture technology and minimize the rise of the global temperature, this thesis has demonstrated the use of membranes for gas separations as a promising approach to rectify the current climate crisis. A literature review of current state-of-the-art membrane modeling techniques was organized to help future post-combustion carbon capture research progress more efficiently. The review paved the way for the projects presented here as it helped determine which modeling techniques were optimal for direct ocean carbon capture. Experimental and computational work determined that direct ocean carbon capture is feasible using a hollow fiber membrane contactor. Since this field is relatively new, the membrane material and seawater composition will need to improve to increase the CO_2 flux, i.e., the driving force, to make hollow fiber membrane contactors competitive against other ocean carbon capture initiatives. Additionally, flat sheet membranes for flue gas compositions were also investigated to determine the effects of non-uniform geometric conditions, such as channel height variation within each membrane sheet. This study concluded that larger variations in the channel heights lead to a decrease in overall performance between 2 - 30%, and that flat sheet and hollow fiber membranes perform identically when the same variations are imposed. The work presented in this thesis advances the current state of membrane technology across different carbon capture applications and brings attention to the advantages they pose. The results illustrate the progress and constraints of current membrane modeling techniques, using membrane contactors in a novel approach, and how membrane performance can be optimized if they are geometrically periodic.

Bibliography

[1] 3m liqui-cell 14x40. Accessed: 2022-07-26.

[2] 3m liqui-cell mini-series. Accessed: 2022-07-26.

[3] Pumping water - energy cost calculator.

[4] Hamed Abdolahi-Mansoorkhani and Sadegh Seddighi. Co2 capture by modified hollow fiber membrane contactor: Numerical study on membrane structure and membrane wettability. *Fuel Processing Technology*, 209:106530, 2020.

[5] AL Ahmad and KK Lau. Impact of different spacer filaments geometries on 2d unsteady hydrodynamics and concentration polarization in spiral wound membrane channel. *Journal of Membrane Science*, 286(1-2):77–92, 2006.

[6] Faizan Ahmad, KK Lau, Azmi Muhamma Shariff, and Yin Fong Yeong. Temperature and pressure dependence of membrane permeance and its effect on process economics of hollow fiber gas separation system. *Journal of membrane science*, 430:44–55, 2013.

[7] Faizan Ahmad, Kok Keon Lau, Serene Sow Mu Lock, Sikander Rafiq, Asad Ullah Khan, and Moonyong Lee. Hollow fiber membrane model for gas separation: Process simulation, experimental validation and module characteristics study. *Journal of Industrial and Engineering Chemistry*, 21:1246–1257, 2015.

[8] Mohamed H Al-Marzouqi, Muftah H El-Naas, Sayed AM Marzouk, Mohamed A Al-Zarooni, Nadia Abdullatif, and Rami Faiz. Modeling of co2 absorption in membrane contactors. *Separation and Purification Technology*, 59(3):286–293, 2008.

[9] Rebecca Albright, Lilian Caldeira, Jessica Hosfelt, Lester Kwiatkowski, Jana K Maclaren, Benjamin M Mason, Yana Nebuchina, Aaron Ninokawa, Julia Pongratz, Katharine L Ricke, et al. Reversal of ocean acidification enhances net coral reef calcification. *Nature*, 531(7594):362–365, 2016.

[10] Nawaf Alkhamis, Ali E Anqi, and Alparslan Oztekin. Computational study of gas separation using a hollow fiber membrane. *International Journal of Heat and Mass Transfer*, 89:749–759, 2015.

[11] Abdulqader Alkhouzaam, Majeda Khraisheh, Mert Atilhan, Shaheen A Al-Muhtaseb, Letian Qi, and David Rooney. *Journal of Natural Gas Science and Engineering*, 36:472–485, 2016.

[12] Myles Allen. *Chapter 1 Framing and Context*, 2018.

[13] Myles Allen, OP Dube, W Solecki, F Aragón-Durand, W Cramer, S Humphreys, M Kainuma, J Kala, N Mahowald, Y Mulugetta, et al. Global warming of 1.5° c. an ipcc special report on the impacts of global warming of 1.5° c above pre-industrial levels and related global greenhouse gas emission pathways, in the context of strengthening the global response to the threat of climate change, sustainable development, and efforts to eradicate poverty. *Sustainable Development, and Efforts to Eradicate Poverty*, 2018.

[14] Mohammed Alrehili, Mustafa Usta, Nawaf Alkhamis, Ali E Anqi, and Alparslan Oztekin. Flows past arrays of hollow fiber membranes–gas separation. *International Journal of Heat and Mass Transfer*, 97:400–411, 2016.

[15] Oscar Alvizo, Luan J Nguyen, Christopher K Savile, Jamie A Bresson, Satish L Lakhapatri, Earl OP Solis, Richard J Fox, James M Broering, Michael R Benoit, Sabrina A Zimmerman, et al. Directed evolution of an ultrastable carbonic anhydrase for highly efficient carbon capture from flue gas. *Proceedings of the National Academy of Sciences*, 111(46):16436–16441, 2014.

[16] Supakorn Atchariyawut, Chunsheng Feng, Rong Wang, Ratana Jiraratananon, and DT Liang. Effect of membrane structure on mass-transfer in the membrane gas–liquid contacting process using microporous pvdf hollow fibers. *Journal of Membrane Science*, 285(1-2):272–281, 2006.

[17] Habib Azarabadi and Klaus S Lackner. Postcombustion capture or direct air capture in decarbonizing us natural gas power? *Environmental science & technology*, 54(8):5102–5111, 2020.

[18] Murray R Badger, Kristin Palmqvist, and Jian-Wei Yu. Measurement of co2 and hco3- fluxes in cyanobacteria and microalgae during steady-state photosynthesis. *Physiologia Plantarum*, 90(3):529–536, 1994.

[19] Ahmad Bahlake, Foad Farivar, and Bahram Dabir. New 3-dimensional cfd modeling of co 2 and h 2 s simultaneous stripping from water within pvdf hollow fiber membrane contactor. *Heat and Mass Transfer*, 52(7):1295–1304, 2016.

[20] Richard W Baker. *Membrane technology and applications*. John Wiley & Sons, 2012.

[21] J Balster. Plate and frame membrane module. *Encyclopedia of Membranes*, pages 1–3, 2013.

[22] Joerg Balster. Spiral wound membrane module. *Encyclopedia of Membranes; Drioli, E., Giorno, L., Eds*, pages 1–3, 2015.

[23] L Bao and GG Lipscomb. Mass transfer in axial flows through randomly packed fiber bundles. In *Membrane Science and Technology*, volume 8, pages 5–26. Elsevier, 2003.

[24] Stepan Bazhenov, Alexandr Bildyukevich, and Alexey Volkov. Gas-liquid hollow fiber membrane contactors for different applications. *Fibers*, 6(4):76, 2018.

[25] Bouchra Belaissaoui and Eric Favre. Novel dense skin hollow fiber membrane contactor based process for co2 removal from raw biogas using water as absorbent. *Separation and Purification Technology*, 193:112–126, 2018.

[26] Robert J Beynon and John S Easterby. *Buffer solutions: The basics*. Taylor & Francis, 2004.

[27] R. B. Bird, Warren E. Stewart, and Edwin N. Lightfoot. *Transport phenomena*. J. Wiley, New York, rev. 2nd edition, 2007.

[28] Totok R Biyanto, Andan Tanjung, Dimas B Priantama, Tita Oxa Anggrea, Gabriella P Dienanta, Titania N Bethiana, and Sonny Irawan. In *Selected Topics on Improved Oil Recovery*, pages 45–58. Springer, 2018.

[29] Board, Ocean Studies and National Academies of Sciences, Engineering, and Medicine and others. *Negative emissions technologies and reliable sequestration: A research agenda*. National Academies Press, 2019.

[30] Mokgadi F Bopape, Tim Van Geel, Abhishek Dutta, Bart Van der Bruggen, and Maurice Stephen Onyango. Numerical modelling assisted design of a compact ultrafiltration (uf) flat sheet membrane module. *Membranes*, 11(1):54, 2021.

[31] Rajashree Borgohain and Bishnupada Mandal. High-speed co2 transport channel containing carboxymethyl chitosan/hydrotalcite membrane for co2 separation. *Journal of Applied Polymer Science*, 137(21):48715, 2020.

[32] Somnuk Boributh, Suttichai Assabumrungrat, Navadol Laosiripojana, and Ratana Jiraratananon. Effect of membrane module arrangement of gas–liquid membrane contacting process on co2 absorption performance: A modeling study. *Journal of membrane science*, 372(1-2):75–86, 2011.

[33] Somnuk Boributh, Suttichai Assabumrungrat, Navadol Laosiripojana, and Ratana Jiraratananon. A modeling study on the effects of membrane characteristics and operating parameters on physical absorption of co2 by hollow fiber membrane contactor. *Journal of membrane science*, 380(1-2):21–33, 2011.

[34] Somnuk Boributh, Ratana Jiraratananon, and Kang Li. Analytical solutions for membrane wetting calculations based on log-normal and normal distribution functions

for co2 absorption by a hollow fiber membrane contactor. *Journal of membrane science*, 429:459–472, 2013.

[35] Somnuk Boributh, Wichitpan Rongwong, Suttichai Assabumrungrat, Navadol Laosiripojana, and Ratana Jiraratananon. Mathematical modeling and cascade design of hollow fiber membrane contactor for co2 absorption by monoethanolamine. *Journal of membrane science*, 401:175–189, 2012.

[36] Aldo Bottino, Gustavo Capannelli, Antonio Comite, Renzo Di Felice, and Raffaella Firpo. Co2 removal from a gas stream by membrane contactor. *Separation and Purification Technology*, 59(1):85–90, 2008.

[37] Noureddine Boucif, Jean Pierre Corriou, Denis Roizard, and Eric Favre. Carbon dioxide absorption by monoethanolamine in hollow fiber membrane contactors: A parametric investigation. *AIChE Journal*, 58(9):2843–2855, 2012.

[38] Noureddine Boucif, Denis Roizard, Jean-Pierre Corriou, and Eric Favre. To what extent does temperature affect absorption in gas-liquid hollow fiber membrane contactors? *Separation Science and Technology*, 50(9):1331–1343, 2015.

[39] Francis Bougie, Ion Iliuta, and Maria C Iliuta. Flat sheet membrane contactor (fsmc) for co2 separation using aqueous amine solutions. *Chemical Engineering Science*, 123:255–264, 2015.

[40] Torsten Brinkmann, Heiko Notzke, Thorsten Wolff, Li Zhao, Sebastian Luhr, and Detlef Stolten. Characterization of a new flat sheet membrane module type for gas permeation. *Chemie Ingenieur Technik*, 91(1-2):30–37, 2019.

[41] David William Brubaker and Karl Kammermeyer. Separation of gases by plastic membranes-permeation rates and extent of separation. *Industrial & Engineering Chemistry*, 46(4):733–739, 1954.

[42] Adele Brunetti, Francesco Scura, Giuseppe Barbieri, and Enrico Drioli. Membrane technologies for co2 separation. *Journal of Membrane Science*, 359(1-2):115–125, 2010.

[43] Henrik Bruus. *Theoretical Microfluidics*. Oxford University Press Inc., New York, rev. 2nd edition, 2009.

[44] Jing Jing Cai, Kelly Hawboldt, and Majid Abedinzadegan Abdi. Analysis of the effect of module design on gas absorption in cross flow hollow membrane contactors via computational fluid dynamics (cfd) analysis. *Journal of Membrane Science*, 520:415–424, 2016.

[45] Fan Cao, Hongxia Gao, Hao Ling, Yangqiang Huang, and Zhiwu Liang. Theoretical modeling of the mass transfer performance of co2 absorption into deab solution in hollow fiber membrane contactor. *Journal of Membrane Science*, 593:117439, 2020.

[46] Nathalie Casas, Johanna Schell, Ronny Pini, and Marco Mazzotti. Fixed bed adsorption of CO_2/ H_2 mixtures on activated carbon: experiments and modeling. *Adsorption*, 18(2):143–161, 2012.

[47] A.H.G. Cents, D.W.F. Brilman, and G.F. Versteeg. Co2 absorption in carbonate/bicarbonate solutions: The danckwerts-criterion revisited.

[48] E Chabanon, E Kimball, E Favre, O Lorain, E Goetheer, D Ferre, A Gomez, and P Broutin. Hollow fiber membrane contactors for post-combustion CO_2. 2013.

[49] E Chabanon, E Kimball, E Favre, O Lorain, E Goetheer, D Ferre, A Gomez, and P Broutin. Hollow fiber membrane contactors for post-combustion co2 capture: A scale-up study from laboratory to pilot plant. *Oil & Gas Science and Technology–Revue d'IFP Energies nouvelles*, 69(6):1035–1045, 2014.

[50] Elodie Chabanon, Denis Roizard, and Eric Favre. Modeling strategies of membrane contactors for post-combustion carbon capture: a critical comparative study. *Chemical engineering science*, 87:393–407, 2013.

[51] Yunhan Chu, Arne Lindbråthen, Linfeng Lei, Xuezhong He, and Magne Hillestad. Mathematical modeling and process parametric study of co2 removal from natural gas by hollow fiber membranes. *Chemical Engineering Research and Design*, 148:45–55, 2019.

[52] DT Coker, T Allen, Benny D Freeman, and GK Fleming. Nonisothermal model for gas separation hollow-fiber membranes. *AIChE journal*, 45(7):1451–1468, 1999.

[53] DT Coker, BD Freeman, and GK Fleming. Modeling multicomponent gas separation using hollow-fiber membrane contactors. *AIChE journal*, 44(6):1289–1302, 1998.

[54] RO Crowder and EL Cussler. Mass transfer in hollow-fiber modules with non-uniform hollow fibers. *Journal of membrane science*, 134(2):235–244, 1997.

[55] Hydroxyl-Terminated Liquid Crystal. Wijmans et al.(1995)"the solution-diffusion model: A review.". *J. Memb. Sci*, 107:1–21, 1995.

[56] Zheng Cui and David deMontigny. Part 7: A review of co2 capture using hollow fiber membrane contactors. *Carbon Management*, 4(1):69–89, 2013.

[57] Edward Lansing Cussler and Edward Lansing Cussler. *Diffusion: mass transfer in fluid systems*. Cambridge university press, 2009.

[58] Radu Custelcean. Direct air capture of co2 using solvents. *Annual Review of Chemical and Biomolecular Engineering*, 13, 2022.

[59] Theodoros Damartzis, Akrivi Asimakopoulou, Dimitrios Koutsonikolas, George Skevis, Chara Georgopoulou, George Dimopoulos, Lampros Nikolopoulos, Konstantinos Bougiouris, Hannes Richter, Udo Lubenau, et al. Solvents for membrane-based post-combustion CO_2 capture for potential application in the marine environment. *Applied Sciences*, 12(12):6100, 2022.

[60] M Rezaei DashtArzhandi, AF Ismail, and T Matsuura. Carbon dioxide stripping through water by porous pvdf/montmorillonite hollow fiber mixed matrix membranes in a membrane contactor. *RSC Advances*, 5(28):21916–21924, 2015.

[61] WJ DeCoursey. Enhancement factors for gas absorption with reversible reaction. *Chemical Engineering Science*, 37(10):1483–1489, 1982.

[62] Liyuan Deng and May-Britt Hagg. Fabrication and evaluation of a blend facilitated transport membrane for co2/ch4 separation. *Industrial & Engineering Chemistry Research*, 54(44):11139–11150, 2015.

[63] Andrew G Dickson and Catherine Goyet. Handbook of methods for the analysis of the various parameters of the carbon dioxide system in sea water. version 2. Technical report, Oak Ridge National Lab., TN (United States), 1994.

[64] VY Dindore, Derk Willem Frederik Brilman, and GF Versteeg. Hollow fiber membrane contactor as a gas–liquid model contactor. *Chemical Engineering Science*, 60(2):467–479, 2005.

[65] VY Dindore, Derk Willem Frederik Brilman, and GF Versteeg. Modelling of cross-flow membrane contactors: mass transfer with chemical reactions. *Journal of membrane science*, 255(1-2):275–289, 2005.

[66] Yong Ding. Perspective on gas separation membrane materials from process economics point of view. *Industrial & Engineering Chemistry Research*, 2019.

[67] Xueliang Dong, Han-Chun Wu, and YS Lin. Co2 permeation through asymmetric thin tubular ceramic-carbonate dual-phase membranes. *Journal of Membrane Science*, 564:73–81, 2018.

[68] Enrico Drioli, Alessandra Criscuoli, and Efrem Curcio. *Membrane contactors: fundamentals, applications and potentialities*. Elsevier, 2011.

[69] Ruth N. Echevarria Huaman. A review on: Co2 capture technology on fossil fuel power plant. *Journal of Fundamentals of Renewable Energy and Applications*, 5(3), 2015.

[70] TJ Edwards, Gerd Maurer, John Newman, and JM Prausnitz. Vapor-liquid equilibria in multicomponent aqueous solutions of volatile weak electrolytes. *AIChE Journal*, 24(6):966–976, 1978.

[71] US EIA. Monthly energy review energy information administration. *Total Energy*, 2020.

[72] Manfred Eigen. Proton transfer, acid-base catalysis, and enzymatic hydrolysis. part i: elementary processes. *Angewandte Chemie International Edition in English*, 3(1):1–19, 1964.

[73] Matthew D Eisaman, Keshav Parajuly, Alexander Tuganov, Craig Eldershaw, Norine Chang, and Karl A Littau. Co 2 extraction from seawater using bipolar membrane electrodialysis. *Energy & Environmental Science*, 5(6):7346–7352, 2012.

[74] P. Eisenberger. System and method for carbon dioxide capture and sequestration. US8500855B2.

[75] Steve Elmore and G Glenn Lipscomb. Analytical approximations of the effect of a fiber size distribution on the performance of hollow fiber membrane separation devices. *Journal of membrane science*, 98(1-2):49–56, 1995.

[76] Sabri Ergun and Ao Ao Orning. Fluid flow through randomly packed columns and fluidized beds. *Industrial & Engineering Chemistry*, 41(6):1179–1184, 1949.

[77] Larry E Erickson and Gary Brase. Paris agreement on climate change. In *Reducing Greenhouse Gas Emissions and Improving Air Quality*, pages 11–22. CRC Press, 2019.

[78] Tobias Esser, Tobias Wolf, Tim Schubert, Jan Benra, Stefan Forero, George Maistros, Stéphan Barbe, George V Theodorakopoulos, Dionysios S Karousos, Andreas A Sapalidis, et al. Co2/ch4 and he/n2 separation properties and water permeability valuation of mixed matrix mwcnts-based cellulose acetate flat sheet membranes: A study of the optimization of the filler material dispersion method. *Nanomaterials*, 11(2):280, 2021.

[79] Rami Faiz and M Al-Marzouqi. Mathematical modeling for the simultaneous absorption of co2 and h2s using mea in hollow fiber membrane contactors. *Journal of Membrane Science*, 342(1-2):269–278, 2009.

[80] Rami Faiz and M Al-Marzouqi. Co2 removal from natural gas at high pressure using membrane contactors: model validation and membrane parametric studies. *Journal of Membrane Science*, 365(1-2):232–241, 2010.

[81] Rami Faiz, Muftah H El-Naas, and M Al-Marzouqi. Significance of gas velocity change during the transport of co2 through hollow fiber membrane contactors. *Chemical engineering journal*, 168(2):593–603, 2011.

[82] Marzie Farjami, Abdolreza Moghadassi, and Vahid Vatanpour. Modeling and simulation of co2 removal in a polyvinylidene fluoride hollow fiber membrane contactor with computational fluid dynamics. *Chemical Engineering and Processing: Process Intensification*, 98:41–51, 2015.

[83] Jana Fárková. The pressure drop in membrane module with spacers. *Journal of membrane science*, 64(1-2):103–111, 1991.

[84] Brian J Fill, Mark J Gartner, Greg Johnson, Jeff Ma, and Marc Horner. Porous media technique for computational modeling of a novel pump-oxygenator. *Asaio Journal*, 52(2):28A, 2006.

[85] Valentin Fougerit, Victor Pozzobon, Dominique Pareau, Marc-André Théoleyre, and Moncef Stambouli. Gas-liquid absorption in industrial cross-flow membrane contactors: Experimental and numerical investigation of the influence of transmembrane pressure on partial wetting. *Chemical Engineering Science*, 170:561–573, 2017.

[86] Valentin Fougerit, Victor Pozzobon, Dominique Pareau, Marc-André Théoleyre, and Moncef Stambouli. Experimental and numerical investigation binary mixture mass transfer in a gas–liquid membrane contactor. *Journal of Membrane Science*, 572:1–11, 2019.

[87] Robert W Fox, Alan T McDonald, and John W Mitchell. *Fox and McDonald's introduction to fluid mechanics*. John Wiley & Sons, 2020.

[88] ACM Franken, JAM Nolten, MHV Mulder, D Bargeman, and CA Smolders. Wetting criteria for the applicability of membrane distillation. *Journal of Membrane Science*, 33(3):315–328, 1987.

[89] Pierre Friedlingstein, Matthew W Jones, Michael O'sullivan, Robbie M Andrew, Judith Hauck, Glen P Peters, Wouter Peters, Julia Pongratz, Stephen Sitch, Corinne Le Quéré, et al. Global carbon budget 2019. *Earth System Science Data*, 11(4):1783–1838, 2019.

[90] Alan Gabelman and Sun-Tak Hwang. Hollow fiber membrane contactors. *Journal of Membrane Science*, 159(1-2):61–106, 1999.

[91] Jozsef Gaspar and Philip Loldrup Fosbøl. Practical enhancement factor model based on gm for multiple parallel reactions: Piperazine (pz) co2 capture. *Chemical Engineering Science*, 158:257–266, 2017.

[92] Nayef Ghasem. Modeling and simulation of the simultaneous absorption/stripping of co2 with potassium glycinate solution in membrane contactor. *Membranes*, 10(4):72, 2020.

[93] Nayef Ghasem, Mohamed Al-Marsouqi, and Nihmiya Abdul Rahim. Simulation of gas/liquid membrane contactor via comsol multiphysics®. 2013.

[94] Arne Gladis, Maria T Gundersen, Philip L Fosbøl, John M Woodley, and Nicolas von Solms. Influence of temperature and solvent concentration on the kinetics of the enzyme carbonic anhydrase in carbon capture technology. *Chemical Engineering Journal*, 309:772–786, 2017.

[95] Nikhil Goyal, Shishir Suman, and SK Gupta. Mathematical modeling of co2 separation from gaseous-mixture using a hollow-fiber membrane module: Physical mechanism and influence of partial-wetting. *Journal of Membrane Science*, 474:64–82, 2015.

[96] B Gu, DY Kim, JH Kim, and Dae Ryook Yang. Mathematical model of flat sheet membrane modules for fo process: Plate-and-frame module and spiral-wound module. *Journal of membrane science*, 379(1-2):403–415, 2011.

[97] L Gurreri, A Tamburini, A Cipollina, G Micale, M Ciofalo, et al. Pressure drop at low reynolds numbers in woven-spacer-filled channels for membrane processes: Cfd prediction and experimental validation. *Desalin. Water Treat*, 61:170–182, 2017.

[98] Bahram Haddadi, Christian Jordan, Martin Miltner, and Michael Harasek. Membrane modeling using cfd: Combined evaluation of mass transfer and geometrical influences in 1d and 3d. *Journal of membrane science*, 563:199–209, 2018.

[99] Mohamad Rezi Abdul Hamid and Hae-Kwon Jeong. Recent advances on mixed-matrix membranes for gas separation: Opportunities and engineering challenges. *Korean Journal of Chemical Engineering*, 35(8):1577–1600, 2018.

[100] Yang Han, Witopo Salim, Kai K Chen, Dongzhu Wu, and WS Winston Ho. Field trial of spiral-wound facilitated transport membrane module for co2 capture from flue gas. *Journal of Membrane Science*, 575:242–251, 2019.

[101] J Hao, PA Rice, and SA Stern. Upgrading low-quality natural gas with h2s-and co2-selective polymer membranes: Part i. process design and economics of membrane stages without recycle streams. *Journal of Membrane Science*, 209(1):177–206, 2002.

[102] J Hao, PA Rice, and SA Stern. Upgrading low-quality natural gas with h2s-and co2-selective polymer membranes: Part ii. process design, economics, and sensitivity study of membrane stages with recycle streams. *Journal of Membrane Science*, 320(1-2):108–122, 2008.

[103] Pingjiao Hao, JG Wijmans, Jay Kniep, and Richard W Baker. Low-pressure membrane contactors for carbon dioxide capture. pages 9–25, 2019.

[104] Pingjiao Hao, JG Wijmans, Jay Kniep, and Richard W Baker. Low-pressure membrane contactors for carbon dioxide capture de-fe0007553, 2019.

[105] John Happel. Viscous flow relative to arrays of cylinders. *AIChE Journal*, 5(2):174–177, 1959.

[106] DL Hartmann, AMG Klein Tank, M Rusticucci, LV Alexander, S Brönnimann, Y Charabi, and FJ Dentener. Ipcc climate change 2013: The physical science basis. 2013.

[107] J Niklas Hausmann, Robert Schlögl, Prashanth W Menezes, and Matthias Driess. Is direct seawater splitting economically meaningful? 2021.

[108] X He. The latest development on membrane materials and processes for post-combustion co2 capture: a review. *SF J Material Chem Eng. 2018; 1 (1)*, 1009, 2018.

[109] Xuezhong He. A review of material development in the field of carbon capture and the application of membrane-based processes in power plants and energy-intensive industries. *Energy, Sustainability and Society*, 8(1):34, 2018.

[110] Xuezhong He and May-Britt Hägg. Hollow fiber carbon membranes: Investigations for co2 capture. *Journal of membrane science*, 378(1-2):1–9, 2011.

[111] Jay MS Henis and Mary K Tripodi. Composite hollow fiber membranes for gas separation: the resistance model approach. *Journal of Membrane Science*, 8(3):233–246, 1981.

[112] H Hikita, S Asai, and T Takatsuka. Absorption of carbon dioxide into aqueous sodium hydroxide and sodium carbonate-bicarbonate solutions. *The Chemical Engineering Journal*, 11(2):131–141, 1976.

[113] Karl Anders Hoff. Modeling and experimental study of carbon dioxide absorption in a membrane contactor. 2003.

[114] Karl Anders Hoff, Olav Juliussen, Olav Falk-Pedersen, and Hallvard F Svendsen. Modeling and experimental study of carbon dioxide absorption in aqueous alkanolamine solutions using a membrane contactor. *Industrial & engineering chemistry research*, 43(16):4908–4921, 2004.

[115] Abolhassan Hosseinzadeh, Mohammadtaghi Hosseinzadeh, Ali Vatani, and Toraj Mohammadi. Mathematical modeling for the simultaneous absorption of co2 and so2 using mea in hollow fiber membrane contactors. *Chemical Engineering and Processing: Process Intensification*, 111:35–45, 2017.

[116] Arshad Hussain and May-Britt Hägg. A feasibility study of co2 capture from flue gas by a facilitated transport membrane. *Journal of Membrane Science*, 359(1-2):140–148, 2010.

[117] Mohamed H Ibrahim, Muftah H El-Naas, Zhien Zhang, and Bart Van der Bruggen. Co2 capture using hollow fiber membranes: A review of membrane wetting. *Energy & Fuels*, 32(2):963–978, 2018.

[118] Ahmad Fauzi Ismail and LIB David. A review on the latest development of carbon membranes for gas separation. *Journal of membrane science*, 193(1):1–18, 2001.

[119] Ahmad Fauzi Ismail, TD Kusworo, A Mustafa, and H Hasbulla. Understanding the solution-diffusion mechanism in gas separation membrane for engineering students. In *Regional Conference on Engineering Education RCEE*, volume 20052005, 2005.

[120] Guozhao Ji and Ming Zhao. Membrane separation technology in carbon capture. *Recent Advances in Carbon Capture and Storage; Yun, Y., Ed*, pages 59–90, 2017.

[121] Matthias Johannink, Kannan Masilamani, Adel Mhamdi, Sabine Roller, and Wolfgang Marquardt. Predictive pressure drop models for membrane channels with non-woven and woven spacers. *Desalination*, 376:41–54, 2015.

[122] Kenneth S Johnson. Carbon dioxide hydration and dehydration kinetics in seawater 1. *Limnology and Oceanography*, 27(5):849–855, 1982.

[123] Sayan Kar, Alain Goeppert, Vicente Galvan, Ryan Chowdhury, Justin Olah, and GK Surya Prakash. A carbon-neutral CO_2 capture, conversion, and utilization cycle with low-temperature regeneration of sodium hydroxide. *Journal of the American Chemical Society*, 140(49):16873–16876, 2018.

[124] CD Keeling, SC Piper, RB Bacatow, M Wahlen, TP Whorf, PM Heimann, and HA Meijer. Atmospheric CO_2 and CO_2 exchange with the terrestrial biosphere and oceans from 1978 to 2000. 2005.

[125] Ralph F Keeling and Charles D Keeling. Atmospheric monthly in situ CO_2 data-mauna loa observatory, hawaii. *Scripps CO_2 program data*, 2017.

[126] David W Keith. Why capture co2 from the atmosphere? *Science*, 325(5948):1654–1655, 2009.

[127] David W Keith, Minh Ha-Duong, and Joshuah K Stolaroff. Climate strategy with co 2 capture from the air. *Climatic Change*, 74(1):17–45, 2006.

[128] David W Keith, Geoffrey Holmes, David St Angelo, and Kenton Heidel. A process for capturing CO_2 from the atmosphere. *Joule*, 2(8):1573–1594, 2018.

[129] David W. Keith, Geoffrey Holmes, David St. Angelo, and Kenton Heidel. A process for capturing co2 from the atmosphere. *Joule*, 2(8):1573–1594, 2018.

[130] Sakarin Khaisri, David deMontigny, Paitoon Tontiwachwuthikul, and Ratana Jiraratananon. A mathematical model for gas absorption membrane contactors that studies the effect of partially wetted membranes. *Journal of Membrane Science*, 347(1-2):228–239, 2010.

[131] Rajab Khalilpour, Ali Abbas, Zhiping Lai, and Ingo Pinnau. Modeling and parametric analysis of hollow fiber membrane system for carbon capture from multicomponent flue gas. *AIChE journal*, 58(5):1550–1561, 2012.

[132] Rajab Khalilpour, Kathryn Mumford, Haibo Zhai, Ali Abbas, Geoff Stevens, and Edward S Rubin. Membrane-based carbon capture from flue gas: a review. *Journal of Cleaner Production*, 103:286–300, 2015.

[133] Erin Kimball, Adam Al-Azki, Adrien Gomez, Earl Goetheer, Nick Booth, Dick Adams, and Daniel Ferre. Hollow fiber membrane contactors for co2 capture: modeling and up-scaling to co2 capture for an 800 mwe coal power station. *Oil & Gas Science and Technology–Revue d'IFP Energies nouvelles*, 69(6):1047–1058, 2014.

[134] Goutham Kotamreddy, Ryan Hughes, Debangsu Bhattacharyya, Joshua Stolaroff, Katherine Hornbostel, Michael Matuszewski, and Benjamin Omell. Process modeling and techno-economic analysis of a co2 capture process using fixed bed reactors with a microencapsulated solvent. *Energy & Fuels*, 33(8):7534–7549, 2019.

[135] A Sarma Kovvali, S Vemury, and Wudneh Admassu. Modeling of multicomponent countercurrent gas permeators. *Industrial & engineering chemistry research*, 33(4):896–903, 1994.

[136] H Kreulen, CA Smolders, GF Versteeg, and Willibrordus Petrus Maria Van Swaaij. Determination of mass transfer rates in wetted and non-wetted microporous membranes. *Chemical engineering science*, 48(11):2093–2102, 1993.

[137] H Kreulen, CA Smolders, GF Versteeg, and Willibrordus Petrus Maria van Swaaij. Microporous hollow fibre membrane modules as gas-liquid contactors part 2. mass transfer with chemical reaction. *Journal of Membrane Science*, 78(3):217–238, 1993.

[138] PS Kumar, JA Hogendoorn, PHM Feron, and GF Versteeg. Approximate solution to predict the enhancement factor for the reactive absorption of a gas in a liquid flowing through a microporous membrane hollow fiber. *Journal of membrane science*, 213(1-2):231–245, 2003.

[139] Shankar Kunalan, Kandasamy Palanivelu, Eledathu Kuriachan Sachin, Daria Aleksandrovna Syrtsova, and Vladimir Vasilievich Teplyakov. Thin-film hydrogel polymer layered polyvinyltrimethylsilane dual-layer flat-bed composite membrane for co2 gas separation. *Journal of Applied Polymer Science*, 139(17):52024, 2022.

[140] Klaus S Lackner and Habib Azarabadi. Buying down the cost of direct air capture. *Industrial & Engineering Chemistry Research*, 60(22):8196–8208, 2021.

[141] Corinne Le Quéré, Robert J Andres, T Boden, Thomas Conway, Richard A Houghton, Joanna I House, Gregg Marland, Glen Philip Peters, Guido Van der Werf, Anders Ahlström, et al. The global carbon budget 1959–2011. *Earth System Science Data Discussions*, 5(2):1107–1157, 2012.

[142] Corinne Le Quéré, Robbie M Andrew, Pierre Friedlingstein, Stephen Sitch, Judith Hauck, Julia Pongratz, Penelope A Pickers, Jan Ivar Korsbakken, Glen P Peters, Josep G Canadell, et al. Global carbon budget 2018. *Earth System Science Data*, 10(4):2141–2194, 2018.

[143] Sunghoon Lee, Michael Binns, Jung Hyun Lee, Jong-Ho Moon, Jeong-gu Yeo, Yeong-Koo Yeo, Young Moo Lee, and Jin-Kuk Kim. Membrane separation process for co2 capture from mixed gases using tr and xtr hollow fiber membranes: process modeling and experiments. *Journal of Membrane Science*, 541:224–234, 2017.

[144] T Leiknes. Theory of transport in membrane. *PhD Thesis-TorOve Leiknes. nd*, pages 1–17.

[145] Bingyun Li, Yuhua Duan, David Luebke, and Bryan Morreale. Advances in co2 capture technology: A patent review. *Applied Energy*, 102:1439–1447, 2013.

[146] F Li, W Meindersma, AB De Haan, and T Reith. Optimization of commercial net spacers in spiral wound membrane modules. *Journal of Membrane Science*, 208(1-2):289–302, 2002.

[147] Jing-Liang Li and Bing-Hung Chen. Review of co2 absorption using chemical solvents in hollow fiber membrane contactors. *Separation and Purification Technology*, 41(2):109–122, 2005.

[148] Wen Li, Sunho Choi, Jeffery H Drese, Marc Hornbostel, Gopala Krishnan, Peter M Eisenberger, and Christopher W Jones. Steam-stripping for regeneration of supported amine-based CO_2 adsorbents. *ChemSusChem*, 3(8):899–903, 2010.

[149] Yifu Li, Pengrui Jin, Xue Song, Xinyuan Zhan, et al. Removal of carbon dioxide from pressurized landfill gas by physical absorbents using a hollow fiber membrane contactor. *Chemical Engineering and Processing: Process Intensification*, 121:149–161, 2017.

[150] SY Lim, YY Liang, GA Fimbres Weihs, DE Wiley, and DF Fletcher. A cfd study on the effect of membrane permeance on permeate flux enhancement generated by unsteady slip velocity. *Journal of membrane science*, 556:138–145, 2018.

[151] B Liu, GG Lipscomb, and J Jensvold. Effect of fiber variation on staged membrane gas separation module performance. *AIChE journal*, 47(10):2206–2219, 2001.

[152] Hongguang Liu, Klaus Lackner, and Xiaomei Fan. Value-added involved in CO_2 emissions embodied in global demand-supply chains. *Journal of Environmental Planning and Management*, 64(1):76–100, 2021.

[153] Serene Sow Mu Lock, Kok Keon Lau, Faizan Ahmad, and AM Shariff. Modeling, simulation and economic analysis of co2 capture from natural gas using cocurrent, countercurrent and radial crossflow hollow fiber membrane. *International Journal of Greenhouse Gas Control*, 36:114–134, 2015.

[154] Jian-Gang Lu, You-Fei Zheng, and Min-Dong Cheng. Wetting mechanism in mass transfer process of hydrophobic membrane gas absorption. *Journal of Membrane Science*, 308(1-2):180–190, 2008.

[155] Shingjiang Jessie Lue, Wen Wei Chen, Su Yu Wu, Li Ding Wang, and Chun Hung Kuo. Vapor permeation modeling of multi-component systems using a poly (dimethylsiloxane) membrane. *Journal of Membrane Science*, 311(1-2):380–389, 2008.

[156] Patricia Luis. *Fundamental Modeling of Membrane Systems: Membrane and Process Performance*. Elsevier, 2018.

[157] Maryam Mahmoudkhani and David W Keith. Low-energy sodium hydroxide recovery for CO_2 capture from atmospheric air—thermodynamic analysis. *International Journal of Greenhouse Gas Control*, 3(4):376–384, 2009.

[158] A Malek, K Li, and WK Teo. Modeling of microporous hollow fiber membrane modules operated under partially wetted conditions. *Industrial & engineering chemistry research*, 36(3):784–793, 1997.

[159] A Mansourizadeh, AF Ismail, and T Matsuura. Effect of operating conditions on the physical and chemical co2 absorption through the pvdf hollow fiber membrane contactor. *Journal of Membrane Science*, 353(1-2):192–200, 2010.

[160] Azam Marjani, Ali Taghvaie Nakhjiri, Arezoo Sodagar Taleghani, and Saeed Shirazian. Mass transfer modeling absorption using nanofluids in porous polymeric membranes. *Journal of Molecular Liquids*, 318:114115, 2020.

[161] AZAM MARJANI[1], SAEED SHIRAZIAN[1], MAHMOUD RANJBAR[1], and Mitra Ahmadi. Mathematical modeling of gas separation in flat-sheet membrane contactors. 2012.

[162] Sayed AM Marzouk, Mohamed H Al-Marzouqi, Muftah H El-Naas, Nadia Abdullatif, and Zahoor M Ismail. Removal of carbon dioxide from pressurized co2–ch4 gas mixture using hollow fiber membrane contactors. *Journal of Membrane Science*, 351(1-2):21–27, 2010.

[163] Mehrdad Massoudi and AK Uguz. Chemically-reacting fluids with variable transport properties. *Applied Mathematics and Computation*, 219(4):1761–1775, 2012.

[164] Norfamila Che Mat and G Glenn Lipscomb. Membrane process optimization for carbon capture. *International Journal of Greenhouse Gas Control*, 62:1–12, 2017.

[165] Norfamilabinti Che Mat, Yuecun Lou, and G Glenn Lipscomb. Hollow fiber membrane modules. *Current Opinion in Chemical Engineering*, 4:18–24, 2014.

[166] Guillain Mauviel, Julien Berthiaud, Cécile Vallieres, Denis Roizard, and Eric Favre. Dense membrane permeation: From the limitations of the permeability concept back to the solution-diffusion model. *Journal of membrane science*, 266(1-2):62–67, 2005.

[167] M Mavroudi, SP Kaldis, and GP Sakellaropoulos. A study of mass transfer resistance in membrane gas–liquid contacting processes. *Journal of Membrane Science*, 272(1-2):103–115, 2006.

[168] S Peters Max, D Timmerhaus Klaus, and E West Ronald. *Plant design and economics for chemical engineers*. McGraw-Hill Companies, 2003.

[169] Ali R Mazaheri and Goodarz Ahmadi. Uniformity of the fluid flow velocities within hollow fiber membranes of blood oxygenation devices. *Artificial organs*, 30(1):10–15, 2006.

[170] Noah McQueen, Katherine Vaz Gomes, Colin McCormick, Katherine Blumanthal, Maxwell Pisciotta, and Jennifer Wilcox. A review of direct air capture (dac): scaling up commercial technologies and innovating for the future. *Progress in Energy*, 3(3):032001, 2021.

[171] Enrique Medina-Martos, José-Luis Gálvez-Martos, Jorge Almarza, Carlos Lirio, Diego Iribarren, Antonio Valente, and Javier Dufour. Environmental and economic performance of carbon capture with sodium hydroxide. *Journal of CO_2 Utilization*, 60:101991, 2022.

[172] Mohsen Mehdipourghazi, Sara Barati, and Farshad Varaminian. Mathematical modeling and simulation of carbon dioxide stripping from water using hollow fiber membrane contactors. *Chemical Engineering and Processing: Process Intensification*, 95:159–164, 2015.

[173] Norman U Meldrum and Francis JW Roughton. Carbonic anhydrase. its preparation and properties. *The Journal of physiology*, 80(2):113, 1933.

[174] Monoj Kumar Mondal, Hemant Kumar Balsora, and Prachi Varshney. Progress and trends in co2 capture/separation technologies: a review. *Energy*, 46(1):431–441, 2012.

[175] Sanaz Mosadegh-Sedghi, Denis Rodrigue, Josée Brisson, and Maria C Iliuta. Wetting phenomenon in membrane contactors–causes and prevention. *Journal of Membrane Science*, 452:332–353, 2014.

[176] AH Ahmadi Motlagh and SH Hashemabadi. 3d cfd simulation and experimental validation of particle-to-fluid heat transfer in a randomly packed bed of cylindrical particles. *International Communications in Heat and Mass Transfer*, 35(9):1183–1189, 2008.

[177] Marcel Mulder. Basic principles of membrane technology. 2012.

[178] Marcel Mulder and J Mulder. *Basic principles of membrane technology*. Springer Science & Business Media, 1996.

[179] Nima Nabian, Ali Asghar Ghoreyshi, Ahmad Rahimpour, and Mohsen Shakeri. Performance evaluation and mass transfer study of co 2 absorption in flat sheet membrane contactor using novel porous polysulfone membrane. *Korean Journal of Chemical Engineering*, 32(11):2204–2211, 2015.

[180] Ali Taghvaie Nakhjiri and Amir Heydarinasab. Cfd analysis of co2 sequestration applying different absorbents inside the microporous pvdf hollow fiber membrane contactor. *Periodica Polytechnica Chemical Engineering*, 64(1):135–145, 2020.

[181] Ali Taghvaie Nakhjiri, Amir Heydarinasab, Omid Bakhtiari, and Toraj Mohammadi. Numerical simulation of co2/h2s simultaneous removal from natural gas using potassium carbonate aqueous solution in hollow fiber membrane contactor. *Journal of Environmental Chemical Engineering*, page 104130, 2020.

[182] None None. The national carbon capture center at the power systems development facility. Technical report, Southern Company Services Incorporated, Wilsonville, AL (United States), 2014.

[183] Anil Kumar Pabby and Ana Maria Sastre. State-of-the-art review on hollow fibre contactor technology and membrane-based extraction processes. *Journal of membrane science*, 430:263–303, 2013.

[184] Hassan Pahlavanzadeh, Mohammad Darabi, Vahid Rajabi Ghaleh, and Omid Bakhtiari. Cfd modeling of co2 absorption in membrane contactors using aqueous solutions of monoethanolamine–ionic liquids. *Industrial & Engineering Chemistry Research*, 59(41):18629–18639, 2020.

[185] CY Pan. Gas separation by high-flux, asymmetric hollow-fiber membrane. *AIChE Journal*, 32(12):2020–2027, 1986.

[186] Subham Paul, Aloke K Ghoshal, and Bishnupada Mandal. Removal of co2 by single and blended aqueous alkanolamine solvents in hollow-fiber membrane contactor: modeling and simulation. *Industrial & engineering chemistry research*, 46(8):2576–2588, 2007.

[187] Ryszard Pohorecki and Wadysaw Moniuk. Kinetics of reaction between carbon dioxide and hydroxyl ions in aqueous electrolyte solutions. *Chemical engineering science*, 43(7):1677–1684, 1988.

[188] Victor Pozzobon and Patrick Perré. Mass transfer in hollow fiber membrane contactor: Computational fluid dynamics determination of the shell side resistance. *Separation and Purification Technology*, 241:116674, 2020.

[189] Sohaib Qazi, Lucía Gómez-Coma, Jonathan Albo, Stéphanie Druon-Bocquet, Angel Irabien, and Jose Sanchez-Marcano. Co2 capture in a hollow fiber membrane contactor coupled with ionic liquid: Influence of membrane wetting and process parameters. *Separation and Purification Technology*, 233:115986, 2020.

[190] Sohaib Qazi, Lucía Gómez-Coma, Jonathan Albo, Stéphanie Druon-Bocquet, Angel Irabien, Mohammad Younas, and José Sanchez-Marcano. Mathematical modeling of co2 absorption with ionic liquids in a membrane contactor, study of absorption kinetics and influence of temperature. *Journal of Chemical Technology & Biotechnology*, 2020.

[191] Zhang Qi and EL Cussler. Microporous hollow fibers for gas absorption: I. mass transfer in the liquid. *Journal of membrane science*, 23(3):321–332, 1985.

[192] R. H. Byrne, F. T. Mackenzie, and A. C. Duxbury. Seawater. *Encycl. Br.*, 2020.

[193] Stephen A Rackley. *Carbon capture and storage*. Butterworth-Heinemann, 2017.

[194] Raghavendra Ragipani, Keerthana Sreenivasan, Robert P Anex, Hang Zhai, and Bu Wang. Direct air capture and sequestration of CO_2 by accelerated indirect aqueous mineral carbonation under ambient conditions. *ACS Sustainable Chemistry & Engineering*, 2022.

[195] Hannaneh Rasouli, Ion Iliuta, Francis Bougie, Alain Garnier, and Maria C Iliuta. Enzyme-immobilized flat-sheet membrane contactor for green carbon capture. *Chemical Engineering Journal*, 421:129587, 2021.

[196] Hannaneh Rasouli, Ion Iliuta, Francis Bougie, Alain Garnier, and Maria C Iliuta. Hybrid enzymatic co2 capture process in intensified flat sheet membrane contactors with immobilized carbonic anhydrase. *Separation and Purification Technology*, 287:120505, 2022.

[197] Greg H Rau, Heather D Willauer, and Zhiyong Jason Ren. The global potential for converting renewable electricity to negative CO_2 emissions hydrogen. *Nature Climate Change*, 8(7):621–625, 2018.

[198] Seyed Mohammad Reza Razavi, Saeed Shirazian, and Mahboobeh Nazemian. Numerical simulation of co2 separation from gas mixtures in membrane modules: Effect of chemical absorbent. *Arabian Journal of Chemistry*, 9(1):62–71, 2016.

[199] Mohammad Rezaei, David M Warsinger, Mikel C Duke, Takeshi Matsuura, Wolfgang M Samhaber, et al. Wetting phenomena in membrane distillation: Mechanisms, reversal, and prevention. *Water research*, 139:329–352, 2018.

[200] Mashallah Rezakazemi, Zahra Niazi, Mojtaba Mirfendereski, Saeed Shirazian, Toraj Mohammadi, and Afshin Pak. Cfd simulation of natural gas sweetening in a gas–liquid hollow-fiber membrane contactor. *Chemical Engineering Journal*, 168(3):1217–1226, 2011.

[201] Joanna R. Rivero, Grigorios Panagakos, Austin Lieber, and Katherine Hornbostel. Hollow fiber membrane contactors for post-combustion carbon capture: A review of modeling approaches. *Membranes*, 10(12):1–35, 2020.

[202] Joanna R Rivero, Grigorios Panagakos, Austin Lieber, and Katherine Hornbostel. Hollow fiber membrane contactors for post-combustion carbon capture: A review of modeling approaches. *Membranes*, 10(12):382, 2020.

[203] Sabine Rode, Phuc Tien Nguyen, Denis Roizard, Roda Bounaceur, Christophe Castel, and Eric Favre. Evaluating the intensification potential of membrane contactors for

gas absorption in a chemical solvent: A generic one-dimensional methodology and its application to co2 absorption in monoethanolamine. *Journal of membrane science*, 389:1–16, 2012.

[204] Wichitpan Rongwong, Ratana Jiraratananon, and Supakorn Atchariyawut. Experimental study on membrane wetting in gas–liquid membrane contacting process for co2 absorption by single and mixed absorbents. *Separation and Purification Technology*, 69(1):118–125, 2009.

[205] Simon Roussanaly, Rahul Anantharaman, Karl Lindqvist, Haibo Zhai, and Edward Rubin. Membrane properties required for post-combustion co2 capture at coal-fired power plants. *Journal of Membrane Science*, 511:250–264, 2016.

[206] Muhammad Saeed and Liyuan Deng. Post-combustion co2 membrane absorption promoted by mimic enzyme. *Journal of Membrane Science*, 499:36–46, 2016.

[207] MS Saidi, MR Hajaligol, A Mhaisekar, and M Subbiah. A 3d modeling of static and forward smoldering combustion in a packed bed of materials. *Applied Mathematical Modelling*, 31(9):1970–1996, 2007.

[208] Rolf Sander. Henry's law constants. *National Institute of Standards and Technology*, 2020.

[209] Eloy S Sanz-Pérez, Christopher R Murdock, Stephanie A Didas, and Christopher W Jones. Direct capture of co2 from ambient air. *Chemical reviews*, 116(19):11840–11876, 2016.

[210] Andreas A Sapalidis, Panagiotis I Karantzis, Achilles Vairis, Stephanos F Nitodas, Stéphan Barbe, and Evangelos P Favvas. A study of the reinforcement effect of mwcnts onto polyimide flat sheet membranes. *Polymers*, 12(6):1381, 2020.

[211] Colin A Scholes, Abdul Qader, Geoff W Stevens, and Sandra E Kentish. Membrane gas-solvent contactor pilot plant trials of co2 absorption from flue gas. *Separation Science and Technology*, 49(16):2449–2458, 2014.

[212] Colin A Scholes, Michael Simioni, Abdul Qader, Geoff W Stevens, and Sandra E Kentish. Membrane gas–solvent contactor trials of co2 absorption from syngas. *Chemical engineering journal*, 195:188–197, 2012.

[213] Kai G Schulz, Ulf Riebesell, Bjoern Rost, Silke Thoms, and RE Zeebe. Determination of the rate constants for the carbon dioxide to bicarbonate inter-conversion in ph-buffered seawater systems. *Marine chemistry*, 100(1-2):53–65, 2006.

[214] Yonghyun Shin, Hyeongrak Cho, Jihyuck Choi, Yong Sun Jang, Yong-Jun Choi, Jinsik Sohn, Sangho Lee, and Juneseock Choi. Application of response surface methodology

(rsm) in the optimization of dewetting conditions for flat sheet membrane distillation (md) membranes. *Desalination and Water Treatment*, 57(22):10020–10030, 2016.

[215] S Shirazian and SN Ashrafizadeh. Mass transfer simulation of carbon dioxide absorption in a hollow-fiber membrane contactor. *Separation Science and Technology*, 45(4):515–524, 2010.

[216] Saeed Shirazian, Abdolreza Moghadassi, and Sadegh Moradi. Numerical simulation of mass transfer in gas–liquid hollow fiber membrane contactors for laminar flow conditions. *Simulation Modelling Practice and Theory*, 17(4):708–718, 2009.

[217] Saeed Shirazian, Mahboobeh Pishnamazi, Mashallah Rezakazemi, Amir Nouri, Mostafa Jafari, Sooran Noroozi, and Azam Marjani. Implementation of the finite element method for simulation of mass transfer in membrane contactors. *Chemical Engineering & Technology*, 35(6):1077–1084, 2012.

[218] Saeed Shirazian, Ali Taghvaie Nakhjiri, Amir Heydarinasab, and Mahdi Ghadiri. Theoretical investigations on the effect of absorbent type on carbon dioxide capture in hollow-fiber membrane contactors. *Plos one*, 15(7):e0236367, 2020.

[219] John C Slattery. *Advanced transport phenomena*. Cambridge University Press, 1999.

[220] Mahmoud Reza Sohrabi, Azam Marjani, Sadegh Moradi, Mehran Davallo, and Saeed Shirazian. Mathematical modeling and numerical simulation of co2 transport through hollow-fiber membranes. *Applied Mathematical Modelling*, 35(1):174–188, 2011.

[221] RG Svitek and WJ Federspiel. A mathematical model to predict co 2 removal in hollow fiber membrane oxygenators. *Annals of biomedical engineering*, 36(6):992–1003, 2008.

[222] Morteza Taherinejad, John Gorman, Ephraim Sparrow, and Shahram Derakhshan. Porous medium model of a hollow-fiber water filtration system. *Journal of membrane science*, 563:210–220, 2018.

[223] Constantine Tsonopoulos, Dale M Coulson, and Lawrence B Inman. Ionization constants of water pollutants. *Journal of chemical and engineering data*, 21(2):190–193, 1976.

[224] A Kerem Uguz and Mehrdad Massoudi. Heat transfer and couette flow of a chemically reacting non-linear fluid. *Mathematical methods in the applied sciences*, 33(11):1331–1341, 2010.

[225] Mustafa Usta, Michael Morabito, Mohammed Alrehili, Alaa Hakim, and Alparslan Oztekin. Steady three-dimensional flows past hollow fiber membrane arrays–cross flow arrangement. *Canadian Journal of Physics*, 96(12):1272–1287, 2018.

[226] Sriram Valluri and SK Kawatra. Reduced reagent regeneration energy for CO_2 capture with bipolar membrane electrodialysis. *Fuel Processing Technology*, 213:106691, 2021.

[227] Kévin Villeneuve, Denis Roizard, Jean-Christophe Remigy, Marcello Iacono, and Sabine Rode. Co2 capture by aqueous ammonia with hollow fiber membrane contactors: Gas phase reactions and performance stability. *Separation and Purification Technology*, 199:189–197, 2018.

[228] Kevin Villeneuve, David Albarracin Zaidiza, Denis Roizard, and Sabine Rode. Modeling and simulation of co2 capture in aqueous ammonia with hollow fiber composite membrane contactors using a selective dense layer. *Chemical Engineering Science*, 190:345–360, 2018.

[229] Monika Vogt, Ralf Goldschmidt, Dieter Bathen, Bernhard Epp, and Hans Fahlenkamp. Comparison of membrane contactor and structured packings for co2 absorption. *Energy Procedia*, 4:1471–1477, 2011.

[230] Chun Feng Wan, Tianshi Yang, G Glenn Lipscomb, Donald J Stookey, and Tai-Shung Chung. Design and fabrication of hollow fiber membrane modules. *Journal of Membrane Science*, 538:96–107, 2017.

[231] R Wang, DF Li, and DT Liang. Modeling of co2 capture by three typical amine solutions in hollow fiber membrane contactors. *Chemical Engineering and Processing: Process Intensification*, 43(7):849–856, 2004.

[232] Xia Wang, Hao Chen, Lin Zhang, Ran Yu, Rumin Qu, and Linjun Yang. Effects of coexistent gaseous components and fine particles in the flue gas on co2 separation by flat-sheet polysulfone membranes. *Journal of membrane science*, 470:237–245, 2014.

[233] Yuan Wang, Li Zhao, Alexander Otto, Martin Robinius, and Detlef Stolten. A review of post-combustion co2 capture technologies from coal-fired power plants. *Energy Procedia*, 114:650–665, 2017.

[234] Sol Weller and Waldo A Steiner. Separation of gases by fractional permeation through membranes. *Journal of Applied Physics*, 21(4):279–283, 1950.

[235] Stephen Whitaker. Forced convection heat transfer correlations for flow in pipes, past flat plates, single cylinders, single spheres, and for flow in packed beds and tube bundles. *AIChE Journal*, 18(2):361–371, 1972.

[236] S.R. Wickramasinghe, M J Semmens, and Edward Cussler. Mass-transfer in various hollow fiber geometries. *Journal of Membrane Science*, 69:235–250, 05 1992.

[237] Heather D Willauer, Felice DiMascio, Dennis R Hardy, and Frederick W Williams. Feasibility of CO_2 extraction from seawater and simultaneous hydrogen gas genera-

tion using a novel and robust electrolytic cation exchange module based on continuous electrodeionization technology. *Industrial & Engineering Chemistry Research*, 53(31):12192–12200, 2014.

[238] Sam Wong, WD Gunter, MJ Mavor, et al. Economics of co2 sequestration in coalbed methane reservoirs. In *SPE/CERI Gas Technology Symposium*. Society of Petroleum Engineers, 2000.

[239] Jiayou Xu, Zhi Wang, Zhihua Qiao, Hongyu Wu, Songlin Dong, Song Zhao, and Jixiao Wang. Post-combustion co2 capture with membrane process: Practical membrane performance and appropriate pressure. *Journal of Membrane Science*, 581:195–213, 2019.

[240] Ming-Chien Yang and EL Cussler. Designing hollow-fiber contactors. *AIChE Journal*, 32(11):1910–1916, 1986.

[241] Wenjing Yang, Yundong Wang, Jianfeng Chen, and Weiyang Fei. Computational fluid dynamic simulation of fluid flow in a rotating packed bed. *Chemical Engineering Journal*, 156(3):582–587, 2010.

[242] Weiliang Yuan, Lingzhi Zhu, Chao Luo, Hongguang Liu, Zan Chen, Yanzhen He, and Enshan Han. Enhanced co2 separation properties by incorporating acid-functionalized graphene oxide into polyimide membrane. *High Performance Polymers*, 33(4):405–416, 2021.

[243] David Albarracin Zaidiza, Bouchra Belaissaoui, Sabine Rode, and Eric Favre. Intensification potential of hollow fiber membrane contactors for co2 chemical absorption and stripping using monoethanolamine solutions. *Separation and Purification Technology*, 188:38–51, 2017.

[244] David Albarracin Zaidiza, Bouchra Belaissaoui, Sabine Rode, Thibaut Neveux, Camel Makhloufi, Christophe Castel, Denis Roizard, and Eric Favre. Adiabatic modelling of co2 capture by amine solvents using membrane contactors. *Journal of Membrane Science*, 493:106–119, 2015.

[245] David Albarracin Zaidiza, Joseph Billaud, Bouchra Belaissaoui, Sabine Rode, Denis Roizard, and Eric Favre. Modeling of co2 post-combustion capture using membrane contactors, comparison between one-and two-dimensional approaches. *Journal of membrane science*, 455:64–74, 2014.

[246] David Albarracin Zaidiza, Seth Gabriel Wilson, Bouchra Belaissaoui, Sabine Rode, Christophe Castel, Denis Roizard, and Eric Favre. Rigorous modelling of adiabatic multicomponent co2 post-combustion capture using hollow fibre membrane contactors. *Chemical Engineering Science*, 145:45–58, 2016.

[247] ZHANG Ze and J Sx. Hollow fiber membrane contactor absorption of co2 from the flue gas: review and perspective. *Glob. Nest J*, 16:355–374, 2014.

[248] Richard Zeebe and Dieter Wolf-Gladrow. Carbon dioxide, dissolved (ocean). In *Encyclopedia of paleoclimatology and ancient environments/ed. by Vivien Gornitz Dordrecht: Springer*, pages 123–127. 2009.

[249] Richard E Zeebe and Dieter Wolf-Gladrow. *CO_2 in seawater: equilibrium, kinetics, isotopes*. Number 65. Gulf Professional Publishing, 2001.

[250] Haibo Zhai and Edward S Rubin. Techno-economic assessment of polymer membrane systems for postcombustion carbon capture at coal-fired power plants. *Environmental science & technology*, 47(6):3006–3014, 2013.

[251] Hong-Yan Zhang, Rong Wang, David Tee Liang, and Joo Hwa Tay. Modeling and experimental study of co2 absorption in a hollow fiber membrane contactor. *Journal of membrane science*, 279(1-2):301–310, 2006.

[252] Hong-Yan Zhang, Rong Wang, David Tee Liang, and Joo Hwa Tay. Theoretical and experimental studies of membrane wetting in the membrane gas–liquid contacting process for co2 absorption. *Journal of Membrane Science*, 308(1-2):162–170, 2008.

[253] Juntao Zhang, Timothy DC Nolan, Tao Zhang, Bartley P Griffith, and Zhongjun J Wu. Characterization of membrane blood oxygenation devices using computational fluid dynamics. *Journal of Membrane Science*, 288(1-2):268–279, 2007.

[254] Yuan Zhang, Jaka Sunarso, Shaomin Liu, and Rong Wang. Current status and development of membranes for co2/ch4 separation: A review. *International Journal of Greenhouse Gas Control*, 12:84–107, 2013.

[255] Shuaifei Zhao, Paul HM Feron, Liyuan Deng, Eric Favre, Elodie Chabanon, Shuiping Yan, Jingwei Hou, Vicki Chen, and Hong Qi. Status and progress of membrane contactors in post-combustion carbon capture: A state-of-the-art review of new developments. *Journal of Membrane Science*, 511:180–206, 2016.